

INAUGURAL-DISSERTATION

zur

Erlangung der Doktorwürde

der

Naturwissenschaftlich-Mathematischen

Gesamtfakultät

der

Ruprecht-Karls-Universität

Heidelberg

vorgelegt von

Shuying WAN, MSc.

aus Sichuan, China

Tag der mündlichen Prüfung: 8. Februar 1999

In-beam γ -spectroscopy
with Relativistic Radioactive Ion Beams

Gutachter: Prof. Dr. Dirk Schwalm
Prof. Dr. Dietrich Pelte

Abstract

In-beam γ -spectroscopy with relativistic radioactive ion beams (RIB) is a rather untouched field which offers new opportunities to study the nuclear structure of exotic nuclei: Coulomb excitation and few nucleon removal reactions provide rich spectroscopic information; thick secondary targets can be used resulting in large yields counteracting low beam intensities. On the other hand, one has to cope with large Doppler effects and huge atomic background.

After the fragmentation reaction of ^{50}Ti on ^9Be at 330 AMeV, more than 30 neutron-rich isotopes from B to Ca were selected simultaneously by the FRagment Separator FRS at GSI, Darmstadt. Peripheral collisions with secondary Pb and C targets were employed to populate excited states. Particle detectors before and behind the target enabled the identification of mass, charge and trajectory of the individual beam species and secondary fragments. De-excitation γ -rays were detected with the Darmstadt-Heidelberg Crystal Ball spectrometer. Discrete γ -transitions could be observed in ~ 30 isotopes, down to beam intensities of only ~ 80 particles per second. Coulomb excitation allowed the determination of $B(E2)$ values of low lying low spin states. From few nucleon removal reactions, in particular using the C target, the γ -decay of higher lying states with medium spin was observed. Thus in this experiment the promising potential of a new method to study the structure of exotic nuclei has been shown.

Kurzfassung

Gamma-Spektroskopie mit relativistischen radioaktiven Strahlen ist ein nahezu unberührtes Gebiet, das neue Möglichkeiten bietet, die Struktur exotischer Kerne zu studieren: Coulomb-anregung und Wenignukleonen-Abstreifreaktionen bieten reichhaltige spektroskopische Informationen; dicke Sekundärtargets können verwendet werden, um die geringen Strahlintensitäten zu kompensieren. Andererseits stellen der starke Dopplereffekt und ein extremer atomarer Untergrund experimentelle Herausforderungen dar.

Nach Fragmentationsreaktionen von ^{50}Ti an ^9Be bei 330 AMeV wurden mehr als 30 n-reiche Isotope von B bis Ca gleichzeitig durch den Fragmentseparator FRS der GSI, Darmstadt, selektiert. Periphere Reaktionen mit sekundären Pb- und C-Targets dienten zur Bevölkung angeregter Zustände. Masse, Ladung und Trajektorie der Kerne wurden mit Teilchendetektoren vor und hinter dem Target bestimmt. Ihr γ -Zerfall wurde mit der Darmstadt-Heidelberg Kristallkugel gemessen.

Diskrete γ -Übergänge konnten in ~ 30 Isotopen bei Strahlintensitäten ab ~ 80 Teilchen pro Sekunde nachgewiesen werden. Coulombanregung erlaubte die Bestimmung von $B(E2)$ -Werten niedrigliegender Niederspinzustände. Der γ -Zerfall höher angeregter Zustände mittleren Spins wurde mittels Wenignukleonen-Abstreifreaktionen, insbesondere mit dem C-Target, beobachtet. Somit konnten in diesem Experiment die vielversprechenden Möglichkeiten einer neuen Methode zur Untersuchung der Struktur exotischer Kerne gezeigt werden.

Meinem Sohn Yihan-Philipp Yao

Contents

1	Motivation	1
2	Theoretical background	5
2.1	Coulomb excitation at relativistic energies	5
2.2	Coupled-channels calculations of the inelastic excitation cross sections	9
2.3	Nuclear quadrupole deformation	15
3	The experiment	16
3.1	Experimental particularities	16
3.1.1	Production of the radioactive ion beam (RIB)	16
3.1.2	Doppler effect and angular distribution of γ -rays	18
3.1.3	The atomic background	22
3.1.4	The requirement for the experimental set-up	25
3.2	Set-up in the target area CAVE B	26
3.2.1	The particle detectors	26
3.2.2	The γ -spectrometer Crystal Ball (CB)	32
3.2.3	The neutron detector LAND	34
3.3	Electronics and triggers	36
3.3.1	The electronics of the Crystal Ball (CB)	36
3.3.2	Triggers	37
3.4	Statistics	39
4	Data analysis	41
4.1	Particle identification	41
4.1.1	Charge identification and velocity of particles	41
4.1.2	Mass identification and resolution estimate	44

4.1.3	Charge and mass distribution in front of and behind the target	47
4.2	Scattering angle	50
4.2.1	Scattering angle determination and resolution	51
4.2.2	Scattering angle acceptance	52
4.2.3	Cut on the scattering angle for Coulomb excitation	55
4.3	The γ -spectrometer Crystal Ball (CB)	59
4.3.1	Energy calibration and resolution	59
4.3.2	Doppler correction	60
4.3.3	Time calibration and resolution (source measurement)	62
4.3.4	In-beam time spectra	62
4.3.5	Multiplicity and neighbour add	67
4.3.6	Efficiency	69
4.4	Experimental cross section determination	72
5	Experimental results and comparison with calculations	75
5.1	Fragmentation reactions of ^{28}Mg and ^{43}Ar with the C target	78
5.1.1	Charge-changing cross section $\sigma(\Delta Z)$	78
5.1.2	Isotopic cross section $\sigma(Z_2, A_2)$	80
5.2	Spectroscopic results for the Mg-isotopes	84
5.2.1	Excitation of $^{27,28}\text{Mg}$ with the Pb target	84
5.2.2	Reactions of $^{27,28}\text{Mg}$ with the C target	85
5.3	Spectroscopic results for the Ar-isotopes	91
5.3.1	^{42}Ar with the Pb and C target	91
5.3.2	^{43}Ar with the Pb and C target	92
5.3.3	^{44}Ar with the Pb and C target	96
5.4	Experimental cross sections of γ -transitions and comparison with coupled-channels calculations	99

5.4.1	Experimental cross sections	99
5.4.2	Cross sections from coupled-channels calculations	101
6	Summary and outlook	103
A	The two methods to produce radioactive ion beams (RIB)	106
B	Estimate of $\Delta(B\rho)/(B\rho)_0$ resolution	107
C	Scattering angle determination and resolution	108
D	Properties of electromagnetic transitions	109
	References	111

1 Motivation

In contrast to the nuclear structure along the β -stability line which has been well studied both experimentally and theoretically, the structure of the drip-line nuclei is currently of great interest, especially the question if the magicity of the closed neutron and/or proton shells still persists for the nuclei far from the β -stability line ($^{100}_{50}\text{Sn}^{50}$ and $^{78}_{28}\text{Ni}^{50}$ are two extreme examples.). The emphasis in this work will be on the neutron-rich nuclei below $^{48}_{20}\text{Ca}^{28}$ with neutron number between the two magic neutron numbers $N=20$ and $N=28$.

In the late 70's and 80's, a set of "anomalies" were observed in the semi-magic exotic neutron-rich nuclei with $Z \ll N=20$, including the unexpected ground state spin of ^{31}Na [Hub78] and the extremely low first 2^+ state of ^{32}Mg [Gui84]. These phenomena showed a possible deformation in the closed neutron shell and could not be explained by the standard $2s1d$ shell calculation [Wil80A, Wil83] which had been very successful in the description for the nuclei of the $2s1d$ shell close to stability.

Many variations of shell model had been made in order to explain the "anomalies". One of them was a large-scale shell model calculation including mixing between the $2s1d$ and lower $2p1f$ shells for $N=20$ isotones with $10 \leq Z \leq 20$ [Fuk92]. The calculation showed that, for $Z \leq 14$, the $N=20$ closed-shell structure remains but for $Z \leq 12$, the $N=20$ shell gap vanishes, and the $2s1d$ and $2p1f$ shells melt into one shell because of the strong mixing due to the large imbalance in the neutron and proton numbers. This shell-gap vanishing makes these nuclei much softer towards dynamical deformation. It reproduced the already observed "anomalies" and predicted e.g. an "anomalous" increase of $B(E2: 0^+ \rightarrow 2^+)$ value for ^{32}Mg .

A few years later, by using a radioactive ion beam (RIB) of ^{32}Mg at about 50 A MeV to perform Coulomb excitation with a ^{208}Pb target, the first 2^+ state of ^{32}Mg was studied [Mot95]. A dramatically large deformation of $\beta=0.5$ derived from the large $B(E2)$ value of $454 \text{ e}^2\text{fm}^4$, which is consistent with the theoretical prediction in [Fuk92], thus confirming experimentally the disappearance of the $N=20$ shell gap at $Z=12$.

In the $N=28$ chain theory also predicts strong deformations for the very neutron-rich nuclei like ^{44}S [Wer94]. There is indeed experimental evidence for a rapid weakening of shell effect below ^{48}Ca from the β -decay of very neutron-rich nuclei ^{43}P , $^{42,44,45}\text{S}$, $^{44-46}\text{Cl}$ and ^{47}Ar [Sor95]. But this evidence is rather indirect.

For a long time, the experimental data in the $N=20-28$, $Z < 20$ region were very rare, especially the $B(E2)$ values were missing (see fig. 1) because these exotic nuclei cannot be

produced with useful yields from fusion-evaporation or transfer reactions employing stable beams and targets and it was difficult to produce radioactive ion beams (RIBs) of them. Therefore, it was necessary as well as challenging to perform Coulomb excitation experiment with RIBs to study this region systematically.

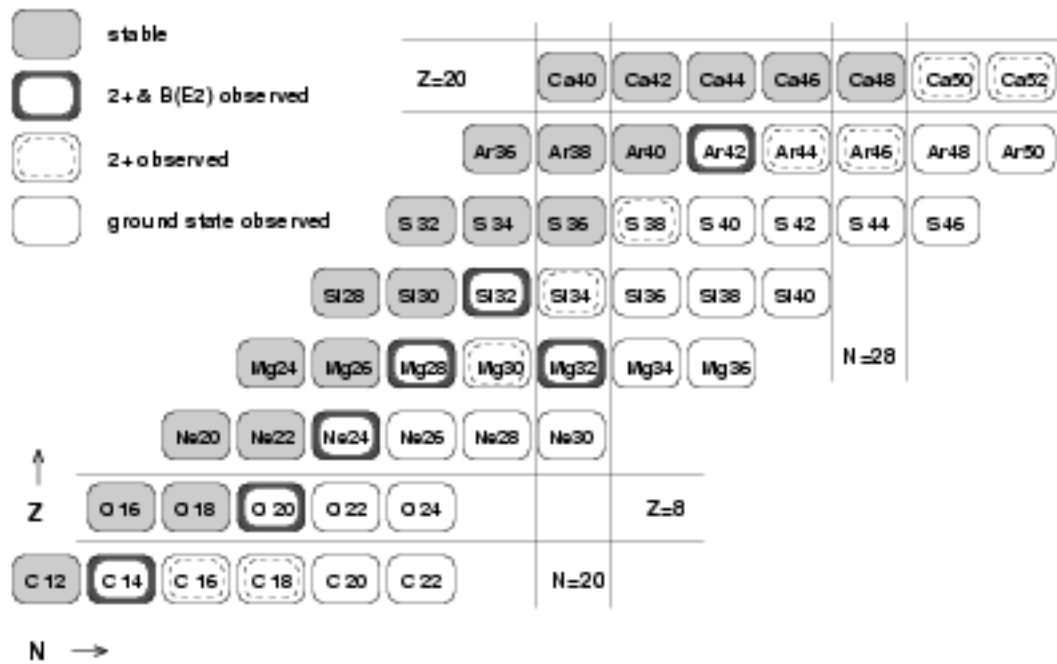


Figure 1: The knowledge of the even-even stable and neutron-rich nuclei in the $N=20-28$, $Z \leq 18$ region till late 1995 [Ajz87, Gui89, End90, Ajz91, Ti93, Aud95, Mot95, Til95, NNDC]. The magic and semi-magic nuclei are marked by lines.

RIBs can be produced in two different ways: by the ISOL (Isotope Separation On-Line) technique [Rav91] or by projectile fragmentation [She91].

The ISOL technique has been developed since the 1960's in order to study nuclei far from stability and has been used in many institutes over the world. The procedure includes five steps: (1) the production of radioactive nuclei by spallation reactions of high-intensity light

projectiles on a thick target, e.g. 100-1000 MeV 10-500 μA protons on 1-300g/cm² targets; (2) the release of radioactive nuclei by high temperature diffusion and/or evaporation (sometimes *Z*-selective) into a catcher; (3) the ionization of radioactive nuclei to some low charge state q^+ (usually $q^+ = 1^+$) by an ion source; (4) the acceleration by an electrostatic field of e.g. 50-300 kV; (5) the isotope separation according to A/q using an electromagnetic mass analyzer. To produce a useful RIB, however, the separated isotopes need to be post-accelerated to higher energies up to 10 AMeV. Several accelerators are presently under construction but not yet in operation. With ISOL technique, high intensity (10^6 to 10^{12} particles per second), good emittance and low energy RIBs from all regions of the nuclide chart will be produced. One of the disadvantages of this method is that, for certain elements, the release from the thick target may be inefficient and/or time consuming, thus the production of RIBs of short-lived isotopes from refractory elements is suppressed.

Projectile fragmentation used e.g. at GSI, GANIL, MSU and RIKEN is a rather newly developed technique to produce RIBs. Primary beams with energies from 50 AMeV to a few AGeV are used to perform fragmentation reactions with up to several g/cm² thick targets like ⁹Be. The radioactive fragments which have large forward momenta with relatively sharp angular distributions peaked near zero degree are suitable to be collected by magnetic devices. By going through an achromatic fragment separator, radioactive nuclei with proper A/q ratio can be selected forming RIBs. The energies of the RIBs range from tens AMeV to a few AGeV. This means they have typical velocities of larger than $\sim 30\%$ of the velocity of light. The intensity for the most abundant isotopes of the RIBs is typically below 1% of the primary beams. For the radioactive nuclei far from stability, the intensity drops sharply. The advantages of this technique are fast separation, no chemical selectivity, relatively simple production targets, beams which do not need reacceleration and can provide different beam species simultaneously. The disadvantages are that, for optimum production the energies have to be generally above the desired energies for many experiments, beam emittances are poor and primary and hence secondary beam intensities are limited.

The comparison between these two methods is shown in table II in appendix A.

Our experiment was made in late 1995 at GSI by the CB-LAND-FRS-Collaboration from GSI, Darmstadt and MPI-K, Heidelberg. After fragmentation reaction of a primary 330 AMeV ⁵⁰Ti beam on a 4g/cm² ⁹Be target, more than 30 neutron-rich isotopes from B to Ca were simultaneously selected by the fragment separator FRS of GSI. To study the excited states of these isotopes, peripheral collisions with secondary Pb and C targets at relativistic energies were employed. The individual beam species and secondary fragments were identified event by event with the $B\rho$ -TOF- ΔE method. De-excitation gamma-rays were detected with the 4π Darmstadt-Heidelberg Crystal Ball spectrometer. Neutrons emitted

from the secondary reactions were detected in LAND (a Large Area Neutron Detector).

In-beam γ -spectroscopy at relativistic energies is a rather untouched field which offers new opportunity to study nuclear structure of exotic nuclei. High velocities of the fragmentation product allow thick targets to be used and in the same time lead to large cross sections. These two factors result in large yields and counteract the usually low intensity of the RIBs of exotic nuclei. Moreover, with relativistic RIBs, different reaction channels can be exploited: (1) Coulomb excitation with the Pb target, from which low-lying low-spin states and giant resonances can be reached; (2) 1 or 2 neutron removal reactions with the Pb or C target, populating high-lying and medium-spin states of the neighbouring nuclei; (3) few neutron and/or proton removal fragmentation reactions with the C target.

On the other hand, with relativistic RIBs, one has to cope with two severe problems which are negligible in the experiments with energies below the Coulomb barrier: Doppler broadening and atomic background. In addition, in order to obtain $B(E2)$ values from Coulomb excitation measurement, nuclear contributions have to be taken into account.

The main motivation of this work was to investigate the feasibility of a pioneering experimental method, namely in-beam γ -spectroscopy employing relativistic radioactive ion beams for the study of the nuclear structure of the neutron-rich nuclei.

2 Theoretical background

Excitation caused by the time-dependent electromagnetic field acting between two colliding nuclei is called Coulomb excitation. Because of its well-understood interaction and reaction mechanism, Coulomb excitation with heavy ions is a powerful tool to study nuclear structure quantitatively.

In the first part of this chapter, Coulomb excitation at relativistic energies, which is rather new in nuclear structure studies, will be treated with emphasis on relativistic effects and the interplay of the nuclear force. In the second part, a coupled-channels approach which is especially developed to calculate cross sections of relativistic inelastic excitation originating from Coulomb and nuclear force, will be introduced. Finally, the formulas to deduce the quadrupole deformation parameter β_2 and the intrinsic quadrupole moment Q_0 from a $B(E2)$ value which is determined by Coulomb excitation will be given.

2.1 Coulomb excitation at relativistic energies

We consider, in the lab system, a projectile nucleus moving along a Z axis with velocity $\beta = v/c$ and a target nucleus being at rest, with Z_i and A_i ($i = p, t$) representing the charge and mass of them. In the following discussion, the length unit will be fm , the energy unit will be MeV .

For collisions with relativistic heavy ions, Coulomb excitation, nuclear excitation and nuclear reactions happen. To assure still pure Coulomb excitation the distance of closest approach of the colliding nuclei must be larger than $(R_p + R_t + \Delta_s)$ with the half-density radius $R_i = 1.28A_i^{1/3} - 0.76$ ($i = p, t$) [Wil80B] and the safety distance $\Delta_s=6.5$ fm for $A_i > 10$ [Boe86]. This is the case for small scattering angles. The trajectories of the projectiles then degenerate to straight lines which are more suitable to be described by impact parameters b instead of scattering angles θ , which also corresponds to the distance of closest approach between the center of mass of the two nuclei.

Several parametrizations of the minimum impact parameter b_{min} (where nuclear and Coulomb excitation probabilities are approximately equal) with respect to the nuclear radii have been proposed within the sharp cut-off approach. One of the most widely used is [Ben89]

$$b_{min} = 1.34(A_p^{1/3} + A_t^{1/3}) - (A_p^{-1/3} + A_t^{-1/3}) . \quad (1)$$

The dimensionless Sommerfeld parameter η for relativistic Coulomb excitation is defined as the ratio between b_{min} and the reduced de Broglie wavelength λ ,

$$\eta = \frac{b_{min}}{\lambda} ,$$

$$\frac{1}{\lambda} = \frac{pc}{\hbar c} = 4.72A_p\gamma\beta, \quad (2)$$

where the velocity β and the Lorentz factor γ of the relativistic projectile can be calculated from the beam energy E_{beam} (in AMeV) as:

$$\begin{aligned} \beta &\equiv \frac{v}{c} = \frac{\sqrt{E_{beam}(E_{beam} + 1863)}}{E_{beam} + 931.5}, \\ \gamma &\equiv \frac{1}{\sqrt{1 - \beta^2}} = 1 + \frac{E_{beam}}{931.5}. \end{aligned} \quad (3)$$

With $\eta \gg 1$, the semi-classical approximation is applicable, i.e. the projectile is considered to move along a classical trajectory which is only determined by the Coulomb force neglecting excitation. With relativistic energies, $1/\lambda$ is large and the condition $\eta \gg 1$ is well satisfied. For example, $\eta \approx 1000$ is obtained for ^{28}Mg projectiles on the ^{208}Pb target with beam energy $E_{beam}=238$ AMeV corresponding to $\beta = 0.60$, $\gamma = 1.26$ and $b_{min}=11.5$ fm, which occurred in our experiment. In the following discussion, this case will always be used as an example.

In the semi-classical approximation, if the target recoil can be neglected, the projectile moving along a straight line will generate a time-dependent electromagnetic field which can be separated into a transversal (\perp) and a longitudinal (z -) component [Jac75,Win79] (see fig. 2):

$$\begin{aligned} \vec{E}_{\perp}(t) &= \frac{-eZ_p\gamma\vec{b}}{(b^2 + \gamma^2v^2t^2)^{3/2}}, & \vec{B}_{\perp}(t) &= \frac{\vec{v}}{c} \times \vec{E}_{\perp}; \\ \vec{E}_z(t) &= \frac{-eZ_p\gamma\vec{v}t}{(b^2 + \gamma^2v^2t^2)^{3/2}}, & \vec{B}_z(t) &= 0. \end{aligned} \quad (4)$$

The momentum transferred to the target nucleus is therefore:

$$\vec{p}_{\perp t} = \int_{-\infty}^{+\infty} eZ_t\vec{E}_{\perp}(t) dt = \frac{2e^2Z_pZ_t}{bv} \left(-\frac{\vec{b}}{b}\right). \quad (5)$$

For $v \rightarrow c$ and $b > b_{min}$, the momentum transfer is found limited to 1 GeV/c resulting in recoil velocities $\beta_{rec} < 0.1$ (in our example, $p_{\perp t} < 410$ MeV/c and $\beta_{rec} < 0.002$), supporting the assumption made in deriving equation (4).

With the projectile momentum $p_p = 931.5A_p\gamma\beta/c$ and $\vec{p}_{\perp p} = -\vec{p}_{\perp t}$, the scattering angle θ of the projectile in the lab system can be obtained

$$\theta(b) \approx \frac{p_{\perp p}}{p_p} = \frac{2e^2Z_pZ_t}{931.5A_p\gamma\beta^2b} = \frac{3.09Z_pZ_t}{A_p\gamma\beta^2b} \times 10^{-3}, \quad (6)$$

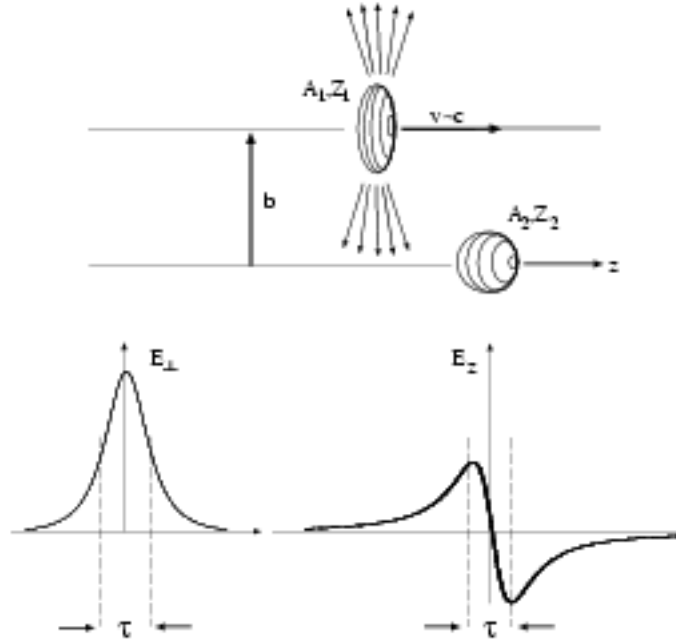


Figure 2: Transversal and longitudinal electrical fields produced by a fast moving projectile in the rest frame of the target nucleus. For relativistic velocity, the trajectory of the projectile with impact parameter larger than the strong interaction radius can be approximated by a straight line.

with b in fm and θ in $radian$. For the minimum impact parameter b_{min} , we find the maximum scattering angle around 1° . In our example, $\theta_{max} = 20.8 \text{ mrad} = 1.2^\circ$. Therefore, the straight-line approach is well justified.

For such small scattering angles θ , the solid angle in the lab system can be expressed approximately as

$$d\Omega \equiv \sin\theta d\theta d\phi \approx \theta d\theta d\phi .$$

The differential cross section in the lab system can therefore be calculated from the excitation probability $P(b)$:

$$\frac{d\sigma}{d\Omega} \equiv P(b) \frac{d\sigma_R}{d\Omega} \approx P(b) \frac{|bdb|d\phi}{\theta d\theta d\phi} = P(b) \frac{b}{\theta} \left| \frac{db}{d\theta} \right| . \quad (7)$$

Here $d\sigma_R = |bdb|d\phi$ is the differential Rutherford cross section for an impact parameter b .

For a Coulomb interaction produced by two moving nuclear charges with collision time τ_{coll} , the width of the Fourier frequency spectrum is $\omega_{coll} = 1/\tau_{coll}$. This gives the observable upper limit of ω_{ph} , the frequency of the photons which are absorbed by the colliding nuclei resulting in excitation with an energy difference of $\Delta E = \hbar\omega_{ph}$. The ratio between ω_{ph} and ω_{coll} is called the adiabaticity parameter ξ . For $\xi > 1$, the transition is getting adiabatic and the excitation probability drops exponentially with ξ . The adiabaticity parameter ξ appropriate for relativistic Coulomb excitation calculations within the straight-line approach is defined as [Win79]:

$$\xi \equiv \frac{\omega_{ph}}{\omega_{coll}} \equiv \frac{\Delta E}{\hbar} \times \tau_{coll} = \frac{\Delta E}{\hbar c} \frac{b}{\gamma\beta}. \quad (8)$$

Requiring $\xi=1$ and $b = b_{min}$, the maximum excitation energy ΔE_{max} can be obtained

$$\Delta E_{max} = \frac{\gamma\beta}{b_{min}} \times 197.3 \text{ (MeV)}. \quad (9)$$

In our example we find $\Delta E_{max} = 13$ MeV. This means, in contrast to Coulomb excitation experiments at “safe” bombarding energies where ΔE_{max} is found to be limited to a few MeV, high-lying states, in particular, the giant resonances can be expected to be strongly populated in relativistic Coulomb excitation studies.

With energies below the Coulomb barrier, pure Coulomb excitation is expected; in collisions at relativistic energies, on the other hand, many other reaction channels open in addition. Therefore, in the theoretical calculation of “unsafe” Coulomb excitation, nuclear excitation and nuclear reactions must also be considered. Usually coupled-channels calculations are used to treat nuclear interactions.

2.2 Coupled-channels calculations of the inelastic excitation cross sections

The relativistic Coulomb excitation induced by heavy projectiles and/or targets may yield large excitation probabilities in grazing collisions where nuclear excitation coexists. Also, theoretical approaches involving perturbation theory may not be applicable. In order to compare with experimental cross sections, therefore, coupled-channels calculations were performed with the computer code CCNUC [Ber96], in which (1) the semi-classical approximation and straight line approach are used; (2) the charge and the mass deformation parameters are assumed to be equal and both amplitudes for Coulomb and nuclear excitations are calculated; (3) the strong absorption at small impact parameters is considered; (4) the Schrödinger equation is solved with the coupled-channels method. Considering only the excitation of the projectile, the main idea of the code will be explained in the following.

The time-dependent state $|\psi(t)\rangle$ satisfies the Schrödinger equation

$$(H + V(\vec{r}(t))|\psi(t)\rangle = i\hbar \frac{\partial}{\partial t} |\psi(t)\rangle, \quad (10)$$

where H is the intrinsic Hamiltonian and V is the external interaction potential. $|\psi(t)\rangle$ can be expanded in a set of eigenstates $\{|m\rangle; m = 0, N\}$ of H

$$|\psi(t)\rangle = \sum_{m=0}^N a_m(t) |m\rangle \exp(-iE_m t/\hbar), \quad (11)$$

where N is the number of excited states to be included in the coupled-channels problem and E_m is the energy of the state $|m\rangle$. Taking the scalar product with each of the states $\langle n|$, the set of coupled equations is obtained

$$i\hbar \dot{a}_n(t) = \sum_{m=0}^N \langle n|V|m\rangle \exp[i(E_n - E_m)t/\hbar] a_m(t) \quad (n = 0 \text{ to } N). \quad (12)$$

In the calculations below, only elastic and a few leading inelastic channels are considered, all others are globally considered as absorption. This is a reasonable approximation because of the very short interaction time.

At impact parameter b larger than b_{min} , Coulomb interaction V^C is dominant. Considering electric dipole ($E1$), magnetic dipole ($M1$) and electric quadrupole ($E2$) excitation modes, the time-dependent matrix element for Coulomb excitation from state $|m\rangle$ to $|n\rangle$ can be written as

$$\langle n|V^C(\vec{r}(t))|m\rangle \equiv V_{nm}^C(\vec{r}(t)) = V_{nm}^{(E1)}(\vec{r}(t)) + V_{nm}^{(M1)}(\vec{r}(t)) + V_{nm}^{(E2)}(\vec{r}(t)). \quad (13)$$

Here the multipole components of the time-dependent matrix element $V_{nm}^{(E1)}$, $V_{nm}^{(M1)}$ and $V_{nm}^{(E2)}$ can be derived from the external electric fields which depend on the trajectory $r(t)$, together with the intrinsic reduced transition probability $B(E1) \uparrow$, $B(M1) \uparrow$ and $B(E2) \uparrow$ respectively. With the semi-classical approximation and straight line approach, $r(t)$ is determined as $r(t) = \sqrt{b^2 + (\gamma vt)^2}$.

As b gets smaller and peripheral collisions occur, the nuclear interaction can also induce excitation. Considering nuclear dipole ($N1$) and quadrupole ($N2$) excitation modes, the time-dependent matrix element for nuclear excitation can be decomposed into two components:

$$\langle n|V^N(r(t))|m\rangle \equiv V_{nm}^N(r(t)) = V_{nm}^{(N1)}(r(t)) + V_{nm}^{(N2)}(r(t)) . \quad (14)$$

Here the matrix element $V_{nm}^{(N\lambda)}$ ($\lambda=1,2$) is calculated from the deformation length δ_λ of the excited projectile and the nuclear optical potential $U_{opt}(r)$. With the assumption that the charge and the mass deformation parameters are equal, δ_λ is related to $B(E\lambda) \uparrow$. For high energy collisions, assuming nucleons are "frozen" during the very short interaction time, $U_{opt}(r)$ can be calculated by folding the nucleon density in the contact region of the two colliding nuclei and then using the nucleon-nucleon cross section.

Inserting Coulomb and nuclear matrix elements (13) and (14) into the set of equations (12) and solving them with the coupled-channels method, the excitation amplitudes a_n ($n = 0$ to N) at $t = +\infty$ are obtained, from which the probabilities for excitation to state $|n\rangle$ ($n = 0$ to N) can be calculated

$$P_n(b) = |a_n(b, t = +\infty)|^2(1 - P_{abs}(b)) , \quad (15)$$

where $P_{abs}(b)$ is the probability of absorption which is strong at small impact parameters. Finally, the total cross section for the excitation of the state $|n\rangle$ is

$$\sigma_n = 2\pi \int_0^{+\infty} P_n(b) b db . \quad (16)$$

Four states of ^{28}Mg , i.e. $0_{gs}^+(0)$, $2^+(1473)$, $0_2^+(3863)$ and $4^+(4020)$ (energies in keV) are included in the coupled-channels calculation. With $B(E2) \uparrow$ values estimated as 338.4, 2.6 and 90.9 $e^2 fm^4$ respectively for transitions $0_{gs}^+ \rightarrow 2^+$, $2^+ \rightarrow 0_2^+$ and $2^+ \rightarrow 4^+$ (refer to chapter 5.4.2), for the reaction with the Pb target, the cross section of populating the three excited states are: $\sigma_{2^+} = 67.7$ mb, $\sigma_{0_2^+} = 0.024$ mb and $\sigma_{4^+} = 0.35$ mb. The excitation to the first excited state $2^+(1473)$ is at least two magnitudes stronger than the others. Therefore multiple excitation is negligible.

As already discussed, with different impact parameter b , different kinds of reactions take place. Here we classify them to three types: (a) absorption including all reactions in which the neutron and/or proton numbers of the projectile ^{28}Mg are changed, (b) inelastic excitation which means that ^{28}Mg is excited from the ground state to any of its excited states, either by nuclear or Coulomb interaction, and (c) elastic scattering in which ^{28}Mg keeps its original intrinsic state. As shown in fig. 3, with small $b \ll R_p + R_t = 9.94$ fm, the absorption probability is 1 (top). As b gets larger, nuclear excitation begins to play a role. It appears only in a narrow region around $R_p + R_t$ because of the absorption on one side and the short-ranged nuclear interactions on the other side. Coulomb excitation starts to coexist with nuclear excitation at $b \approx 9$ fm and takes over at $b \geq b_{min} = 11.5$ fm (middle). Increasing b further, elastic scattering becomes dominant (bottom).

In the middle panel of fig. 3 one may notice that the solid curve, which is obtained from both the Coulomb and nuclear excitation probability, is not a simple sum of its two components. This originates from the interference between the Coulomb and nuclear excitation amplitudes. In the first order perturbation, i.e. if only single-step transitions directly from the ground state $|0\rangle$ to state $|n\rangle$ are considered, the excitation probability can be written as

$$\begin{aligned} P_n(b) &= |a_n^C(b) + a_n^N(b)|^2(1 - P_{abs}(b)) \\ &= [|a_n^C(b)|^2 + |a_n^N(b)|^2 + 2\text{Re}(a_n^C(b)a_n^N(b))](1 - P_{abs}(b)). \end{aligned} \quad (17)$$

The interference term $\text{Re}(a_n^C a_n^N)$ can either be positive or negative. For the excitation to the $2^+(1473)$ state, the interference is negative.

In order to compare the CCNUC calculations with experiment, the differential cross sections for inelastic excitations $\frac{d\sigma}{d\Omega}$ are calculated from $P(b)$. Using formula (6) to our example, the relation between the impact parameter b and the scattering angle θ in the lab system is obtained:

$$\theta(b) \approx \frac{13.7}{b} \text{ degree}.$$

Employing the above relation into formula (7), $\frac{d\sigma}{d\Omega}$ can be deduced

$$\frac{d\sigma}{d\Omega}(b) \approx P(b) \times 175 \times b^4 \text{ mb/sr}.$$

The differential cross section for the transition to the $2^+(1473)$ state $\frac{d\sigma_{2^+}}{d\Omega}(b)$ versus $\theta(b)$ is shown in fig. 4 (top). Coulomb excitation dominates at very forward angles and the nuclear excitation probability overpasses the Coulomb part at angles above $\theta_{max} = 1.2^\circ$. With $\theta \geq 1.4^\circ$, the cross section drops sharply.

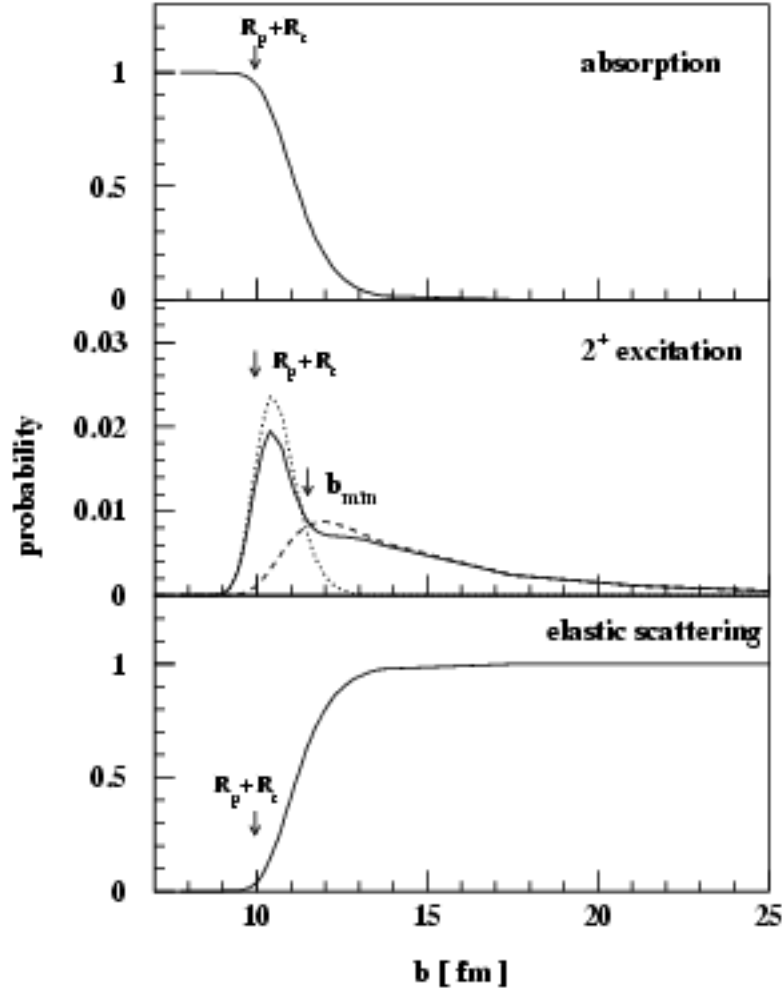


Figure 3: Probability for different kinds of reactions of ^{28}Mg on the Pb target at 238 A MeV, calculated with CCNUC [Ber96]. (a) With $b \ll R_p + R_t$, there is complete absorption. (b) As b gets larger to around $R_p + R_t$, nuclear (dotted curve) and Coulomb (dashed curve) excitation plays a role. The solid curve corresponds to the coherent sum of the Coulomb and nuclear amplitudes. The minimum impact parameter $b_{\text{min}} = 11.5$ fm (where nuclear and Coulomb excitation probabilities are approximately equal) is marked. (c) With $b \gg R_p + R_t$, elastic scattering is dominant.

A similar calculation was performed for the reaction with the C target and $\frac{d\sigma_{2^+}}{d\Omega}$ versus θ is plotted in fig. 4 (bottom). Pure Coulomb excitation exists only in a narrow range of $0^\circ < \theta < 0.1^\circ$. With $\theta > 0.12^\circ$, nuclear excitation quickly exceeds the Coulomb part and reaches its maximum which is about 50 times larger than that of Coulomb excitation. Nuclear excitation in the C target is much stronger than Coulomb excitation because the Coulomb excitation probability is proportional to $\sim Z_t^2$, while the nuclear part scales approximately as $\sim A_t^{1/3}$.

The cross sections for the excitation of the $2^+(1473)$ state of ^{28}Mg are listed in table 1, with σ_C being the cross section for pure Coulomb excitation, σ_N for nuclear excitation and σ_{C+N} the sum of both considering the interference term. For the reaction with the Pb target, with an integration range of $b_{\min} < b < +\infty$, the total cross section σ_{C+N} is dominated by Coulomb excitation, while with $0 < b < +\infty$, the nuclear excitation accounts for about 30%. For the reaction with the C target, the contribution from Coulomb excitation is negligibly small.

Table 1: The cross sections (in mb) to populate the $2^+(1473)$ state of ^{28}Mg calculated from CCNUC assuming $B(E2) \uparrow = 338.4 e^2 fm^4$. See text for details.

reaction	$^{28}\text{Mg}+\text{Pb}$	$^{28}\text{Mg}+\text{Pb}$	$^{28}\text{Mg}+\text{C}$
range of b	$(b_{\min}, +\infty)$	$(0, +\infty)$	$(0, +\infty)$
σ_{C+N}	49.5	67.7	11.6
σ_C	51.3	56.6	1.1
σ_N	2.3	23.5	12.3

Therefore, if a scattering angle $\theta < \theta_{\max}$ (i.e. $b > b_{\min}$) is required, nuclear excitation can be strongly suppressed and the cross section measured with the Pb target can be taken as that of pure Coulomb excitation and be used to derive $B(E2)$ values. If a constraint on θ is not available, the contribution from nuclear excitation can be constructed on the basis of the cross section measured with the C target. That is the main reason why in our experiment, the scattering angle θ was measured and the measurement with the C target was performed in addition to the Pb target.

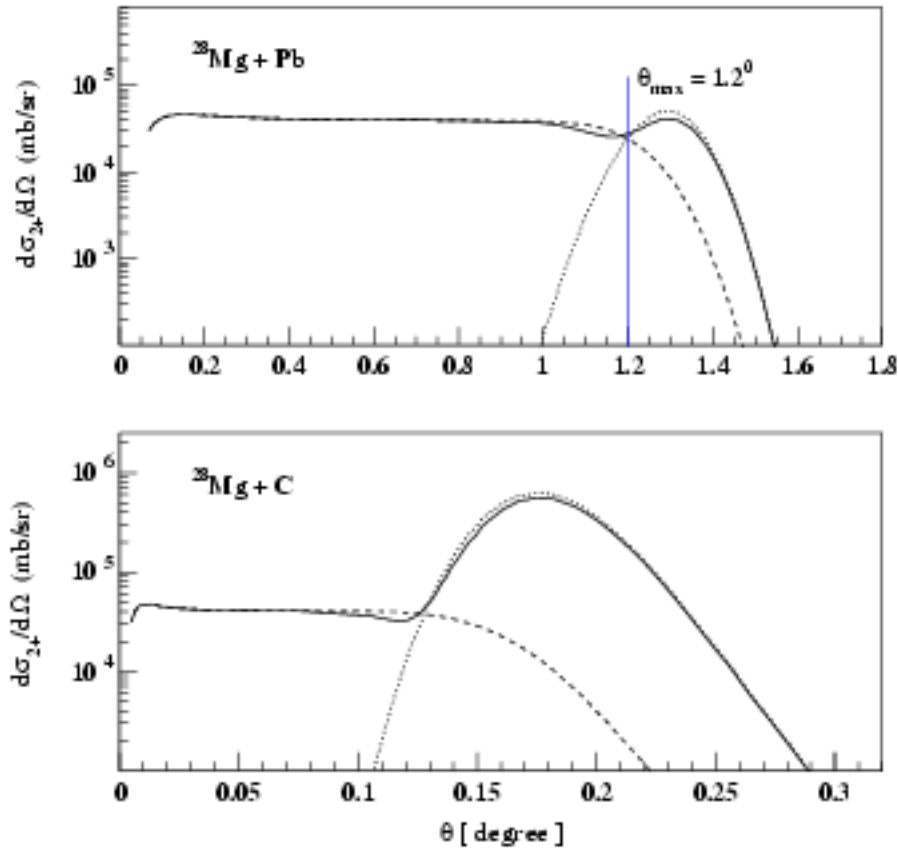


Figure 4: The calculated differential cross section $\frac{d\sigma_{2^+}}{d\Omega}(\theta)$ for the transition to the $2^+(1473)$ state of ^{28}Mg on the Pb (top) and C (bottom) target at 238 A MeV. The dotted and dashed curves indicate the nuclear and Coulomb parts, respectively. The solid curve corresponds to the coherent sum of the nuclear and Coulomb amplitudes. The maximum scattering angle in the lab system θ_{max} , where nuclear and Coulomb excitation probabilities are approximately equal, is marked for the Pb target.

2.3 Nuclear quadrupole deformation

The most direct and unambiguous measure of quadrupole deformation is the E2 properties derived from Coulomb excitation cross sections. In first order, $B(E2)$ values are proportional to Coulomb excitation cross sections. The quadrupole deformation β_2 and the intrinsic electric quadrupole momentum Q_0 of the nuclear ground state in even-even nuclei can be deduced from the $B(E2) \uparrow$ value to the first 2^+ state by using the following relation [Ram88]:

$$\begin{aligned}\beta_2 &= \frac{4\pi}{3Z} \left[\frac{B(E2) \uparrow}{e^2 R_0^4} \right]^{1/2}, \\ Q_0 &= \left[\frac{16\pi}{5} \frac{B(E2) \uparrow}{e^2} \right]^{1/2},\end{aligned}\quad (18)$$

with $B(E2) \uparrow$ in $e^2 fm^4$ and $R_0 = 1.2A^{1/3} fm$.

Between $B(E2)$ value and mean life time τ , there is the following relation:

$$B(E2) \downarrow = \frac{1}{1.22 \times 10^9} \frac{1}{(\alpha + 1) E_\gamma^2 \tau}, \quad (19)$$

where α is the total conversion coefficient. With the relation between $B(\lambda) \uparrow$ (excitation) and $B(\lambda) \downarrow$ (decay)

$$B(\lambda) \uparrow = B(\lambda, I_i \rightarrow I_f) = \frac{2I_f + 1}{2I_i + 1} B(\lambda, I_f \rightarrow I_i) = \frac{2I_f + 1}{2I_i + 1} B(\lambda) \downarrow, \quad (20)$$

i.e. for E2 transition between ground state $0_{g.s.}^+$ and 2_1^+

$$B(E2, 0_{g.s.}^+ \rightarrow 2_1^+) = 5 \times B(E2, 2_1^+ \rightarrow 0_{g.s.}^+), \quad (21)$$

$B(E2) \uparrow$ can be calculated from τ (partial mean life time)

$$B(E2, 0_{g.s.}^+ \rightarrow 2_1^+) \uparrow = \frac{4.1 \times 10^{-9}}{(\alpha + 1) E_\gamma^2} \frac{1}{\tau}, \quad (22)$$

with τ in second, E_γ in MeV and $B(E2)$ in $e^2 fm^4$. β_2 can therefore be obtained via formula (18). This is another method to measure the quadrupole deformation of a nucleus.

3 The experiment

In-beam γ -spectroscopy with relativistic radioactive ion beams is a new method for nuclear structure studies. Therefore in this chapter, first of all, the experimental particularities of this method will be discussed. After that, the experimental set-up, including all the particle detectors, the γ -detector CB and the neutron detector LAND, will be described. In the third part, the electronics of the CB and the different experiment triggers will be introduced. At the end, an overview of the statistics of the experiment will be given.

3.1 Experimental particularities

The experimental particularities, including (1) the procedure to produce the Radioactive Ion Beam (RIB), (2) the Doppler effect, (3) the atomic background and (4) the requirement for the experimental set-up, will be explained in this section.

3.1.1 Production of the radioactive ion beam (RIB)

The procedure to produce the RIB at the SIS-FRS facility is shown in fig. 5.

A low-energetic, partly ionized, continuous ^{50}Ti beam pre-accelerated by UNILAC (UNiversal Linear ACcelerator) passed through a thin carbon foil to become fully ionized and was then injected into SIS (“SchwerIonen Synchrotron” which means “heavy ion synchrotron”) for further acceleration. Within about 2.9 seconds, the ions were accelerated to 330 A MeV and then extracted from SIS within a spill time of about 0.9 second. The intensity of the fully ionized $^{50}\text{Ti}^{22+}$ primary beam in our case was up to 10^9 particles per spill, i.e. on the average about 2×10^8 particles per second.

The relativistic $^{50}\text{Ti}^{22+}$ primary beam from SIS underwent fragmentation reactions in a 4 g/cm^2 ^9Be primary target and a full variety of nuclei lighter than ^{50}Ti were produced. By setting the magnetic rigidity of the bending magnets at FRS (FRagment Separator) to $B\rho = 5.588 \text{ Tm}$, about 50 different nuclear species from $Z = 4 - 20$ were selected with $A/Z \approx 2.1 - 2.5$ and energies ranging from 210 to 280 A MeV ($\beta \approx 0.58 \sim 0.64$). After about 250 meters (transmission $\approx 15 - 20\%$), the RIB reached the target area CAVE B with an intensity of around 10^4 particles per second for the full composition of nuclear species i.e. on the average about 200 particles per second for each nuclear species (see also fig. 19 in chapter 4.1.3). For example, the intensity for the nucleus ^{38}S for which the transmission was optimized was about 300 particles per second. Fig. 6 shows the time structure of the RIB measured at the entrance of CAVE B.

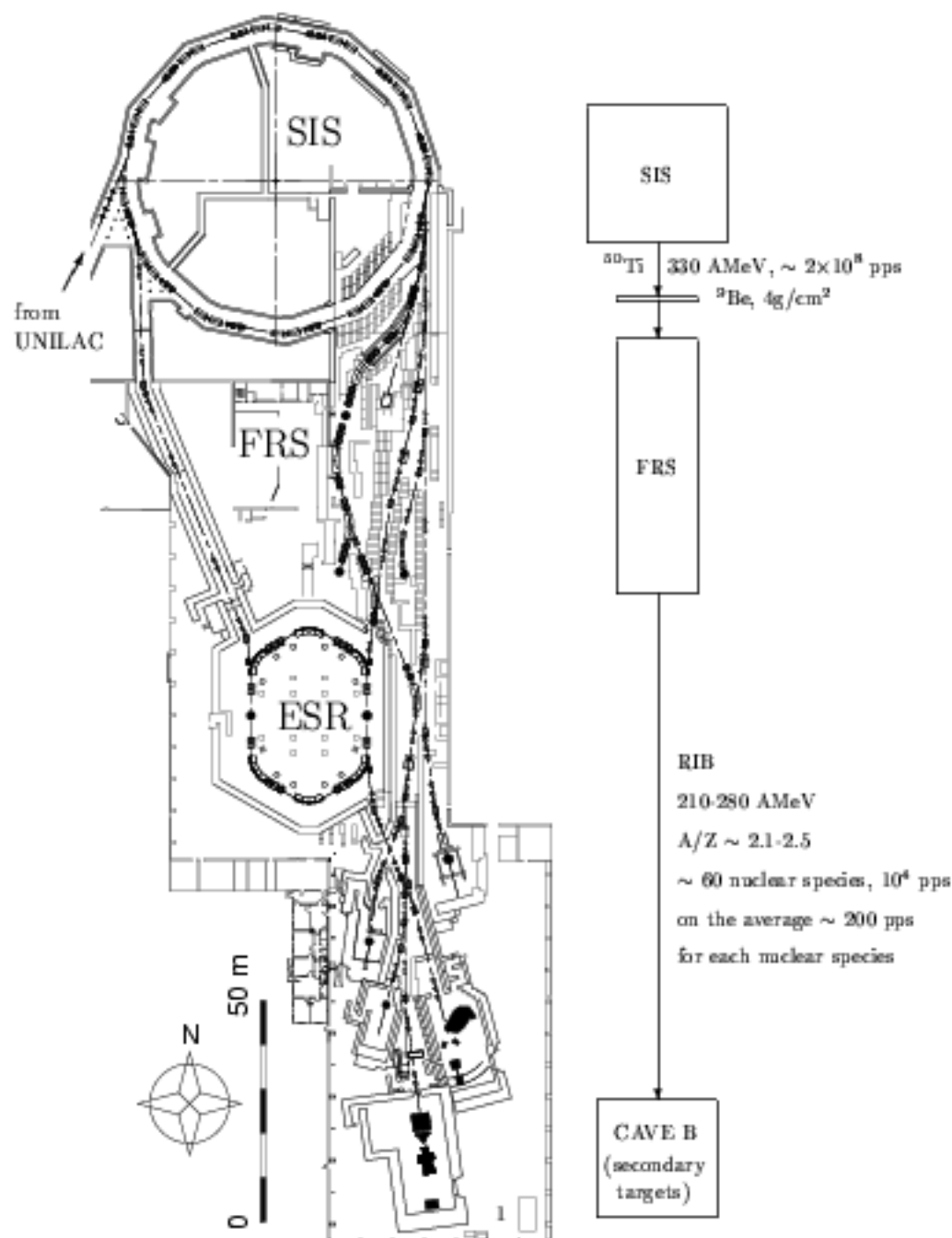


Figure 5: The procedure to produce the RIB for our experiment was as follows: the ^{50}Ti beam was pre-accelerated by UNILAC and further accelerated to relativistic energies by SIS; after fragmentation reactions with a 4g/cm^2 ^9Be target at the entrance of FRS, a full variety of nuclei lighter than ^{50}Ti were produced and then about 50 nuclear species with similar A/Z ratio were selected by FRS; finally being focused and guided by the dipole- and quadrupole-magnets on the beam-line, the RIB was transmitted to the experimental area CAVE B to perform secondary reactions. The transmission from the FRS to CAVE B was 15 – 20%.

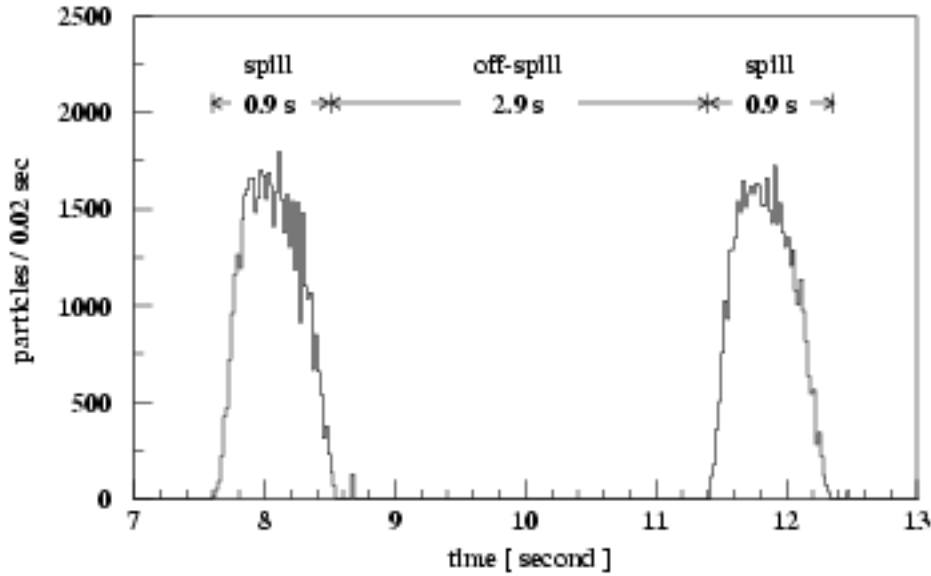


Figure 6: Time structure of the RIB measured at the entrance of CAVE B. The spill repetition time is around 3.8 seconds with about 0.9 second spill length. The beam intensity is about 5×10^4 particles per spill, i.e. on the average 1.3×10^4 particles per second.

Using relativistic RIBs, we have to cope with two severe problems: Doppler effect and atomic background. In the following we discuss them using an example from the experiment: ^{43}Ar on ^{208}Pb and ^{12}C targets with a beam energy of $E_{\text{beam}} = 222$ AMeV in the lab system, corresponding to a velocity of $\beta = 0.59$ and Lorentz factor $\gamma = 1.24$ (refer to formula (3) in chapter 2.1).

3.1.2 Doppler effect and angular distribution of γ -rays

Gamma-rays emitted from the excited projectiles moving with high velocity $\beta = 0.59$ will be strongly Doppler shifted according to the following formula [Pel82]:

$$E_{\gamma}^{\text{lab}} = E_{\gamma} \frac{\sqrt{1 - \beta^2}}{1 - \beta \cos \theta_{\gamma}} \quad (23)$$

where E_{γ} is the de-excitation γ -energy for the projectile at rest (in our case the coordinate system is attached to the moving projectile), E_{γ}^{lab} is the Doppler shifted γ -energy detected in the lab system, θ_{γ} is the angle between the γ -ray and the projectile in the lab system. Because of the very small scattering angle of high velocity projectiles (below

2°), we can take the angle between the γ -ray and the beam direction as θ_γ in order to simplify the calculation. This approximation will be always taken in the following discussions.

Fig. 7 (a) shows the Doppler shift, from which we can see, at forward direction ($\theta_\gamma = 0^\circ$), $E_\gamma^{lab} \approx 2E_\gamma$ while at backward direction ($\theta_\gamma = 180^\circ$), $E_\gamma^{lab} \approx \frac{1}{2}E_\gamma$.

To correct the Doppler shift, i.e., to get the original γ -energy E_γ from the detected E_γ^{lab} , β and θ_γ must be determined precisely. β can be derived with an accuracy of better than 1% (see chapter 4.1.1), but the accuracy of θ_γ is worse because of the opening angle of common γ -detectors. Using a detector with a diameter of 8 cm at a distance of 25 cm from the target, the opening angle of the detector is $\Delta\theta_\gamma \approx 18^\circ$. This results in the uncertainty ΔE_γ to determine the original γ -energy E_γ :

$$E_\gamma \pm \frac{1}{2}\Delta E_\gamma = E_\gamma^{lab} \frac{1 - \beta \cos(\theta_\gamma \pm \frac{1}{2}\Delta\theta_\gamma)}{\sqrt{1 - \beta^2}} \quad (24)$$

From equations (23) and (24), we get:

$$\frac{\Delta E_\gamma}{E_\gamma} \approx \frac{\sin\theta_\gamma}{1 - \beta \cos\theta_\gamma} \beta \Delta\theta_\gamma \quad (25)$$

The uncertainty of the original γ -energy $\Delta E_\gamma/E_\gamma$ caused by the high velocity β of the projectile and the opening angle of detector $\Delta\theta_\gamma$ is called Doppler broadening.

Fig. 7 (b) shows the Doppler broadening for $\beta = 0.59$ and $\Delta\theta_\gamma = 18^\circ$. The Doppler broadening reaches values up to 23% at $\theta_\gamma \approx 55^\circ$ while in the forward and especially backward region the broadening is smaller.

In order to find the optimal positions for the γ -detectors, besides Doppler broadening, we must also take the angular distribution of the γ -rays into account.

First we need the Lorentz transformation with the assumption of the projectile scattering angle $\theta = 0^\circ$ [Pel82]:

$$\begin{aligned} \phi_\gamma^{rest} &= \phi_\gamma \\ \cos\theta_\gamma^{rest} &= \frac{\cos\theta_\gamma - \beta}{1 - \beta \cos\theta_\gamma} \end{aligned} \quad (26)$$

where ϕ_γ^{rest} and θ_γ^{rest} are γ -ray emission angles in the rest system of the projectile while ϕ_γ and θ_γ are in the lab system. In both systems the Z-axis is equal to the beam axis. From this we can get the relation between the solid angles in the rest system and the lab system:

$$\frac{d\Omega_{rest}}{d\Omega} = \frac{1 - \beta^2}{(1 - \beta \cos\theta_\gamma)^2} \equiv \left(\frac{E_\gamma^{lab}}{E_\gamma}\right)^2 \quad (27)$$

^{43}Ar on the Pb target with $E_{\text{beam}} = 222 \text{ A MeV}$, $\beta = 0.59$

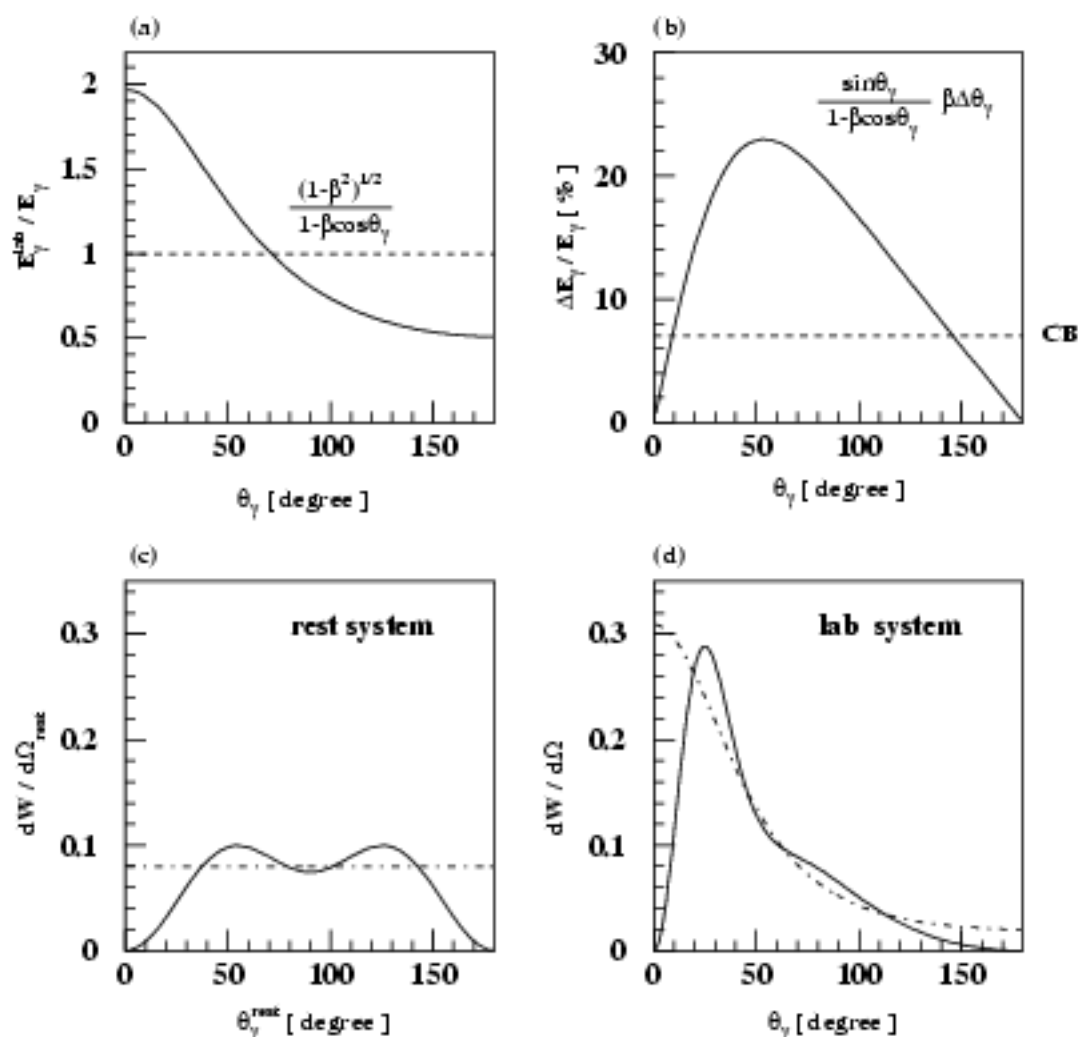


Figure 7: (a) Doppler shift, (b) Doppler broadening assuming an opening angle of 18° for one detector element (the 7% intrinsic energy resolution of the CB is marked by the dashed line), (c) angular distribution of γ -rays in the rest system and (d) in the lab system (after the Lorentz transformation). The angular distribution of γ -rays in the lab system is peaked at forward angles where Doppler broadening is rather severe.

Then we can transform the angular distribution from the rest system into the lab system:

$$\frac{dW}{d\Omega}(\theta_\gamma) = \frac{1 - \beta^2}{(1 - \beta \cos\theta_\gamma)^2} \frac{dW}{d\Omega_{rest}}(\theta_\gamma^{rest}) \quad (28)$$

We start by simply assuming an isotropic angular distribution in the rest system:

$$\frac{dW}{d\Omega_{rest}}(\theta_\gamma^{rest}) = \frac{1}{4\pi} \quad (29)$$

The distribution is normalized to 1 for the 4π integration. From equations (28) and (29), we get the relevant angular distribution in the lab system:

$$\frac{dW}{d\Omega}(\theta_\gamma) = \frac{1}{4\pi} \frac{1 - \beta^2}{(1 - \beta \cos\theta_\gamma)^2} \quad (30)$$

Taking the angular distribution of γ -rays of a $I \rightarrow I - 2$ quadrupole transition from Coulomb excitation populating the magnetic sub-state $m = 0$ and assuming a projectile scattering angle $\theta = 0^\circ$, in the rest system we get [Wol93]:

$$\frac{dW}{d\Omega_{rest}}(\theta_\gamma^{rest}) = \frac{1}{4\pi} [1 + a_2 P_2(\cos\theta_\gamma^{rest}) + a_4 P_4(\cos\theta_\gamma^{rest})] \quad (31)$$

with

$$\begin{aligned} a_2 &= -\frac{5}{14} \frac{I+1}{2I-1} \\ a_4 &= -\frac{9}{56} \frac{(I+1)(I+2)}{(2I-3)(2I-1)} \end{aligned}$$

where the Legendre polynomials are $P_0(x)=1$, $P_2(x)=\frac{1}{2}(3x^2-1)$, $P_4(x)=\frac{1}{8}(35x^4-30x^2+3)$ [Bro87]. For a $2^+ \rightarrow 0^+$ transition, the angular distribution in equation (31) is simplified as:

$$\frac{dW}{d\Omega_{rest}}(\theta_\gamma^{rest}) = \frac{1}{4\pi} \frac{15}{16} (1 + 2\cos^2\theta_\gamma^{rest} - 3\cos^4\theta_\gamma^{rest}) \quad (32)$$

From equations (28) and (32), we get the angular distribution for a $2^+(m=0) \rightarrow 0^+$ transition in the lab system:

$$\frac{dW}{d\Omega}(\theta_\gamma) = \frac{1}{4\pi} \frac{1 - \beta^2}{(1 - \beta \cos\theta_\gamma)^2} \frac{15}{16} (1 + 2\cos^2\theta_\gamma^{rest}(\theta_\gamma) - 3\cos^4\theta_\gamma^{rest}(\theta_\gamma)) \quad (33)$$

With $\beta = 0.59$, the angular distributions of γ -rays in the rest system and the lab system are illustrated in fig. 7 (c), (d) respectively. The dashed line stands for the simple isotropic distribution and the solid line represents the distribution for a $2^+ \rightarrow 0^+$ transition. In both cases, the angular distribution of γ -rays in the lab system is peaked at forward angles. In this region, however, the Doppler broadening is large.

From fig. 7 (b) and (d), we can determine an average Doppler broadening of about 15%. This large Doppler broadening favors the use of scintillating detectors like the Crystal Ball composed of NaI's with a typical intrinsic energy resolution of about 8% at 1.3 MeV and large full energy peak efficiencies, instead of Ge detectors whose much better energy resolution (but worse efficiency) does not fit the experiment with relativistic energies if they are not segmented to allow for a better resolution in θ_γ .

3.1.3 The atomic background

The main atomic processes in the experiments with relativistic RIBs are [Anh84, Anh86, Hol92]:

- (1) K and L X-rays from ionized target atoms;
- (2) radioactive electron capture (REC) of the target electrons into the projectile K and/or L shells;
- (3) primary Bremsstrahlung (PB) from target electrons scattering off the projectile;
- (4) secondary Bremsstrahlung (SEB) from energetic knock-on electrons re-scattering in the target and/or the surrounding material.

The cross sections of all these processes depend strongly on projectile and target charges, in particular does PB scale with $Z_p^2 Z_t$ and SEB with $Z_p^2 Z_t^2$.

Based on experimental results, the double differential cross section $d^2\sigma/dEd\Omega$ of the above 4 atomic processes with ^{43}Ar beam on Pb and C targets at 222 AMeV can be calculated empirically [Hol97]. From the calculation we get the following properties for this particular reaction.

K and L X-rays are discrete lines below 100 keV. REC produces broad peaks around 100 keV but they are Doppler shifted to a broad structure from 50 keV to 250 keV at $\beta = 0.59$. PB and SEB are continuum spectra which are dominant at higher photon energies. PB can reach about 350 keV. Because of the Doppler effect, this value shifts to 180 keV at backward direction and 700 keV at forward direction. SEB distributes to even higher energies and reaches up to the maximum electron knock-on energy given (classically) by $E_{max} = 2\gamma^2\beta^2 m_e c^2$ which is 541 keV at $E_{beam} = 222$ AMeV.

Table 2: Properties of the main atomic processes at $E_{beam} = 222$ AMeV.

atomic process	energy range	Doppler shift	energy distribution	angular distribution $d\sigma/d\Omega$ in lab	charge dependence
X-rays	< 100 keV	no	discrete lines	isotropic	yes
REC	~ 100 keV	50-200 keV	broad peak(s)	$\sim \sin^2\theta_\gamma$	yes
PB	≤ 350 keV	200-700 keV	continuum	$\sim \sin^2\theta_\gamma(1 - \beta\cos\theta_\gamma)$	$Z_p^2 Z_t$
SEB	≤ 540 keV	no	continuum	isotropic	$Z_p^2 Z_t^2$

The angular distribution of X-rays and SEB is isotropic, while it shows approximately a $\sin^2\theta_\gamma$ and $\sin^2\theta_\gamma(1 - \beta\cos\theta_\gamma)$ dependence respectively for REC and PB, where θ_γ is the laboratory angle between the beam and the photons. The reason why REC and PB are not forward-shifted is that the retardation effect which shifts the distribution backwards cancels the Doppler transformation [Spi79].

All these properties are shown in table 2.

Fig. 8 illustrates the angle-integrated cross section from the calculation. At around 75 and 85 keV, X-rays from the Pb target can be seen but not for the C target because the energies of its X-rays are too low (below 1 keV). We can also see the cross section is two magnitudes bigger for the Pb target than for the C target because of their different charge number Z_t . In both cases, the cross sections are quite large at low energy but decrease sharply as the energy increases and then drop down at around 540 keV corresponding to the maximum electron knock-on energy for SEB. The small tails at higher energy are Doppler shifted PB.

The angle- and energy-integrated cross section is 28 kbarn for the Pb target and 200 barn for the C target which is at least 3 orders of magnitude larger than typical Coulomb excitation and nuclear reaction cross sections. If we integrate over energies above 500 keV, we get 240 mb for the Pb target and 0.43 mb for the C target.

The atomic background is huge and must be suppressed. For the low energy part (about ≤ 100 keV) with cross sections ranging from tens to one thousand barn, an appropriate absorber should be used in front of the γ -detectors in order to avoid pile up. For the atomic background with higher energies but lower cross sections, a proper threshold like 500 keV could be set to the trigger. This will not disturb the γ -spectra because the excitation energies of the light nuclei which we are interested in are above 1 MeV. In addition, selective

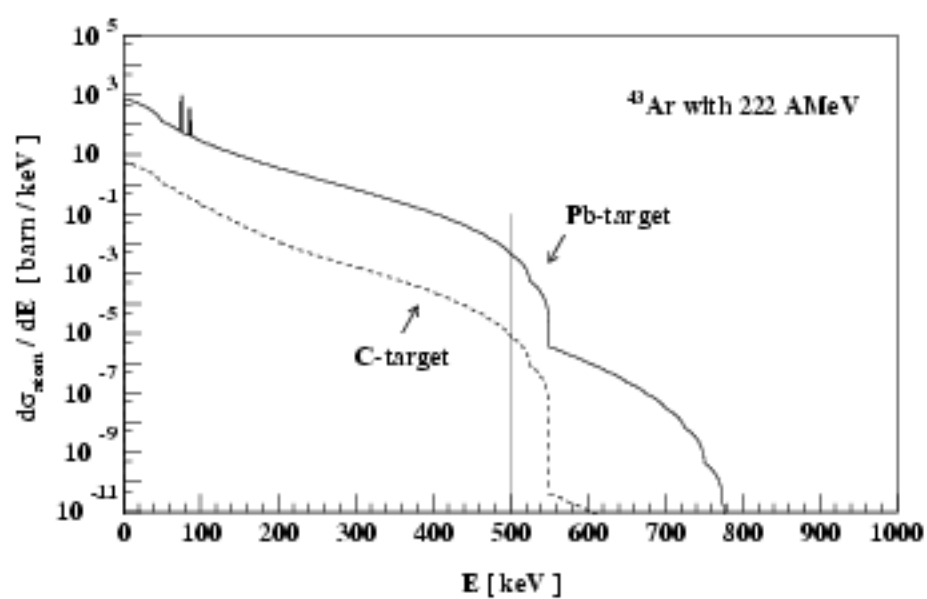


Figure 8: Angle-integrated cross section of the atomic background from ^{43}Ar on the Pb (solid line) and C target (dashed line) at 222 AMeV. The 500 keV detection threshold of the NaIs of the CB used in the experiment is marked.

trigger also helps to suppress the atomic background, e.g. by requiring a minimal scattering angle or neutron coincidence to get rid of pure atomic background which is associated with large impact parameters and not accompanied by neutron emission.

3.1.4 The requirement for the experimental set-up

Because the relativistic RIB was not well focused, veto counters were necessary to veto on the beam halo. The charge and mass number Z_1 and A_1 of the different nuclear species which were simultaneously selected in the RIB must be identified even by event. With relativistic energies, different reactions, e.g. Coulomb excitation, nuclear excitation, few nucleon removal reactions as well as fragmentation, may take place with the secondary target. Therefore, the charge and mass number Z_2 and A_2 of the secondary reaction product also need to be identified.

However, the above information is not sufficient to distinguish Coulomb and nuclear excitations which are both inelastic excitations and satisfy the condition of $Z_2=Z_1$ and $A_2=A_1$. Cut on scattering angle of $\theta < \theta_{\text{max}} \approx 1^\circ$ might be helpful to suppress the nuclear part (see chapter 2.2). Moreover, requiring a minimal scattering angle helps to suppress the atomic background. Therefore, the trajectories of the beam-like particles in front of and behind the secondary target were measured event by event in order to determine scattering angles. These trajectories are also needed for A_2 determination.

For γ -spectroscopy employing RIBs at relativistic energies, the Crystal Ball is well suited because its intrinsic energy resolution of about 8% is well matched to the Doppler broadening and, moreover, its 4π solid angle and large full energy efficiency $\varepsilon_{fe} \approx 70\%$ at 1.3 MeV compensate for the low beam intensity.

Giant resonances with excitation energies above 10 MeV are also expected to be populated in relativistic Coulomb excitation (see chapter 2.1). In order to measure the neutrons evaporated from giant resonances, the high efficiency neutron detector LAND was employed.

3.2 Set-up in the target area CAVE B

The experimental set-up in the target area CAVE B consisted of three types of detectors as shown in fig. 9:

- particle detectors:
 - (1) two-dimensional position detectors ZST01, ZST02 and ZST03 to determine the trajectory of the particles in front of and behind the target;
 - (2) start detector POS01 to generate the common time reference;
 - (3) veto-counters HALO and ROLU to veto on the beam halo;
 - (4) ΔE counters PIN01 and PIN02 to identify charge number Z_1 and Z_2 in front of and behind the target;
 - (5) one-dimensional position detectors GFI01 and GFI02 behind ALADIN (A LArge DIpole magNet) to determine the deflection angle, from which the mass number A_2 behind the target can be derived by the ΔE - $B\rho$ -TOF method.
 - (6) TOF-wall to measure the time of flight from which particle velocities and the mass number A_1 in front of the target can be derived.

- the γ -spectrometer CB with the secondary target at the center;
- the neutron detector LAND with a veto detector in front.

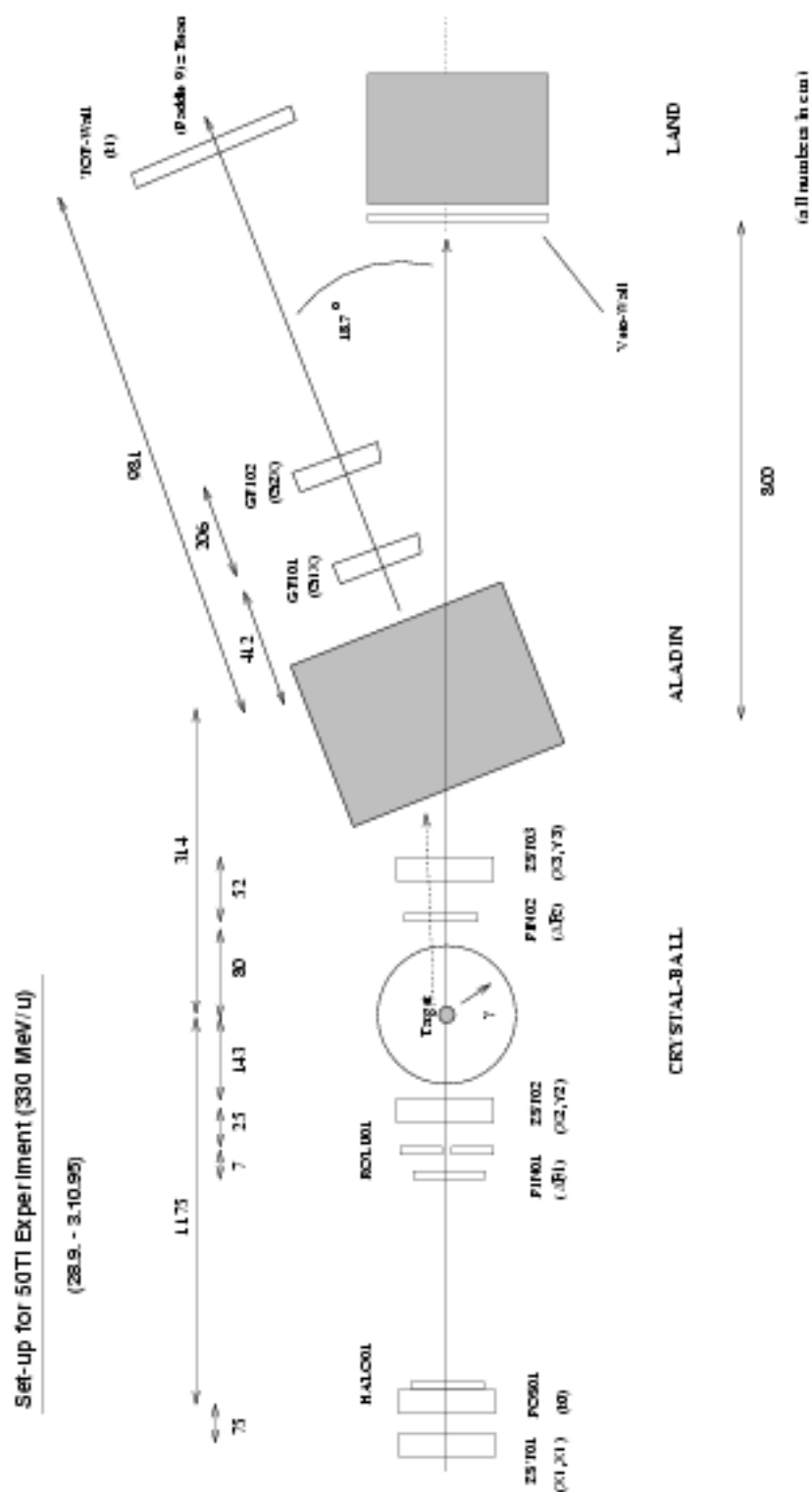
The beam and the particle detectors were kept in vacuum till PIN02 (including).

3.2.1 The particle detectors

(1) ZST01, ZST02 and ZST03

These are MultiWire Proportional Chambers MWPC developed for the detection of heavy ions at relativistic energies and for beam monitoring [Ste91]. In our experiment they were used to determine the trajectory of the ion before and after the secondary target. ZST01 and ZST02 in front of the target have a size of 9×9 cm² and a thickness of 5 cm (8.3 mg/cm²) while ZST03 behind the target has a size of 20×20 cm² and a thickness of 10 cm.

A schematic layout of a two-stage MWPC is shown in fig. 10. The planar anode A consists of $20\mu\text{m}$ gold-plated tungsten wires with a pitch of 2 mm; the cathodes X and Y are made of $50\mu\text{m}$ gold-plated tungsten wires with a pitch of 1 mm. The wire directions in X and Y are orthogonal to each other, while that in A is diagonal to them. The planar mesh electrodes T and G are made of woven fabrics of plastic and coated with a nickel layer. Typical potentials applied to the planar electrodes are: $U_G = -10$ kV, $U_T = -2.6$ kV, $U_A = +2.5$ kV. The

Figure 9: Set-up for the ^{50}Ti experiment in the target area CAVE B.

readout planes X and Y are on ground. A gas mixture consisting of 80% argon, 19% CO₂ and 1% heptane with a pressure of 1 atmosphere was used during the experiment.

The primary electrons produced by the particles hitting the active area of the chamber are pre-amplified in the electric field between G and T by a factor of 10^2 . The avalanche then drifts through the transfer gap between T and X. With 15% transfer efficiency, the electrons arrive in the amplifier gap between X and A and are amplified by a factor of 10^3 till they reach the anode A.

The electron avalanche causes negative signal on the anode A and induces positive signals on the adjacent wires in the X and Y cathodes. These signals can be used to determine the two-dimensional position of the incoming particle. Each wire of the planes X and Y is connected to a tap of a delay line with a delay of 4 ns per tap. The signal propagates through the left and the right side of the delay line. At both ends of the delay line the signals are amplified and fed in the STOP of a TDC while the START signal for the TDC is derived from the anode. The time difference between the left and the right side of the delay line is a measure of the position; whereas the sum of left and right (delay-sum) should be a constant, namely the total length of the delay line ($\sim 1 \mu\text{s}$, depending on the number of wires of the X and Y planes). To avoid pile up, the particle rate should not exceed 100 kHz.

By requiring a constant delay-sum, the spatial resolution of ZST01 in both coordinates was 1.5 mm with an efficiency of 90% for $Z \geq 8$. For ZST02, however, nearly half of events had a delay-sum smaller than the constant. The reason might be that the delay line signal from ZST02 may not have been properly shaped causing ambiguous times from the CFD's. The efficiency of ZST02 was therefore reduced to about 50% if a constant delay-sum was required in order that the 1.5 mm spatial resolution could be achieved. For ZST03, the resolution was 3 mm and the efficiency depended strongly on the charge number Z because of the high threshold to suppress noise. For the two extreme cases of $Z = 8$ and 18, the efficiency of ZST03 was less than 10% and around 75%, respectively. Because of this, ZST03 was not used to determine scattering angles of light particles. Instead, information from GFI01, GFI02 and the TOF-wall was used.

(2) POS01

It is a circular plastic scintillator at the entrance of CAVE B with a diameter of 10 cm and a thickness of 0.350 mm (36.1 mg/cm²). With a good time resolution of around 100 ps (FWHM), it serves as the start detector for the time-of-flight measurement and, moreover, determines the common START respectively STOP for all TDCs used.

(3) HALO and ROLU

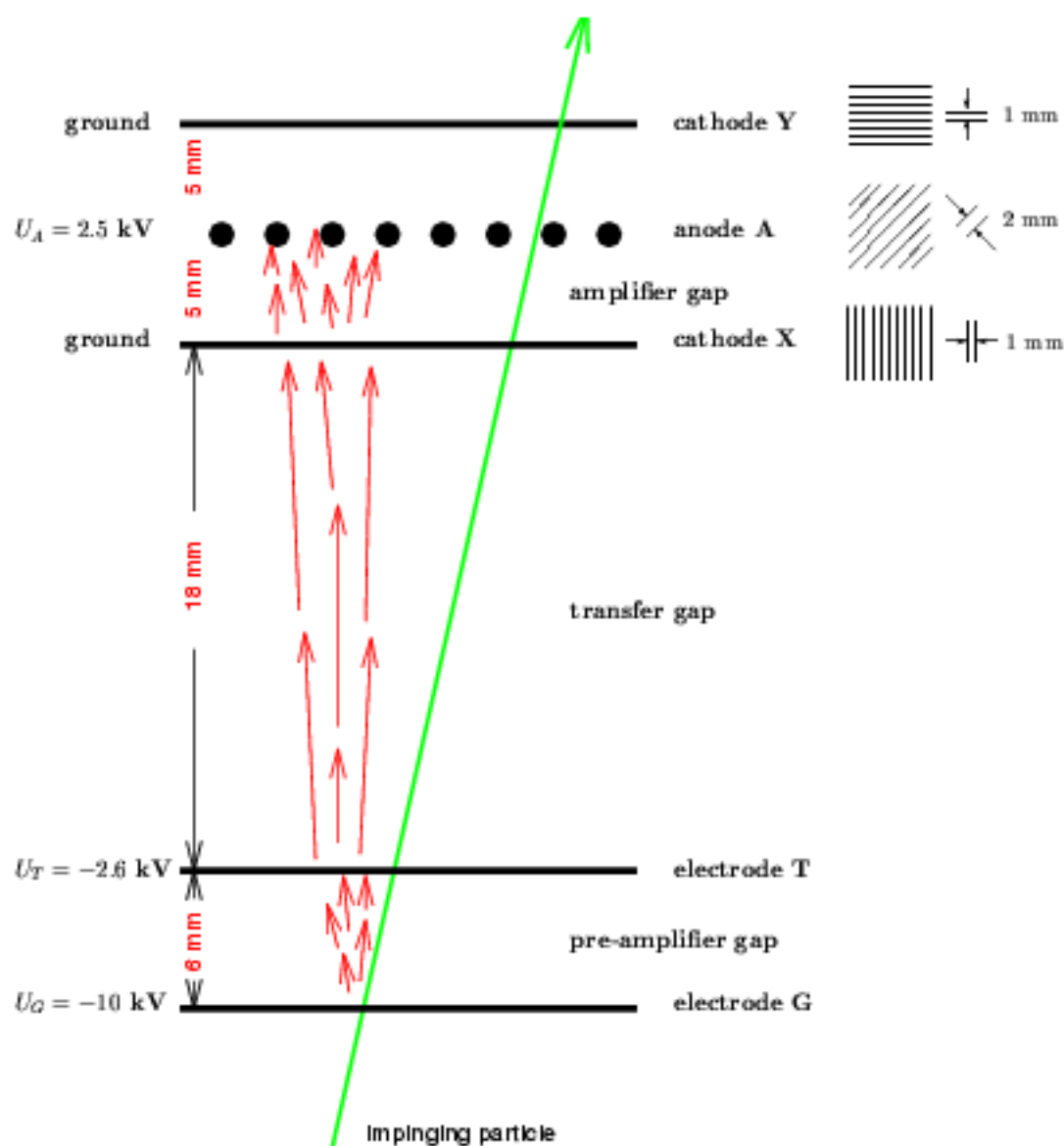


Figure 10: Two-stage MultiWire Proportional Chamber (MWPC) ZST developed for the detection of heavy ions at relativistic energies and for beam monitoring [Ste91]. Typical potentials applied to the planar electrodes are indicated.

These two plastic scintillators were used to veto on beam halos. HALO is a $10 \times 10 \text{ cm}^2$ square with a circular hole of 8 cm diameter in the center. It was placed at the entrance of CAVE B close to POS01. ROLU (“Rechts-Oben-Links-Unten” which means “right-up-left-down”) was placed about 10 meters behind HALO and about 1.7 meters in front of the target. It is composed of 4 plastic rectangles which can be moved along a frame through a motor in order to adjust the rectangular hole formed by them from 0×0 to about $4 \times 4 \text{ cm}^2$ [Ste96]. During most of our beam time, the hole from ROLU was set to about $3 \times 3 \text{ cm}^2$ which gave the limit of the beam size on the target position.

(4) PIN01 and PIN02

They are $5 \times 5 \text{ cm}^2$ silicon PIN diodes of 0.172 mm (40.1 mg/cm^2) thickness placed in the beam near the target. From the energy loss ΔE_1 , ΔE_2 of the particles, together with their velocity β_1 and β_2 (in front and behind of the target) deduced from time of flight ($t_1 - t_0$) between POS01 and the TOF-wall (or GFI01), the charge number Z_1 and Z_2 in front of and behind the target can be calculated (see chapter 4.1 for detail). The efficiency of PIN01 and PIN02 are nearly 100%.

(5) GFI01 and GFI02

GFI01 and GFI02 (“Großer Fiber” which means “big fiber”) are one-dimensional position sensitive large scintillating fiber detectors developed for experiments with relativistic heavy-ion beams [Cub98](see fig. 11). Each one has an active area of $50 \times 50 \text{ cm}^2$ and is composed of about 500 fibers with $1 \times 1 \text{ mm}^2$ square cross section. In order to identify which fiber is hit, one end of each fiber is coupled to a position-sensitive photomultiplier (PSPM) via a specially designed mask. The position resolution of the PSPM is good enough to distinguish individual fibers. For trigger purposes and to achieve good timing information, the other end of the 500 fibers are read out by a conventional photomultiplier.

The position resolution is determined by the fiber width of 1 mm. Depending on the nuclear charge of the beam, the efficiencies are between 80% and 100% and the time resolutions are between 800 and 200 ps FWHM. The counting rate can be up to 10^6 Hz .

In our experiment, GFI01 and GFI02 were placed behind ALADIN [ALA89] which bends the secondary beam particles after traversing the secondary target by 18.7° but the reaction products by different angles according to their different A/Z ratios and scattering angles. With the fibers along the vertical direction, GFI01 and GFI02 give the horizontal position information $G1X$ and $G2X$ which are used to determine A_2 and the scattering angle behind the target. GFI can also be used to measure time of flight (see chapter 4.1).

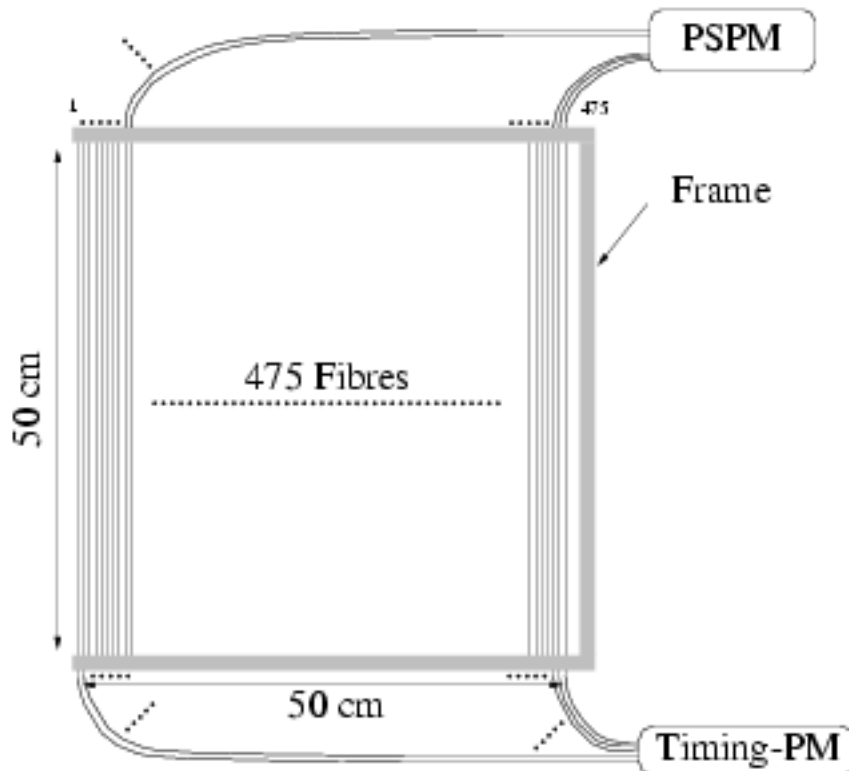


Figure 11: *One-dimensional position sensitive big scintillating fiber detector GFI developed for experiments with relativistic heavy-ion beams [Cub98].*

(6) TOF-wall

The TOF-wall was placed at the end of CAVE B which was about 25 meters away from POS01. It is a $0.5 \times 208 \times 200 \text{ cm}^3$ plastic wall composed of 20 scintillator strips each with an active area of $0.5 \times 10 \times 200 \text{ cm}^3$ and a black thin light shield. The strips are arranged parallel to each other and along the vertical direction. The time resolution of the TOF-wall is 200~300 ps FWHM. From the time of flight between POS01 and the TOF-wall, velocities for different isotopes can be clearly separated and the mass number A_1

before the target can be identified (see chapter 4.1). In addition, the TOF-wall can also give position information with a spatial resolution of 10 cm (horizontal) and 2–3 cm (vertical).

3.2.2 The γ -spectrometer Crystal Ball (CB)

The Darmstadt-Heidelberg Crystal Ball (CB) is a 4π γ -spectrometer developed and built by a collaboration between GSI, Darmstadt, Max-Planck-Institut für Physik, Heidelberg and Physikalisches Institut der Universität Heidelberg [Met86]. It consists of 162 individual NaI crystals (each of them is coated by a thin aluminium layer) forming a closed shell with 20 cm crystal thickness and an inner diameter of 50 cm. Four different shapes are used for the crystals, one regular pentagon (12) and three irregular hexagons (60+60+30). With an area of 49 cm² at the front face, all of them covers the same solid angle of 77 msr, thereby subtending an opening angle of 18° with respect to the center of the ball.

The CB is mounted on a compact platform of 2×4 m² size. The construction allows the CB to be adjusted to different beam heights and be opened perpendicular to the beam direction.

As measured during the commissioning in 1983, the total efficiency of the full ball is 96% at 1.3 MeV and 90% at 3.0 MeV. The full energy efficiency is 71% at 1.3 MeV and 56% at 3.0 MeV. The energy resolution of the NaI crystals is about 7 ~ 8% at 1.3 MeV and the mean time resolution is 3.5 ns.

The CB and its ancillary set-up in this ⁵⁰Ti experiment is shown in fig. 12. Several targets were mounted on an aluminium ladder. It was possible to change targets during the beam time by moving the target ladder up and down through a motor which was controlled by a PC. The target chamber with an outer diameter of 49 cm was made from 3-mm-thick carbon fiber laminate.

As discussed in chapter 3.1.3, the huge atomic background produced by the relativistic beam must be strongly suppressed. One method is to install additional material between the target and the NaIs to absorb X-rays and low-energy γ -rays from atomic processes in order to avoid pile up in the γ -detectors. For this purpose, a tube with a diameter of 10 cm and a length of 43 cm was placed in the carbon chamber along the beam line with the target inside. Two small openings were made on top and bottom of the absorber to let the target ladder move freely. The absorber was composed of an inner layer of 2 mm aluminium and an outer layer of 2 mm lead. The aluminium layer kept the shape of the tube and stopped electrons; while the lead layer absorbed X-rays and low energy γ -rays. Both of them did not absorb too many of the higher energy γ -rays which we were interested in. For example, for photons at 100 keV, the absorption of the lead layer is $\geq 99\%$; while for γ -rays at 500 keV, it is 30% and 40% with $\theta_\gamma = 90^\circ$ and 45° corresponding to an effective absorption thickness of

$\frac{2}{\sin\theta_\gamma} = 2$ and 2.8 mm respectively. The absorption of the aluminium layer is negligibly small.

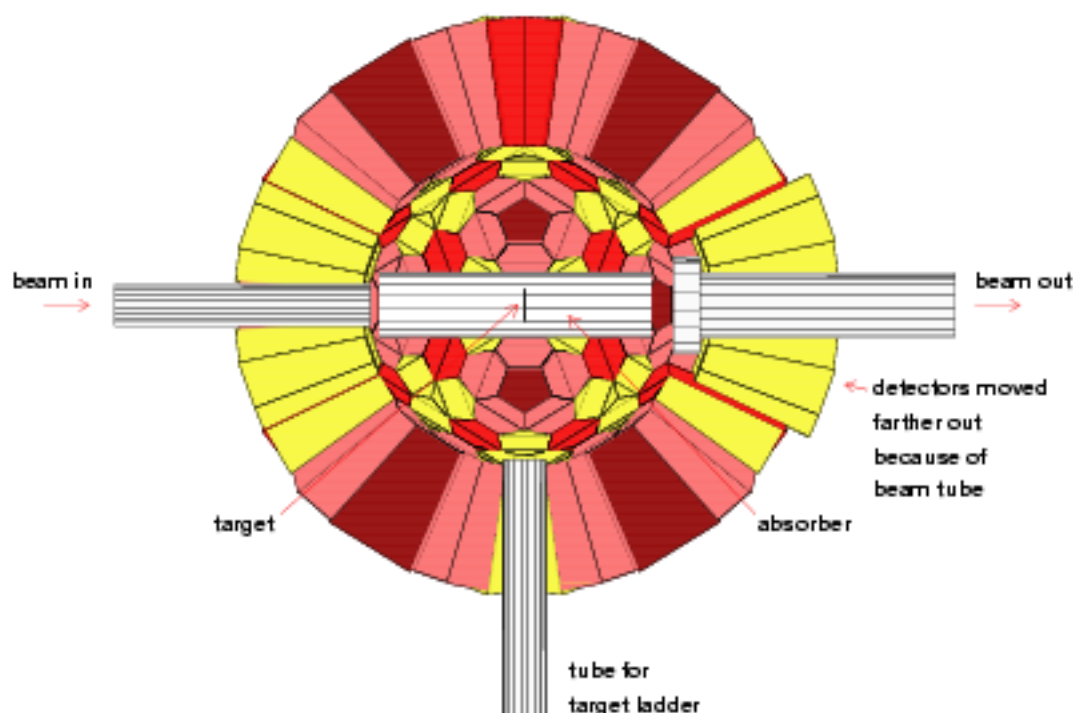


Figure 12: Half shell of the γ -spectrometer CB in the ^{50}Ti experiment, with absorber and target. The vacuum chamber is not shown for clarity.

Several crystals were removed for mechanical reasons. One crystal (82) was replaced by the beam-in tube, one (77) by the tube for the target ladder. For the beam-out tube, three crystals (81, 61 and 91) were removed from the ball and four crystals (60, 62, 90 and 92) were moved further out by 4 cm. In addition, three crystals (49, 127 and 162) did not work properly and one crystal (92) had considerable energy calibration change (see chapter 4.3.1) during the experiment.

The efficiency of the CB was reduced to $85 \pm 4\%$ (total) and $57 \pm 3\%$ (full energy) mainly

because of the missing NaIs and the lead absorber. For the energy and the mean time resolution of the NaIs, $8 \pm 2\%$ and 3.8 ns were derived respectively (see chapter 4.3 for detail).

3.2.3 The neutron detector LAND

A Large Area Neutron Detector LAND has been built to study neutrons from relativistic heavy-ion collisions at SIS [LAN92]. Fig. 13 shows the structure of LAND and one of its paddles. The full detector has a front face of $2 \times 2 \text{ m}^2$, 1 m depth and is composed of 10 layers with 20 paddles in each layer. The $200 \times 10 \times 10 \text{ cm}^3$ paddles are arranged parallel to each other in the same layer but orthogonal to each other in subsequent layers, thus giving position information in both vertical and horizontal directions. Each paddle has an alternating sandwich structure of 5mm scintillator/5mm passive iron converter in order to increase the detection efficiency. Particles produced by the interactions between the incoming neutrons and the iron converters ionize and excite the scintillator material. Light emitted from the scintillators of the whole paddle is detected by two photomultipliers on either end of the paddle. From the two photomultiplier signals, the position of the light production can be determined either by arriving time difference ($t_1 - t_2$) or by the logarithm of the pulse height ratio $\ln(E_1/E_2)$; while the time information can be deduced from the mean time $(t_1 + t_2)/2$.

In front of LAND, a veto detector for charged particles is installed. It consists of 20 scintillator strips of the same structure as in the TOF-wall. The strips are arranged parallel to each other and along the horizontal direction. Each strip covers an area of $200 \times 10 \text{ cm}^2$ which matches the neutron paddle size and a thickness of 0.5 cm which is enough for particles to have interaction within it but too thin for a noticeable neutron interaction. Again, the light is read out at both ends of each strip in order to obtain position and time information.

In the experiment, LAND was placed about 11 meters away from the target facing directly to the target. Although its opening angle was only 33 msr ($< 0.3\%$ of the full 4π solid angle), LAND can still be taken as a “ 4π ” detector because the neutrons emitted from the relativistic projectiles are strongly forward focused. For example, if a projectile goes along the beam line with a kinetic energy of 220 AMeV, all the emitted neutrons with kinetic energy less than 2 MeV in its rest system can be detected by LAND.

The detection efficiency of LAND (i.e. at least one neutron fires LAND) is about 85% if there is only one neutron emitted from a projectile with a kinetic energy of 220 MeV and more than 98% if there are more than one neutrons emitted in an event.

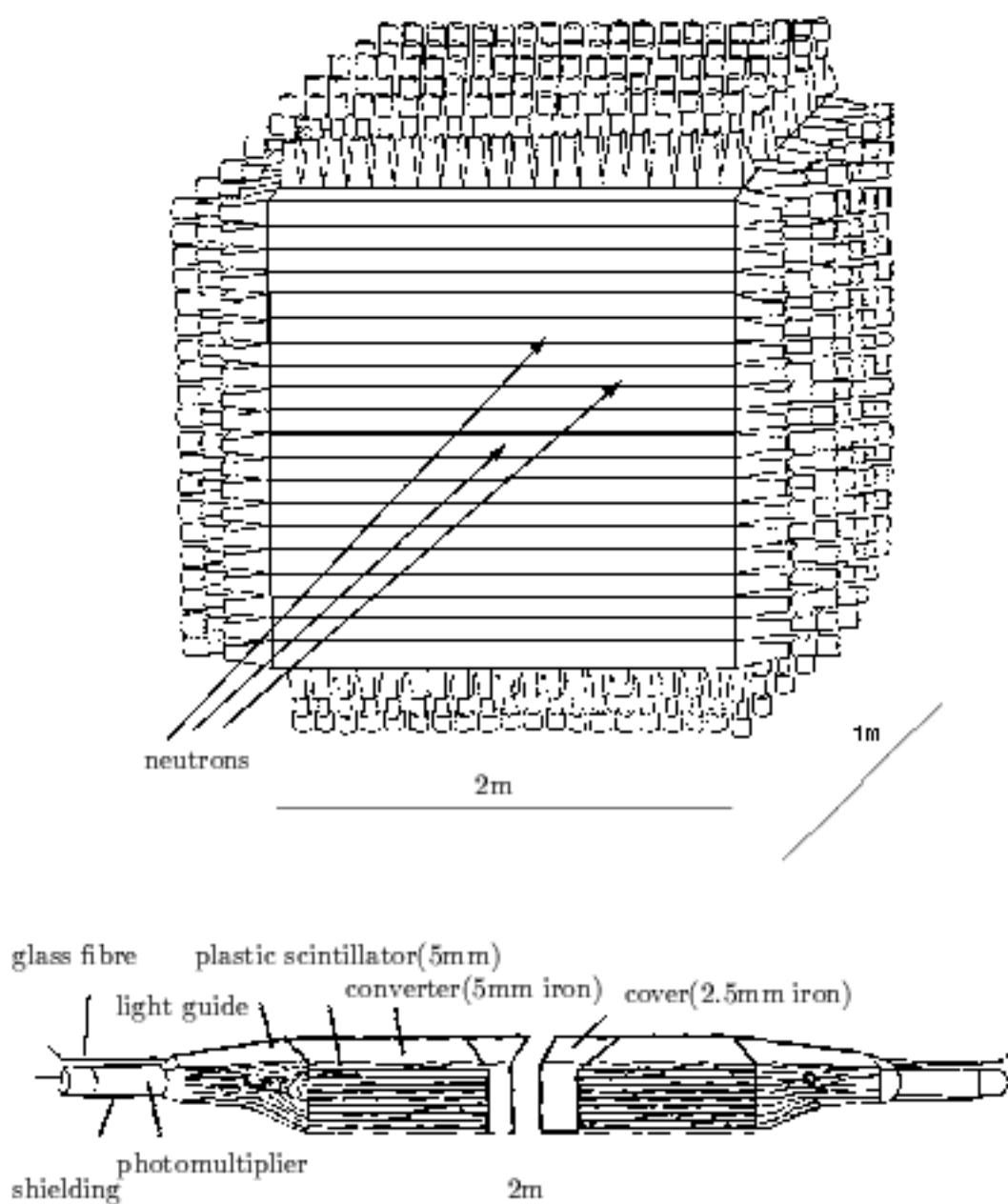


Figure 13: The neutron detector LAND (top) and one of its 200 paddles (bottom) [LAN92].

3.3 Electronics and triggers

3.3.1 The electronics of the Crystal Ball (CB)

The electronics of the CB in the ^{50}Ti experiment is shown in fig. 14. Each individual NaI of the CB gave one signal to a QDC from which we got the energy information. Another signal went to a CFD. In order to suppress atomic background produced from the beam (see chapter 3.1.3), the threshold of the CFDs was set to around 500 keV. Each CFD had two outputs. One of them fed in the "START" of a TDC. The second output from all the CFDs joined together into an "OR" gate to generate the "CB-OR" trigger. All the TDCs had a common "STOP". When there was no beam during the source measurement for the CB calibration, the "STOP" came from the same "OR" gate as the "CB-OR" trigger; when the beam was there, POS01 generated the common "STOP".

As described above, the "CB-OR" trigger required that at least one NaI was fired by a γ -ray with energy higher than 500 keV.

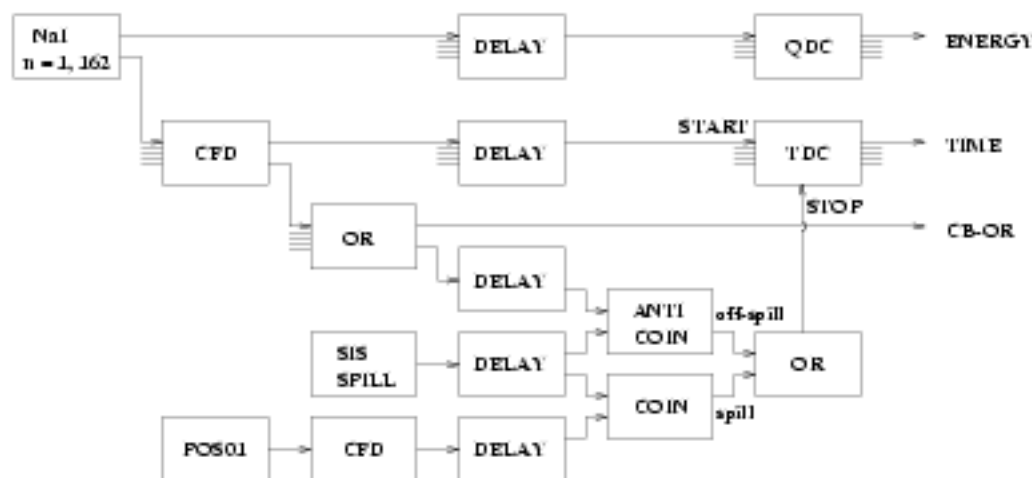


Figure 14: The CB front-end electronics in the ^{50}Ti experiment. The threshold of the CFDs was set to around 500 keV to suppress the atomic background produced by the beam. The "CB-OR" trigger was the "OR" of the signals from all CFDs.

3.3.2 Triggers

Sixteen different triggers were foreseen in the experiment. They were down-scaled by different factors ranging from $2^0 = 1$ to $2^9 = 512$. The master trigger for the data acquisition system was the “OR” of all these triggers after they were down-scaled (see fig. 15). The rate of the master trigger was about 170 Hz introducing $\sim 50\%$ dead time.

The main hardware triggers, which were later used in the analysis, were as follows:

$$(1) \text{ fragment} = \text{spill} \oplus \text{ZST01} \oplus \text{POS01} \oplus \overline{\text{HALO} + \text{ROLU}} \oplus \text{PIN02} \oplus \text{TOF-wall}$$

This trigger selected the “good” particles from the RIB. “Good” means that the particles came into CAVE B without firing the veto detectors HALO and ROLU (suitable beam size) but firing the particle detectors along the beam line from ZST01, POS01, PIN02 till the TOF-wall. The raw rate of this trigger was about 5500 Hz. During most of the beam time, this trigger was down-scaled by a factor of $2^9 = 512$; the accepted rate of this trigger was ~ 6 Hz. The product of the number of the events with this trigger and the down-scale factor were used as the number of projectiles to estimate cross sections.

$$(2) \gamma = \text{fragment} \oplus \text{CB-OR}$$

This trigger required at least one of the NaIs of the CB was fired coincident with a “good” particle in the RIB. The raw rate of this trigger was ~ 140 Hz. Without down-scaling during the beam time, the accepted rate of this trigger was ~ 65 Hz. The events from this trigger were used for in-beam γ -spectroscopy. Although a threshold of 500 keV was set to the CFDs of the NaIs of the CB and coincidence with the “good” particles was required, there were still a lot of events from atomic background in this trigger.

$$(3) \gamma + \text{neutron} = \text{fragment} \oplus \text{CB-OR} \oplus \text{LAND}$$

Coincidence of γ (’s) from the CB, neutron(’s) from LAND and a “good” particle in the RIB was required for this trigger. The raw rate of this trigger was about 12, 9 and 60 Hz respectively for the Pb target, no target and C target run. It was not down-scaled during the beam time. The events from this trigger were used for in-beam γ -spectroscopy related with giant resonances and/or nuclear reactions from which neutrons were emitted. The γ -spectra from this trigger were nearly free from atomic background.

$$(4) \text{ single } \gamma = \text{off-spill} \oplus \text{CB-OR}$$

At least one of the NaIs was fired with the condition that there was no beam. This trigger was used for calibration of the CB before and after the beam time. It was not down-scaled

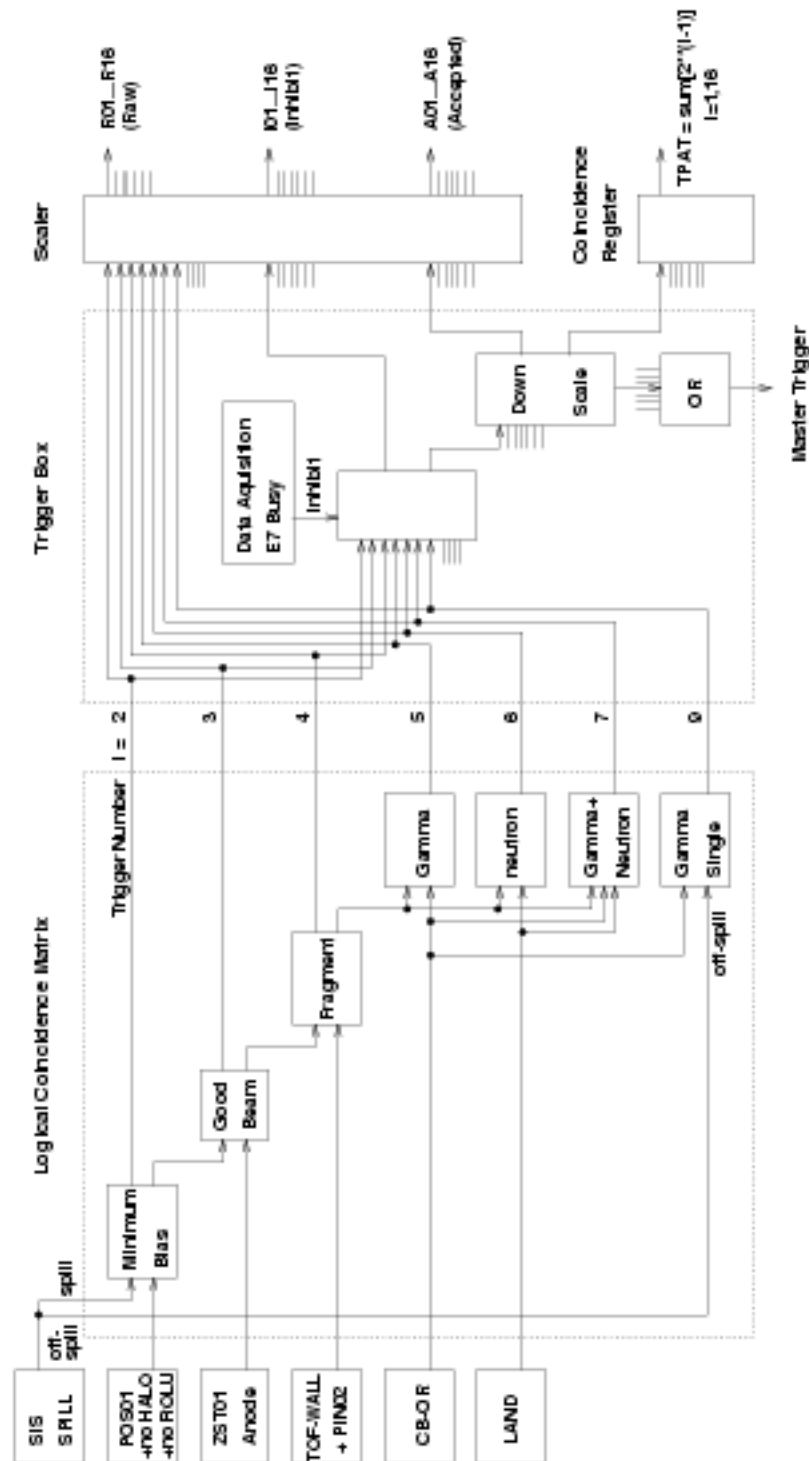


Figure 15: Triggers and scalers in the ^{50}Ti experiment. The master trigger for the data acquisition system was the “OR” of all the sixteen triggers after they were down-scaled.

during the calibration. During the beam time, however, it was down-scaled by a factor of $2^9 = 512$.

3.4 Statistics

The experiment was performed at GSI in 1995 by the CB-LAND-FRS collaboration. There was first a test measurement from July 28th to August 1st. Then we had the short production run from September 28th to October 4th which will be discussed in the following.

At the beginning of the beam time, much time was spent to focus the beam in order to achieve a reasonable transmission of 15-20% from FRS to CAVE B which is about 250 meters away (see also chapter 3.1.1). After that, without primary production target, the mono-energetic primary ^{50}Ti beam was used instead of the RIB to calibrate the particle detectors in CAVE B. In addition, there was a cosmic run to calibrate LAND.

Table 3: The statistics of RIB on target.

target	942 mg/cm ² Pb	no target	536 mg/cm ² C
beam time (hour)	28.8	8	6.4
beam particles	6.9×10^8	4.2×10^8	2.9×10^8
events on tape			
γ	2.9×10^6	1.5×10^6	2.1×10^6
$\gamma+n$	3.9×10^5	1.3×10^5	6.5×10^5

There were altogether 43 hours of RIB on target. Two targets were used: 942 mg/cm² Pb with a size of 4.99×4.96 cm² and 536 mg/cm² C with a size of 5.03×5.03 cm². The reaction rate for both targets was around 1%. The measurement with the Pb target lasted 28.8 hours with 2.9×10^6 γ events on tape and the measurement with the C target lasted 6.4 hours with 2.1×10^6 γ events on tape. In addition, there were 8 hours measurement with the RIB but without any target in order to measure the background originating from the surrounding material. The statistics of RIB on target is summarized in table 3. The intensity of the RIB measured at the entrance of CAVE B during the measurements with different targets is shown in fig. 16.

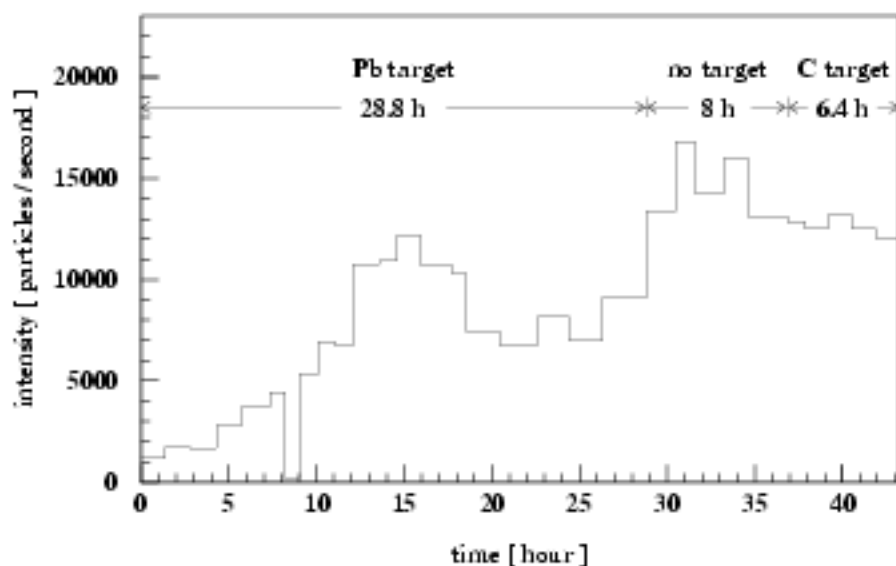


Figure 16: *The intensity of the RIB measured at the entrance of CAVE B during the measurements with different targets.*

The calibration of the CB was done both before and after the beam time by using three γ -sources ^{152}Eu , ^{88}Y and ^{226}Ra with γ energies ranging from 122 keV to 2204 keV.

4 Data analysis

The acquisition, analysis and control software for the experiment was PAW-LAND, which is based on the PAW(Physics Analysis Workstation)/ZEBRA [Cer93] software package developed at CERN but significantly extended for the experiments in CAVE B [Bla89, Lei93]. The programming language is FORTRAN 77. The experimental parameters such as calibration, geometry etc. are saved in a data base by the memory manager ZEBRA. The experimental data were written as LMD (list mode data) files to DLT (digital linear tape) tapes event by event. Each event includes the complete information from all the detectors. In order to analyse the data from the LMD files, one needs first to run PAW-LAND to create an N-Tuple [Cer95] including the necessary entries and then work with the N-Tuple. There are four levels of N-Tuples from which three were used in the analysis. The lowest level is the so called "raw-N-Tuple" with data like QDC- and TDC- channels, from which energy and time can be calibrated. After putting the calibration parameters to the data base, the "calibrated-N-Tuple" is available. Finally one can combine and operate the calibrated variables to get the "hit-N-Tuple" with physical quantities like multiplicity, time of flight, position, velocity, mass and charge number, etc. which can be directly used in the analysis.

This chapter consists of four parts dealing with: (1) particle identification, (2) scattering angle determination, (3) γ -data analysis and (4) cross section determination. The analysis of the neutron detector LAND is not included here and readers are referred to [Bor95].

4.1 Particle identification

As described in chapter 3.1.1, we had several tens of different nuclear species in the RIB simultaneously, which need to be identified event by event both before and after the reaction with the secondary target.

4.1.1 Charge identification and velocity of particles

When particles pass through matter, they lose energy mainly because of atomic collisions with electrons. The energy loss depends on the charge state of the particles q (in our case $q = Z$ as the energies were so high that the particles were completely stripped), their velocities β and the stopping matter:

$$\Delta E = Z^2 \cdot f(\beta), \quad (34)$$

where $f(\beta)$ is the function of β with parameters depending on the material and thickness of the stopping matter but not on the incident particles.

In order to determine Z_1 and Z_2 , the charge number in front of and behind the target, ΔE_1 and ΔE_2 were measured by the silicon-diodes PIN01 and PIN02. The procedure to deduce $f(\beta)$ and to calculate β_1 and β_2 will be described in the following.

The function $f(\beta)$ is complicated if derived theoretically (e.g. Bethe-Bloch formula [Leo94]). In the analysis, $f(\beta)$ was deduced by using the program ATIMA [Sch91] developed at GSI which calculates various physical quantities characterizing the slowing-down of protons and heavy ions in matter for kinetic energies ranging from 1 AkeV to 500 AGeV. Giving the stopping matter as 0.172 mm thick silicon (PIN01, PIN02) and the particles as ^{50}Ti ($q = Z = 22$), the energy loss ΔE for different velocities in the range of $\beta = 0.45 - 0.75$ could be calculated by running ATIMA. Fitting the results by a polynomial, we could get $f(\beta)$ [Hol96]:

$$f(\beta) = \sum_{i=1}^6 a_i \beta^{i-4}, \quad (35)$$

as shown in fig. 17.

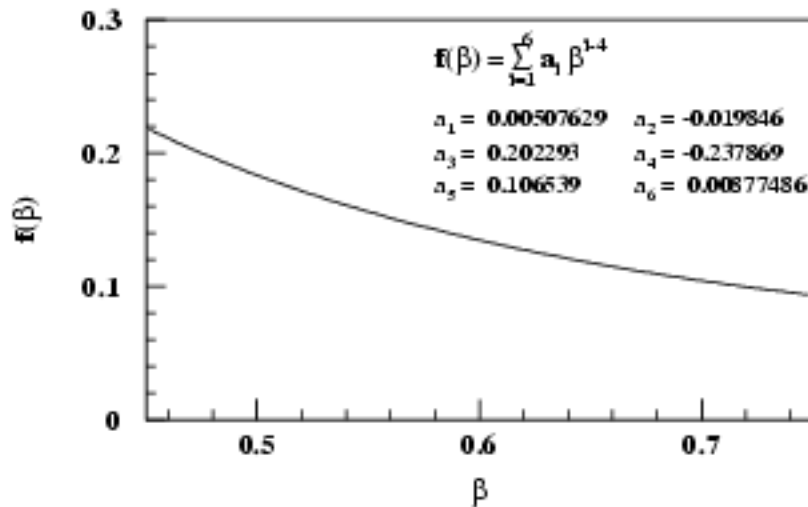


Figure 17: The polynomial $f(\beta)$ in the velocity region relevant to our experiment, deduced by fitting the data calculated from ATIMA for $^{50}\text{Ti}^{22+}$ on 0.172 mm silicon. It was used to calculate Z_1 and Z_2 from the energy loss in PIN01 and PIN02 (see formula (34)).

The ideal way to obtain β_1 and β_2 , the velocity of particles in front of and behind the target, would be to measure the time of flight in front of as well as behind the target, because the particles may change their velocities significantly when passing through the thick target. However, the time resolution of the detectors PIN01, PIN02, ZST02 and ZST03 near the target were not good enough for resolving different masses of the particles via the time of flight measurement. Therefore, we could only use the time of flight from POS01, which was at the entrance of CAVE B, to GFI01 (or the TOF-wall), which was far behind the target (see fig. 9 in chapter 3.2), to derive both β_1 and β_2 . This was done by an iterative calculation [Cub96] which will be described briefly in the following.

The primary value of β_1 was the average velocity between POS01 and GFI01. Using this β_1 value and the energy loss in PIN01, the primary value of Z_1 could be calculated from formula (34). Under the simplifying assumption that the particles only lose energy at the target position considering an “effective” thickness ΔX , which was the sum of the thickness of the target (942 and 536 mg/cm² for the Pb and C target respectively) and all the other material (407 mg/cm²) between POS01 and GFI01 (both including), exists, we calculated the energy loss $\Delta E \propto Z_1^2 \beta_1^{-3/2} \Delta X$ and then the velocity change $\Delta\beta$ in the target. After that, a more accurate β_1 could be obtained by solving the following equation:

$$t_{GFI01} - t_{POS01} = \frac{s_1}{c\beta_1} + \frac{s_2}{c(\beta_1 - \Delta\beta)}, \quad (36)$$

where $(t_{GFI01} - t_{POS01})$ is the time of flight from POS01 to GFI01; $s_1 = 1175$ cm is the distance between POS01 and the target; $s_2 = 726$ cm is the distance between the target and GFI01.

Starting with the new β_1 value and iterating the whole calculation, an even better β_1 could be achieved. From the second iteration on, the β_1 value is stable within 10^{-5} . Finally, β_2 was calculated simply by $\beta_2 = \beta_1 - \Delta\beta$.

Using formula (34) with the β_1 and β_2 values derived from the iteration calculation, Z_1 and Z_2 values were finally obtained.

The main contribution to the resolution of β_1 and β_2 is from the time resolution of POS01 and GFI01:

$$\frac{\delta\beta_i}{\beta_i} = \frac{\sqrt{\delta t_{POS01}^2 + \delta t_{GFI01}^2}}{t_{GFI01} - t_{POS01}} \quad (i = 1, 2).$$

With $\delta t_{POS01} \sim 100$ ps, $\delta t_{GFI01} \sim 700$ ps and $(t_{GFI01} - t_{POS01}) \approx 106$ ns, 0.7% is derived as the resolution of β_1 and β_2 .

The resolution of Z_1 and Z_2 comes mainly from the energy resolution of PIN01 and PIN02 which is sufficient to distinguish different charges (see fig. 19 and fig. 20 in chapter 4.1.3).

4.1.2 Mass identification and resolution estimate

The mass of a charged particle behind a magnet can be evaluated from the following relation:

$$B\rho [Tm] = \frac{p}{qe} \equiv 3.107 \cdot \frac{A}{q} \gamma \beta, \quad (37)$$

where $B\rho$ is the magnetic rigidity; p is the momentum; q is the charge state, in our case $q = Z$ because the particles were fully ionized; e is the electron charge; A is the mass number; β is the velocity; $\gamma = 1/\sqrt{1 - \beta^2}$. The constant "3.107" is deduced as follows:

$$\begin{aligned} \frac{p}{qe} &= \frac{AM_u \gamma \cdot \beta c}{qe} = \frac{M_u c^2}{ec} \cdot \frac{A}{q} \gamma \beta = \frac{931.5 MeV}{e \times 2.9979 \times 10^8 m/s} \cdot \frac{A}{q} \gamma \beta \\ &= 3.107 \cdot \frac{A}{q} \gamma \beta \quad (\text{in } \frac{V}{m/s} \text{ i.e. } Tm). \end{aligned}$$

The isotopes in the RIB were selected by the FRS with $B\rho = 5.588$ Tm. The calculation of Z_1 and β_1 in front of the target is described in chapter 4.1.1. Therefore, the mass number A_1 in front of the target can be calculated by:

$$A_1 = \frac{5.588 \cdot \text{rint}(Z_1)}{3.107 \cdot \gamma_1 \beta_1}. \quad (38)$$

Here $\text{rint}(Z_1)$ means the integer nearest to Z_1 which is calculated with formula (34). The A_1 resolution is deduced as follows:

$$\begin{aligned} \frac{\delta A_1}{A_1} &= \sqrt{\left(\frac{\delta(B\rho)}{B\rho}\right)^2 + \left(\frac{\delta(\gamma_1 \beta_1)}{\gamma_1 \beta_1}\right)^2}, \\ \gamma_1 \beta_1 &= \frac{\beta_1}{\sqrt{1 - \beta_1^2}} \Rightarrow \frac{\delta(\gamma_1 \beta_1)}{\gamma_1 \beta_1} = \frac{1}{1 - \beta_1^2} \left(\frac{\delta \beta_1}{\beta_1}\right). \end{aligned}$$

With the acceptance of the magnets from FRS as $\delta(B\rho)/B\rho \sim 0.5\%$, $\delta\beta_1/\beta_1 \sim 0.7\%$ and $\beta_1 \sim 0.6$, $\delta A_1/A_1$ is obtained as 1.2%.

After the reaction with the secondary target, $\Delta p/p$ increased because of the energy straggling and, more important, A and/or Z changes. That means, when particles passed through the big bending magnet ALADIN behind the target, they were deflected horizontally (X-direction) along different paths due to different $B\rho$ values. Therefore, two one-dimensional position detectors GF101 and GF102 were used to determine $B\rho$ and thus to identify A_2 , the

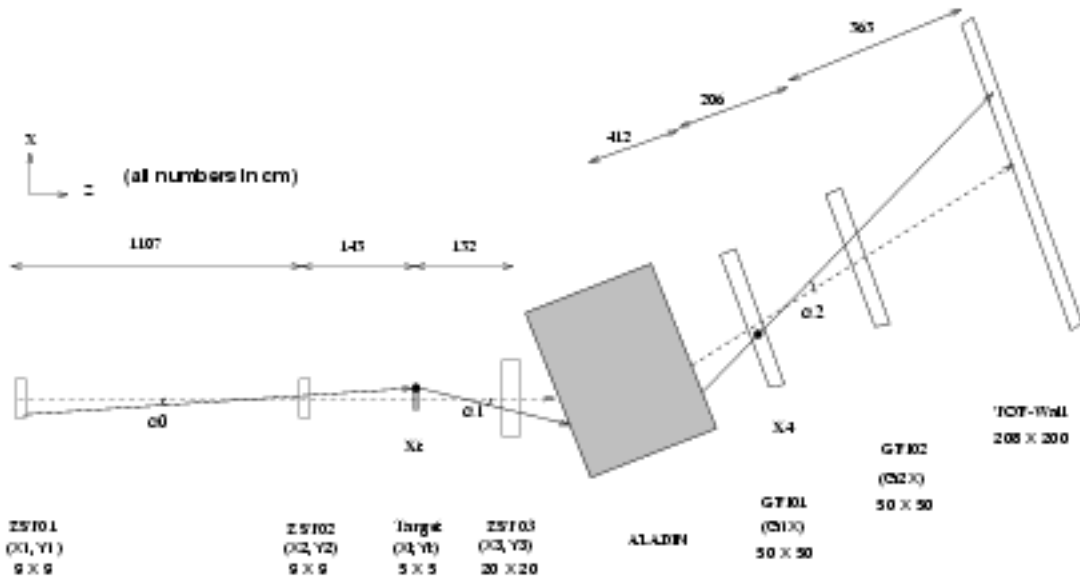


Figure 18: The illustration of the definitions of X_t , α_1 , X_4 and α_2 which are used in formula (39) to calculate $B\rho$ for the A_2 identification. The dashed line indicates the “standard trajectory” which is symmetric to the bending magnet ALADIN.

mass number after the target, by using the relation given in formula (37).

Before discussing how $B\rho$ was determined, we need to make the following definitions (refer to fig. 18) with the position unit in *cm*, the angle unit in *radian* and the magnetic rigidity unit in *Tm*:

- X_t : the horizontal position at the target;
- α_1 : the horizontal incoming angle in front of ALADIN;
- “standard trajectory”: a fixed horizontal trace which is symmetric to ALADIN with $\alpha_1 = 0$, $X_t = 0$ and deflection from the Z-axis of 14.4° (the angle between the axis of the ALADIN magnet and the Z-axis is 7.2°);
- $(B\rho)_0$: the magnetic rigidity associated with the “standard trajectory”;
- $\Delta(B\rho)$: the deviation of the magnetic rigidity from $(B\rho)_0$;
- X_4 : the horizontal position in GFI01 relative to the “standard trajectory”;

- α_2 : the horizontal outgoing angle behind ALADIN relative to the “standard trajectory”.

In order to determine X_t , position information from ZST01 and ZST02 is needed; for α_1 , ZST01, ZST02 and ZST03 are needed; for X_4 , GF01 is needed; for α_2 , GFI01 and GFI02 are needed (refer to appendix B for the detailed calculations). If any three of these four quantities are known, $\Delta(B\rho)/(B\rho)_0$ can be calculated from the following relation [Liv69]:

$$\begin{cases} X_4 = a_1 X_t + b_1 \alpha_1 + c_1 [\Delta(B\rho)/(B\rho)_0] \\ \alpha_2 = a_2 X_t + b_2 \alpha_1 + c_2 [\Delta(B\rho)/(B\rho)_0] \end{cases} \quad (39)$$

with parameters determined by the ALADIN geometry. If X_3 from ZST03, i.e. α_1 is available, $\Delta(B\rho)/(B\rho)_0$ is simply calculated as:

$$\frac{\Delta(B\rho)}{(B\rho)_0} = \frac{1}{c_2} (-a_2 X_t - b_2 \alpha_1 + \alpha_2), \quad (40)$$

with a resolution of 1.07%. If X_3 is missing and α_1 is not available, both relations in formula (39) need to be involved in order to derive $\Delta(B\rho)/(B\rho)_0$:

$$\begin{aligned} \frac{\Delta(B\rho)}{(B\rho)_0} &= \frac{1}{a_3} (-b_3 X_t + b_2 X_4 - b_1 \alpha_2), \\ a_3 &= b_2 c_1 - b_1 c_2, \\ b_3 &= b_2 a_1 - b_1 a_2, \end{aligned} \quad (41)$$

with a resolution of 0.72%. Because α_1 , which has a rather bad resolution ($\delta\alpha_1 \approx 4\delta\alpha_2$, see appendix B) is not involved here, the resolution of $\Delta(B\rho)/(B\rho)_0$ is expected to be better than that obtained by the former method.

Then we can obtain $B\rho$ and estimate its resolution:

$$B\rho = (B\rho)_0 \left[1 + \frac{\Delta(B\rho)}{(B\rho)_0} \right], \quad \frac{\delta(B\rho)}{B\rho} \approx \frac{\delta(B\rho)}{(B\rho)_0} = \delta \left(\frac{\Delta(B\rho)}{(B\rho)_0} \right).$$

Finally, A_2 can be calculated using a relation similar to formula (38). Similar to $\gamma_1\beta_1$, the resolution of $\gamma_2\beta_2$ is obtained as $\sim 1.09\%$. The resolution of A_2 is therefore estimated as:

$$\frac{\delta A_2}{A_2} = \sqrt{\left(\frac{\delta(B\rho)}{B\rho} \right)^2 + \left(\frac{\delta(\gamma_2\beta_2)}{\gamma_2\beta_2} \right)^2}.$$

For $\delta(\Delta(B\rho)/(B\rho)_0) = 1.07\%$ and 0.72% , $\delta A_2/A_2 = 1.5\%$ and 1.3% are obtained.

As discussed above, if information from all the tracking detectors is available and formula (40) is employed to calculate $B\rho$, A_2 is expected to be derived with a resolution of $\delta A_2/A_2 = 1.5\%$; if X_3 from ZST03 is missing and formula (41) is used to obtain $B\rho$, $\delta A_2/A_2 = 1.3\%$ is expected.

4.1.3 Charge and mass distribution in front of and behind the target

By applying the calculations discussed in the former two sections together, the charge and mass distribution in front of and behind the target is obtained [Cub96, Hol96]. This will be used later to set proper cuts in order to select different reaction channels which we are interested in.

After the fragmentation of the 330 AMeV ^{50}Ti primary beam on a $4\text{ g/cm}^2\ ^9\text{Be}$ primary target and the selection of FRS which was optimized to ^{38}S , the charge and mass distribution of the radioactive ion beams in front of the target is shown in fig. 19. About 60 nuclear species (of which more than 45 are neutron-rich) are clearly separated. The spectrum on the top-left shows the Z_1 distribution. The constant resolution of $\delta Z_1 \approx 0.5$ is sufficient to distinguish different elements. The two spectra on the bottom-right show the A_1 distribution of Mg ($Z_1 = 12$) and Ar ($Z_1 = 18$). A resolution of $\delta A_1 \approx 0.3$ and $\delta A_1 \approx 0.5$ for Mg and Ar isotopes is determined from the spectra. The A_1 resolution δA_1 is better for lighter isotopes because $\delta A_1/A_1$ is constant (see chapter 4.1.2). Even for the heavier isotopes, the A_1 resolution is sufficient. The efficiency to determine Z_1 and A_1 is $\sim 100\%$ and $\sim 80\%$, respectively.

As an example, fig. 20 shows the charge and mass distribution behind the Pb (left) and C (right) target requiring ^{28}Mg entering the target. The spectra in the top panel show the Z_2 distribution in which different elements are well separated with a resolution of $\delta Z_2 \approx 0.5$ and an efficiency to derive Z_2 is nearly 100%. The distribution at $Z_2 < Z_1 = 12$ behind the C target is much enhanced compared with the Pb target because nuclear reactions were dominant in the C target while in the Pb target there were strong atomic processes and Coulomb excitation in addition. The spectra in the middle and bottom panels show the A_2 distribution requiring $Z_2 = 12$, with A_2 derived by two methods which will be discussed in the following.

If X_3 from ZST03 was available and formula (40) was used, A_2 could be derived with a resolution of ~ 0.6 mass units for light nuclei like Mg (fig. 20: middle) and ~ 0.8 mass units for heavy nuclei like Ar. This is comparable to (about 20% larger than) the estimate given in the former section. The efficiency to determine A_2 with this method decreases dramatically as Z gets smaller (see table 4), e.g. to $\sim 30\%$ for Ar and $\sim 10\%$ for Mg. This is because, as mentioned in chapter 3.2.1, the efficiency of ZST02 was $\sim 50\%$ (e.g. 63% for Mg and 49% for Ar) and the efficiency of ZST03 was especially low for light isotopes (e.g. 19% for Mg and 77% for Ar).

When high efficiency was required in the analysis, e.g. to investigate γ -spectra cutting on A_2 , A_2 for light nuclei was calculated by formula (41) without X_3 in case ZST03 was not firing. In this way, the efficiency to determine A_2 for Mg could be up to $\sim 55\%$ but the resolution was reduced to ~ 0.8 mass units (fig. 20: bottom), which was about twice as large as the estimate given in the former section. The reason could be: the parameters used in

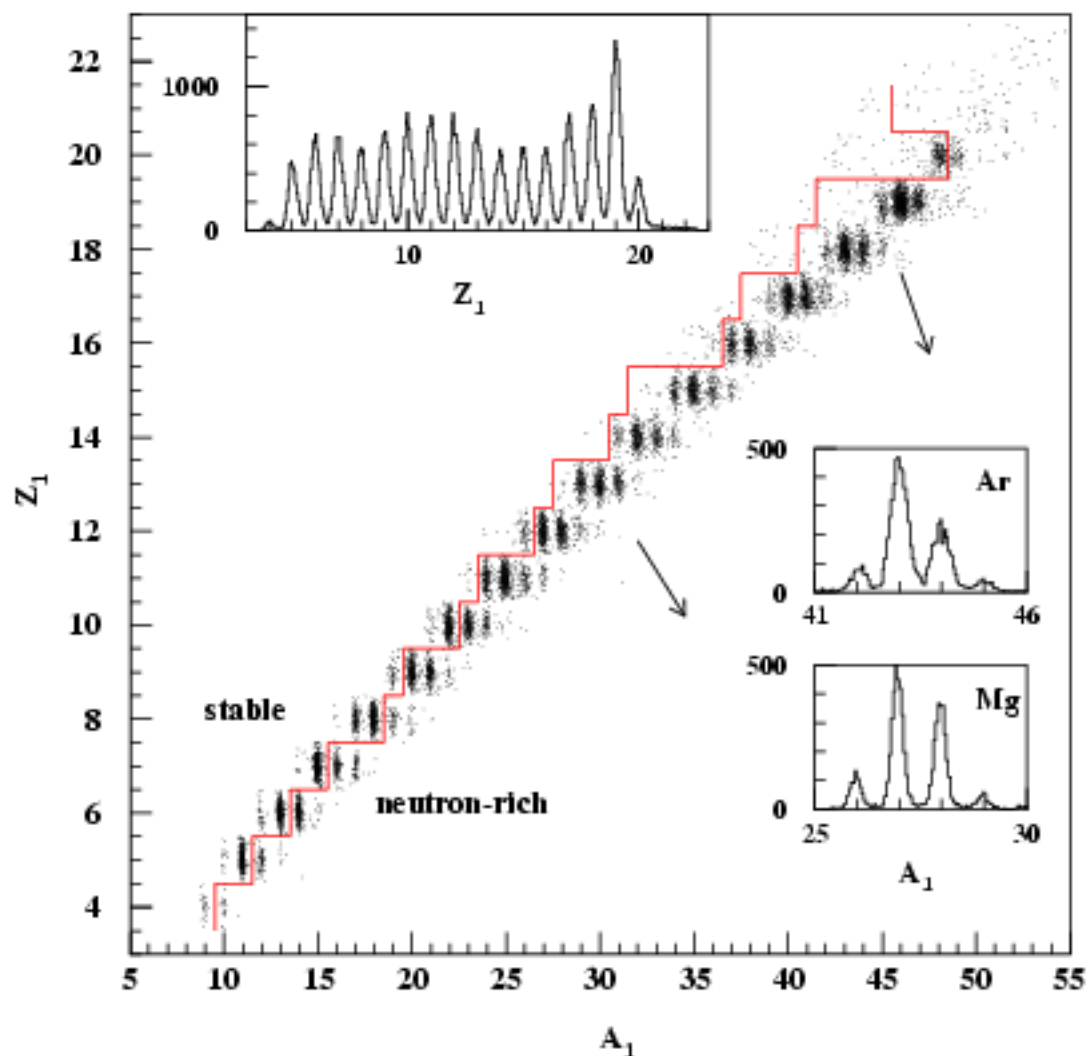


Figure 19: The charge and mass distribution of the RIBs produced from the fragmentation of the 330 A MeV ^{50}Ti primary beam on a 4 g/cm^2 ^9Be primary target with FRS setting optimized to ^{38}S . The borderline between stable and neutron-rich nuclei is marked. On the top-left the Z_1 distribution is shown; on the bottom-right, as examples, the A_1 distributions of Mg and Ar are shown.

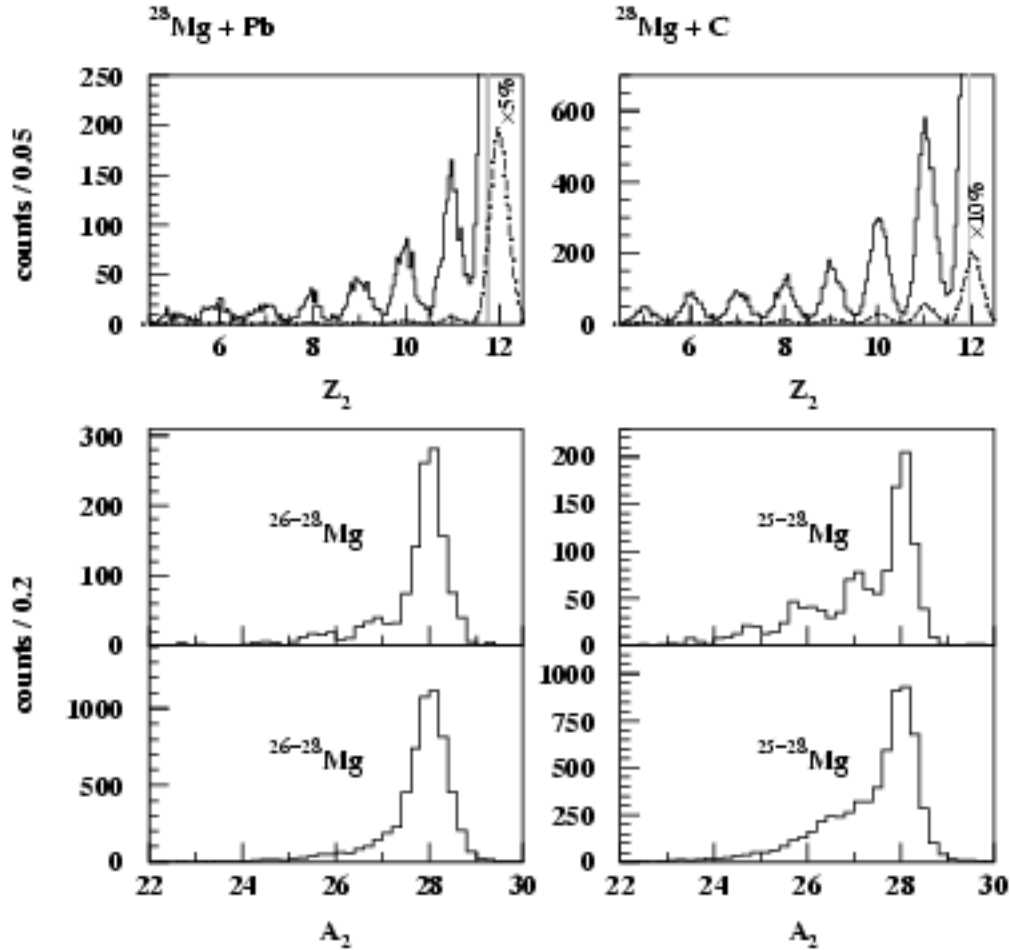


Figure 20: The charge and mass distribution behind the Pb (left) and C (right) target requiring incoming ^{28}Mg . The top panels show the Z_2 charge distributions. The middle and bottom panels display the A_2 mass distributions requiring $Z_2 = 12$. By requiring X_3 from ZST03, A_2 is determined with a resolution of ~ 0.6 mass units (FWHM) and an efficiency of $\sim 10\%$ (middle); if X_3 is not necessarily required, A_2 is determined with a resolution of ~ 0.8 and an efficiency of $\sim 55\%$ (bottom). There is contribution from atomic background in the $Z_2 = Z_1$ and $A_2 = A_1$ peak because no condition on the CB is required.

Table 4: The efficiency to determine A_2 if ZST03 is required.

element	Z	ε_{A_2}
Ar	18	32%
Cl	17	31%
S	16	28%
P	15	27%
Si	14	23%
Al	13	18%
Mg	12	10%
Na	11	6%
Ne	10	3%

formula (39) are obtained under simplifying assumption (e.g. the magnetic field of ALADIN is homogeneous along the X-axis and has a sharp cut-off along the Z-axis). If X_3 from ZST03 is available, only three parameters a_2 , b_2 and c_2 are involved; if X_3 is not available, all the six parameters a_i , b_i and c_i ($i = 1, 2$) especially $a_3 = b_2c_1 - b_1c_2$ are involved which may cause a larger systematic error.

In order to improve the A_2 quality, using detectors with both high resolution and high efficiency to measure X_1 , X_2 and X_3 is important. If the resolution of these quantities could reach 0.1 cm (instead of $\delta X_1 = \delta X_2 = 0.15$ cm and $\delta X_3 = 0.3$ cm in our experiment), $\delta A_2/A_2 = 1.2\%$ could be achieved. This would be as good as $\delta A_1/A_1$ which was sufficient.

4.2 Scattering angle

The main purpose to measure the scattering angle θ was to suppress the huge atomic background and to try to distinguish Coulomb excitation from nuclear excitation. In this section, the two methods to determine θ and the corresponding resolutions, the scattering angle acceptance, and the cut on θ to select Coulomb excitation, will be discussed.

4.2.1 Scattering angle determination and resolution

In order to make the calculations easier to be understood, readers are referred to fig. 18 in chapter 4.1.2. The angle unit will be *radian*, the length unit will be *cm*.

The following angles will be used in the calculations:

- θ_X : the horizontal scattering angle, i.e. the projection of θ on the X-Z plane;
- θ_X^{in} : the horizontal incoming angle before the target;
- θ_X^{out} : the horizontal outgoing angle after the target, same as α_1 in fig. 18;
- θ_Y : the vertical scattering angle, i.e. the projection of θ on the Y-Z plane;
- θ_Y^{in} : the vertical incoming angle before the target;
- θ_Y^{out} : the vertical outgoing angle after the target.

From ZST01 and ZST02, $(\theta_X^{in}, \theta_Y^{in})$ was calculated with a resolution of $\delta\theta_X^{in} = \delta\theta_Y^{in} = 0.19$ mrad. The position at the target (X_t, Y_t) , which is needed to determine $(\theta_X^{out}, \theta_Y^{out})$, was also calculated from ZST01 and ZST02. If (X_3, Y_3) from ZST03 was available, $(\theta_X^{out}, \theta_Y^{out})$ can be directly obtained with a resolution of $\delta\theta_X^{out} = \delta\theta_Y^{out} = 2.6$ mrad. Otherwise θ_Y^{out} was calculated from the TOF-wall with $\delta\theta_Y^{out} = 2.3$ mrad; and θ_X^{out} , which is actually α_1 in chapter 4.1.2, could be derived from GFI01 and GFI02 by using the relation in formula (39) with a resolution of $\delta\theta_X^{out} = 1.3$ mrad. See appendix C for the detailed calculations.

Because θ was small, it could be calculated approximately:

$$\theta \approx \sqrt{\theta_X^2 + \theta_Y^2} = \sqrt{(\theta_X^{out} - \theta_X^{in})^2 + (\theta_Y^{out} - \theta_Y^{in})^2}.$$

As $\delta\theta_X^{in}$ and $\delta\theta_Y^{in}$ were about one magnitude smaller than $\delta\theta_X^{out}$ and $\delta\theta_Y^{out}$, the resolution of θ was:

$$\delta\theta = \sqrt{(\delta\theta_X^{out})^2 + (\delta\theta_Y^{out})^2}.$$

To determine the scattering angle θ , information from ZST01 and ZST02 is necessary. If information from ZST03 was available, θ is expected to be obtained with a resolution of 4 mrad; if (X_3, Y_3) was missing and information from GFI01, GFI02 and the TOF-wall was used instead, $\delta\theta$ is expected to be 3 mrad. The reasons that the resolution with the latter method is expected to be better are: (1) in the X direction, GFI01 and GFI02 had better resolution than ZST03; (2) in the Y direction, although the TOF-wall had a limited resolution, the distance from the target to the TOF-wall was much larger than to ZST03. On the other hand, because formula (39), which was obtained under simplification of the

magnetic field of ALADIN, is involved in the latter method, the systematic error might be larger.

From the measurement without target, the resolution of θ was determined for both methods to be ~ 5 mrad. The efficiency of θ was measured as $\sim 10\%$ for Mg and $\sim 30\%$ for Ar if θ is determined from ZST01, ZST02 and ZST03; if GFI01, GFI02 and the TOF-wall are employed instead of ZST03, the efficiency to determine θ is $\sim 30\%$ for both Mg and Ar. For heavy nuclei like Ar, the former method was employed to determine θ ; for light nuclei like Mg, the latter method was used because of its higher efficiency.

4.2.2 Scattering angle acceptance

The scattering angle acceptance, i.e. the maximum scattering angle which can be measured by the detection system after the reaction with the secondary target, depended mainly on PIN02 because of its limited size (refer to fig. 18 in chapter 4.1.2). From its 5×5 cm² size and 80 cm distance to the target, the maximum angle which can be accepted by PIN02 was calculated as $\theta \approx 30$ mrad.

As illustrated in fig. 4 in chapter 2.2, the probability for both Coulomb and nuclear excitation drops sharply at $1.4^\circ = 24$ mrad. As to atomic angular straggling, according to the ATIMA simulation which is briefly introduced in chapter 4.1.1, the standard deviation of the angle width $\sigma(\theta_{strag})$ is 5.5 mrad for ³⁸S in the Pb target and respectively 1.7 and 1.8 mrad for ²⁸Mg and ⁴³Ar in the C target. Therefore, the ~ 30 mrad scattering angle acceptance was sufficient to cope not only with atomic straggling but also with the excitations caused either by the Coulomb force or by nuclear interaction.

However, the maximal scattering angle with fragmentation reactions is larger and it is necessary to check the acceptance of PIN02 in this case. This will be discussed in the following.

For the beam particles traversing the target, the main contribution to the scattering is atomic angular straggling which is small as mentioned above. For fragments, on the other hand, in addition to atomic straggling, fragmentation also contributes to the scattering with an angle width on the x and y direction (the beam is along the z direction) as:

$$\sigma_i(\theta_{frag}) = \frac{\sigma(p_i)}{p_{tot}} = \frac{\sigma(p_x)}{p_{tot}} \quad (i = x, y), \quad (42)$$

where p_{tot} is the total momentum which is proportional to A_1 :

$$p_{tot} = A_1 \beta \gamma \times 931.5 \quad (MeV/c),$$

and $\sigma(p_z)$ is the longitudinal-momentum width which is proportional to $\sqrt{|\Delta A|}$ according to an empirical relation [Mor89]:

$$\sigma(p_z) = \frac{150}{\sqrt{3}} \sqrt{|\Delta A|} \quad (MeV/c).$$

Using formula (42), the fragmentation angle width $\sigma_i(\theta_{frag})$ ($i = x, y$) is calculated as $4.4\sqrt{|\Delta A|}$ and $3.0\sqrt{|\Delta A|}$ mrad for the incoming ^{28}Mg and ^{43}Ar particles respectively.

For the fragmentation of ^{28}Mg and ^{43}Ar with the C target, the relative acceptance of PIN02, which is normalized to 1 for beam particles, is therefore deduced as follows:

- [1] events with the beam trigger from the measurement of RIBs on the C target are used;
- [2] two-dimensional positions (X, Y) on PIN02 are calculated from (X_n, Y_n) ($n=1, 2$ and 3) which are measured by the trajectory detectors ZST01, ZST02 and ZST03, respectively; with the condition of $|X| < 2.5$ cm and $|Y| < 2.5$ cm, N_0 , the number of events which are only affected by atomic straggling in the C target and are within the PIN02 acceptance of 5×5 cm², is obtained (see fig. 21: left);
- [3] smearing (X, Y) to (X_{frag}, Y_{frag}) on PIN02 by assuming fragmentation with an angle width of $\sigma_i(\theta_{frag}(|\Delta A|))$ ($i = x, y$) calculated from formula (42) and then requiring $|X_{frag}| < 2.5$ cm and $|Y_{frag}| < 2.5$ cm, $N(\Delta A)$, the number of events which are affected by atomic straggling as well as by fragmentation with the C target and are within the PIN02 acceptance, is obtained (see fig. 21: right);
- [4] the ratio $N(\Delta A)/N_0$ is just the relative acceptance of PIN02 for the fragments with mass loss ΔA .

As listed in table 5, even for the fragments with mass loss $\Delta A = -10$, the relative acceptance of PIN02 is larger than 80%. For the fragmentation with the Pb target, similar results should be obtained because the fragmentation angle width is empirically independent of the target.

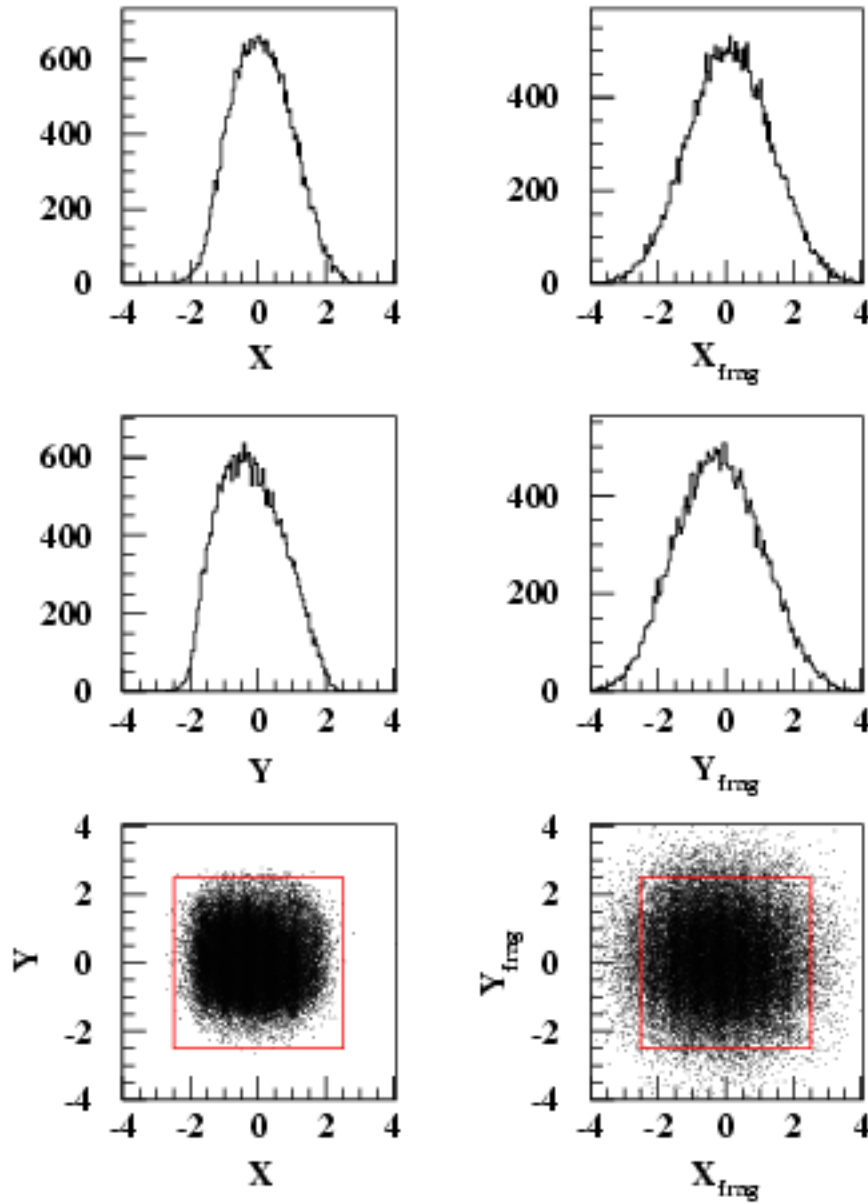


Figure 21: left: Positions (X, Y) on PIN02 of the beam particles from the measurement of ^{28}Mg on the C target, only atomic straggling is included. right: Positions $(X_{\text{frag}}, Y_{\text{frag}})$ on PIN02 smeared from (X, Y) by assuming fragmentation on the C target with, e.g., a mass loss of $\Delta A = -6$ i.e. an angle width of $\sigma_x(\theta_{\text{frag}}) = \sigma_y(\theta_{\text{frag}}) = 11$ mrad, straggling and fragmentation are included. The size of PIN02 is marked.

Table 5: The relative acceptance of PIN02 for fragments with mass loss ΔA from two reactions. The values can be fitted with a second order polynomial.

$^{28}\text{Mg}+\text{C}$ @ 238.7 AMeV		$^{43}\text{Ar}+\text{C}$ @ 222.2 AMeV	
ΔA	ϵ_{PIN2}	ΔA	ϵ_{PIN2}
0	1.000	0	1.000
-1	0.991	-1	0.997
-2	0.976	-2	0.992
-3	0.957	-3	0.987
-4	0.943	-4	0.981
-6	0.908	-6	0.970
-8	0.871	-8	0.954
-10	0.830	-10	0.938
-12	0.784	-12	0.923
-14	0.736	-14	0.909

4.2.3 Cut on the scattering angle for Coulomb excitation

With relativistic RIB on a Pb target, atomic processes, Coulomb excitation and nuclear reactions dominate at different scattering angle regions. Atomic processes focus at $\theta \approx 0^\circ$. As θ becomes larger, according to the theoretical calculation for the ^{28}Mg projectile (see fig. 3 and fig. 4 in chapter 2.2), at $\theta \leq \theta_{\text{max}} \approx 21$ mrad Coulomb excitation is dominant; when θ becomes even larger, in a narrow range of $21 \leq \theta \leq 27$ mrad, nuclear excitation takes priority; finally when the two colliding nuclei overlap each other and $\theta > 27$ mrad, nuclear fragmentation reaction channels associated with change of mass and/or charge numbers open.

The following θ cuts may help to select events originating from Coulomb excitation: (1) by requiring a minimum θ , the large atomic background can be suppressed; (2) by setting an upper limit to θ , the nuclear reactions are excluded; (3) if the resolution of θ is good enough, nuclear excitation, whose dominant region is very near to that of Coulomb excitation because of the relativistic beam energies, can also be distinguished.

The measured distribution of θ with ^{28}Mg on the Pb target is shown in fig. 22. In the upper figure, with the beam trigger which means no reaction but only atomic straggling takes place, θ dominates at $\sim 0^\circ$ and falls suddenly at ~ 8 mrad. The middle one requires

$Z_2 = Z_1$, γ -trigger with γ -multiplicity $M_\gamma > 0$ and at least one γ -ray with energy $E_\gamma \geq 1000$ keV. Comparing to the upper one, the distribution around $\theta_{max} \approx 21$ mrad corresponding to Coulomb and nuclear excitation is much stronger. The events at $\theta \approx 0^\circ$ may originate from high energetic atomic processes. Subtracting it by assuming a similar distribution as in the upper panel, we get the dashed line which dominates at $\theta \approx 12 \sim 20$ mrad. The picture in the bottom is associated with $M_\gamma > 0$ in the CB and at least one neutron detected in LAND. The events originating from pure atomic processes with $\theta \approx 0^\circ$ are strongly suppressed by the strict trigger condition. The distribution at $\theta < \theta_{max}$ may correspond to giant resonances while that at $\theta > \theta_{max}$ are associated with few nucleon removal reactions. Because of the scattering angle acceptance of the detection system, the intensity decreases steeply at $\theta \approx 30$ mrad.

Comparing the three spectra in fig. 22, we find the mean value of θ becomes bigger for more violent reactions but, mainly due to the finite θ resolution, the overlap of the regions is very strong. As discussed in chapter 4.2.1, the intrinsic resolution of θ caused by the spacial resolution of the trajectory detectors was measured as 5 mrad. In addition to that, the atomic angular straggling with the thick Pb target was simulated as $5 \sim 6$ mrad. The combined resolution was therefore not sufficient to distinguish Coulomb and nuclear excitation whose dominant θ regions are only a few mrad apart. Nevertheless, requiring a minimum θ is quite useful to suppress the high energetic atomic background which is difficult to be distinguished from γ -rays by other ways, so as to improve the γ -lines originating from Coulomb and/or nuclear excitation. An upper limit on θ helps not too much because by setting other cuts like γ -trigger, $M_\gamma = 1$, $Z_2 = Z_1$ and/or $A_2 = A_1$, nuclear reactions are almost excluded anyhow.

Compromising between the statistics of excitation and a tolerable background, in addition to the condition of $Z_1 = Z_2$, γ -trigger and $M_\gamma = 1$, a cut of $\theta = 8 - 28$ mrad was set to improve the γ -lines associated with inelastic excitation, in which more than 70% is from Coulomb excitation according to the theoretical calculation in chapter 2.2. Fig. 23 shows γ -spectra with different cuts on θ . In the upper spectrum with $\theta = 0 - 8$ mrad, we can hardly see any peak but mainly atomic background; whereas in the lower one with $\theta = 8 - 28$ mrad, the 1470 keV peak from the first $2^+ \rightarrow 0^+$ γ transition in ^{28}Mg clearly shows up.

In brief, the resolution of θ obtained with the present set-up is not sufficient to distinguish Coulomb excitation from nuclear excitation. However, requiring a minimum θ is helpful to suppress atomic background and to improve the γ -lines associated with inelastic excitation. Because of the $\sim 30\%$ efficiency of the θ determination, this method is inapplicable for γ -lines with poor statistics.

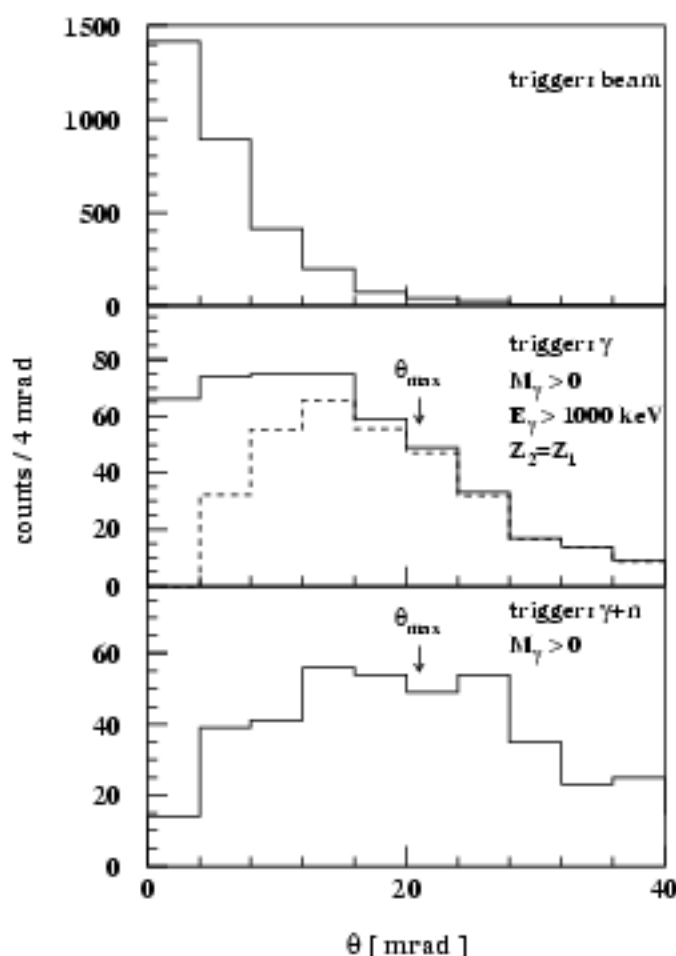


Figure 22: Scattering angle distribution of ^{28}Mg on the Pb target with different conditions. $\theta_{\text{max}} \approx 21$ mrad, where nuclear excitation takes priority over Coulomb excitation, is marked. Upper: with beam trigger almost only atomic straggling exists. Middle: with γ -trigger etc., Coulomb and nuclear excitations coexist around $\theta = \theta_{\text{max}}$ while the high energetic atomic background is seen at $\theta \approx 0^\circ$. The dashed line is obtained by subtracting the atomic contribution (assuming it is similar to that in the upper panel) from the solid line. Bottom: requiring γ and neutron coincidence, giant resonances at $\theta \leq \theta_{\text{max}}$ and few nucleon removal reactions at $\theta > \theta_{\text{max}}$ take place. The sudden decrease at $\theta \approx 30$ mrad in the middle and bottom panels is partly because of the scattering angle acceptance of the detection system.

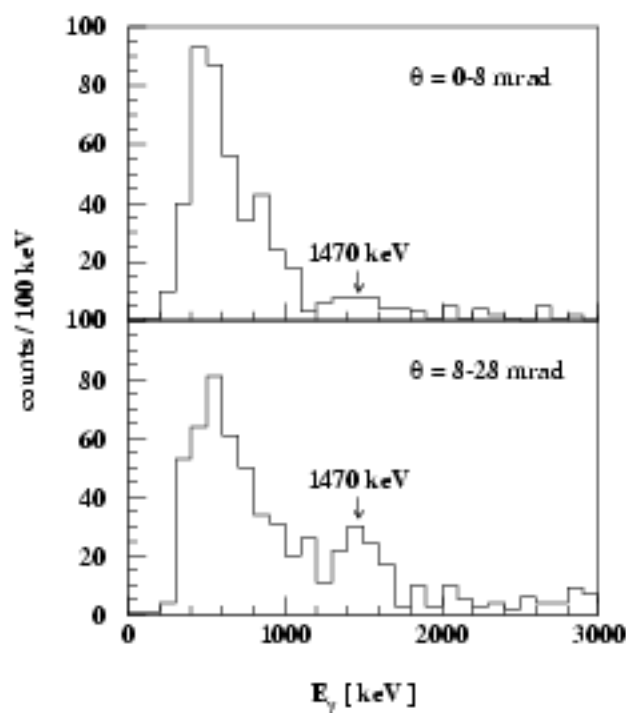


Figure 23: Gamma-spectra with different θ cuts in addition to the condition of $Z_1 = Z_2$, γ -trigger and $M_\gamma = 1$. With $\theta = 8 - 28$ mrad, the 1470 keV peak corresponding to the first $2^+ \rightarrow 0^+$ γ transition in ^{28}Mg is improved, while the atomic background at 300-1000 keV is suppressed.

4.3 The γ -spectrometer Crystal Ball (CB)

The analysis of the γ -data measured by the CB deals with the following aspects: (1) the energy calibration and Doppler correction; (2) the time calibration and a proper time cut for prompt γ -rays; (3) the γ -multiplicity and neighbour add; (4) the energy and angle dependent efficiency of the CB.

4.3.1 Energy calibration and resolution

The energy calibration of the CB was done both before and after the beam time by using ^{152}Eu , ^{226}Ra and ^{88}Y sources with γ energies ranging from 121.8 keV to 2204.1 keV (see table 6).

Table 6: Energy calibration and the intrinsic resolution of the CB

source	^{152}Eu	^{152}Eu	^{226}Ra	^{88}Y	^{226}Ra	^{152}Eu	^{88}Y	^{226}Ra
E_γ (keV)	121.8	344.3	609.3	898.0	1120.3	1408.0	1836.1	2204.1
δE_γ (FWHM, keV)	21.8	38.6	54.0	69.2	78.5	97.0	115.6	137.0
$\delta E_\gamma/E_\gamma$ (%)	17.9	11.2	8.86	7.70	7.01	6.89	6.30	6.21

In order to check possible calibration changes during the beam time, a linear calibration was done by using the two γ lines from the online raw spectra of the ^{88}Y source both before and after the beam time. For nearly all the NaIs, the offset shift was less than 10 keV and the gain shift was less than 5%. Only for crystal 92, the offset shifted by about 12 keV and the gain shifted by about 27%. This module was therefore excluded in the analysis.

After that, a quadratic calibration was performed by using all the eight γ lines from the measurement after the beam time. The calibration was checked by comparing all the peak positions ($E_{\gamma ij}$, with $i=1,162$ and $j=1,8$) in the energy-calibrated spectra with the real γ line $E_{\gamma j}$. The relative energy deviation $(E_{\gamma ij} - E_{\gamma j})/E_{\gamma j}$ for all the peak positions was below 5% which was within the 7~8% resolution of NaI crystal.

The average intrinsic energy resolution of the OR of all the CB modules was obtained as $8 \pm 2\%$ for E_γ from ~ 500 to ~ 2500 keV (see table 6 and fig. 24), reflecting the good quality of the calibration.

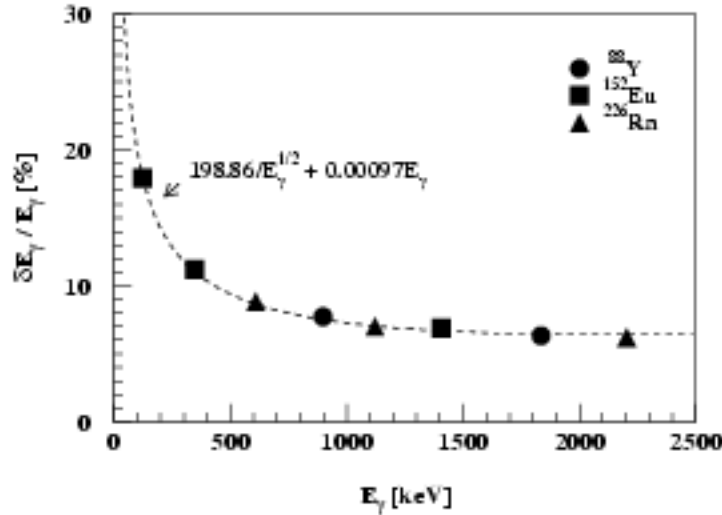


Figure 24: The intrinsic energy resolution of the CB.

4.3.2 Doppler correction

As described in chapter 3.1.2, the high velocity of the excited RIB nuclei causes the energy of the decay γ -rays E_γ to be severely Doppler shifted. To recover E_γ from the measured γ -energy E_γ^{lab} , formula (23) in chapter 3.1.2 was used, with θ_γ being simplified as the angle between the center of the associated NaI crystal and the beam direction, and β as the velocity of the projectile at the center of the target (because γ -decay could happen at any position between the front and the rear face of the target). β was calculated event by event:

$$\beta = \frac{\beta_1 + \beta_2}{2}, \quad (43)$$

where β_1 and β_2 are the velocities of the projectile in front of and behind the target with a resolution of 0.7% (see chapter 4.1.1). The difference between β_1 and β_2 was 0.5% \sim 2.0% depending on the target thickness and the charge number of the projectile.

As an example, fig. 25 shows the γ spectra of the CB for the deexcitation of ^{28}Mg at a velocity $\beta=0.605$ without and with Doppler correction. Particle identification $A_1 = 28$,

$Z_1 = Z_2 = 12$ and γ multiplicity $M_\gamma = 1$ were required. Without Doppler correction there is no observable peak in the spectrum. After Doppler correction, the 1.47 MeV peak corresponding to the γ transition from the first excited state to the ground state of ^{28}Mg can be clearly seen. The energy resolution derived from the bottom spectrum is about 17% (refer also to fig. 34: top) which was mainly caused by the expected $\sim 15\%$ Doppler broadening (see chapter 3.1.2) and the $\sim 8\%$ intrinsic resolution of the CB.

Doppler correction assuming the projectile being the emitter has always been applied in the γ -spectra if not specified.

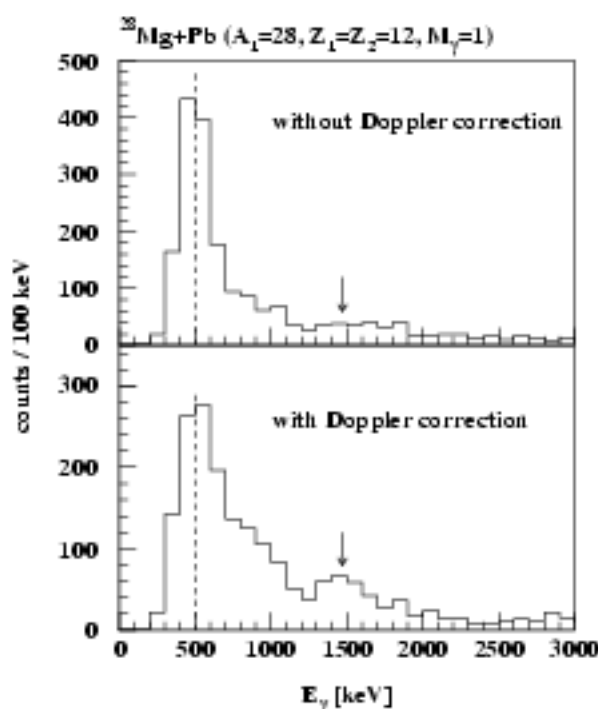


Figure 25: The γ spectra of ^{28}Mg with velocity $\beta=0.605$ on the Pb target without (top) and with (bottom) Doppler correction. The 1.47 MeV peak position corresponding to the γ transition of ^{28}Mg is marked. The dashed line indicates the CFD-threshold.

4.3.3 Time calibration and resolution (source measurement)

The time calibration of the individual CB channels was done event by event employing the following relation:

$$t_{CB} = [(4096 - N_{TDC}) - a_{0i}] \cdot a_{1i} \quad (i = 1, 162), \quad (44)$$

where N_{TDC} is the TDC channel number, a_{0i} and a_{1i} are the offset and gain parameters. As described in chapter 3.3.1, each TDC channel had an individual START from its corresponding NaI and all the TDCs had a common STOP either from POS01 (during the beam time) or from the earliest NaI signal in an event (during calibration measurement with the source). The gain parameters were obtained by using a pulser which produced one pulse every 20 ns. The parameters were different for different TDCs and fluctuated between 50 and 52 ps/channel. The offsets were obtained such that the time spectrum for each NaI peaked at the 0 ns position.

To determine the time resolution, we analyzed the measurement with the ^{88}Y source which has two γ -rays with energy of $E_{\gamma 1} = 898.0$ keV and $E_{\gamma 2} = 1836.1$ keV from a cascade (see the level scheme on the top-right corner in fig. 26). In order to reduce background in the time spectra, a sum energy below 3 MeV was demanded to suppress the pile-up events. About 5.6% events had a sum energy above 3 MeV (see fig. 26) which gave a rough value of the pile-up effect corresponding to the source strength of $\sim 2 \times 10^5$ Bq. In the measurement with RIB, the pile-up effect is negligible because of the low beam intensity (60 kHz) and the Pb absorber shielding abundant low energy X-rays.

During the source measurement, both START and STOP signals for the TDCs were obtained from the NaIs (refer to fig. 14 in chapter 3.3.1). Therefore in the time spectra for most of the NaIs, there was a spike corresponding to self-trigger. In order to get rid of the spike, we required only time signals from the TDCs whose START and STOP were delivered by two different NaIs.

The calibrated time spectrum of the ^{88}Y source is shown in fig. 27 with the condition that at least two NaIs are firing with γ -energy bigger than the CFD threshold of ~ 500 keV. A resolution of $\delta t_{CB}^{OR} = 5.4$ ns (FWHM) is obtained. Therefore the intrinsic time resolution of the NaIs in the CB is $\delta t_{NaI} = 5.4/\sqrt{2} = 3.8$ ns.

4.3.4 In-beam time spectra

In the in-beam measurement, the common STOP was from POS01 (refer to fig. 14 in chapter 3.3.1) with a resolution of about 100 ps which was much smaller than that of NaIs ($\delta t_{NaI} = 3.8$ ns), therefore the time spectra of γ -rays from the RIB measurement should have

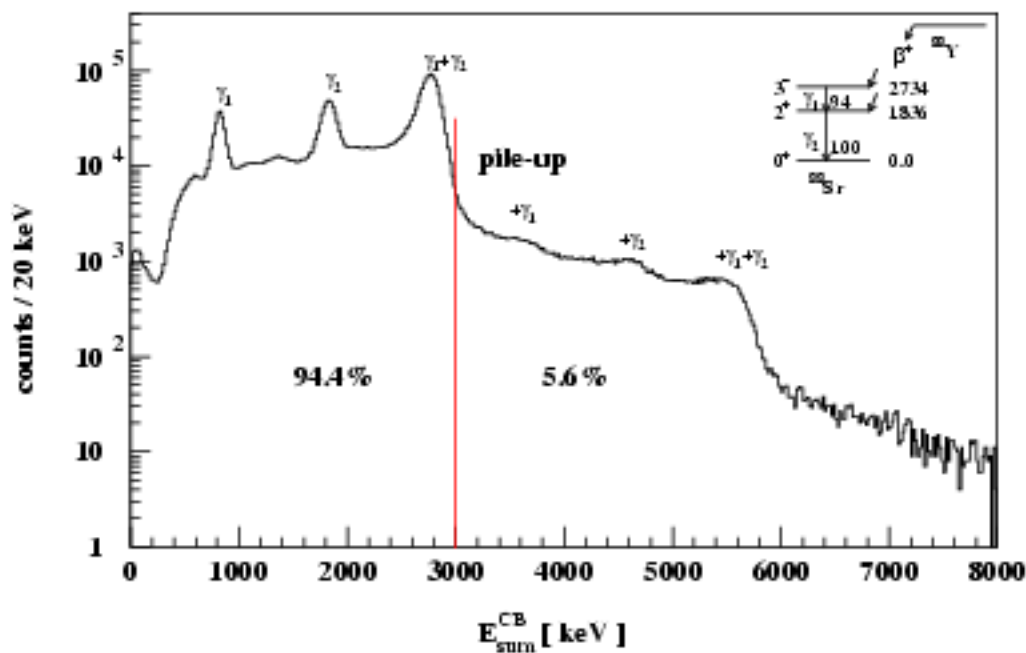


Figure 26: The sum energy from the CB in the ^{88}Y -source measurement. The events above 3000 keV resulting from pile-up. The source strength was $\sim 2 \times 10^5$ Bq.

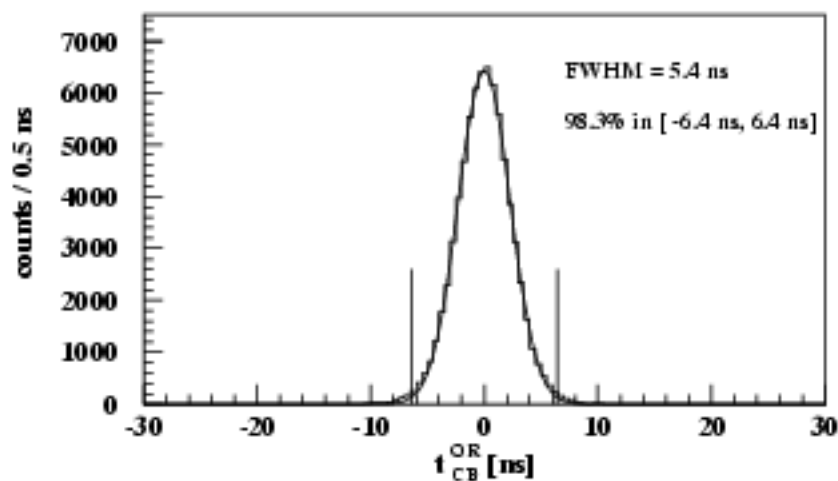


Figure 27: Time spectrum of the CB from the ^{88}Y -source measurement with a condition of $E_{\text{sum}}^{\text{CB}} < 3000$ keV to suppress the pile-up events. See text for details.

a width of about δt_{NaI} . In the analysis with the RIB, a time cut of $[-4.5, 4.5]$ ns corresponding to $2.36 \times \delta t_{NaI}$ was set. For a standard Gaussian distribution, 99.5% events should be in this cut. Actually in the time spectrum from the ^{88}Y source measurement with a resolution of $\sqrt{2}\delta t_{NaI}$, 98.3% events were in the equivalent time cut of $2.36 \times \sqrt{2}\delta t_{NaI}$ i.e. $[-6.4, 6.4]$ ns.

Different nuclear species in the RIB reach the target position at different time with respect to POS01 because of different velocities. The time at the target position t_t is calculated from the velocity of particles in front of the target (refer to chapter 4.1.1) and the flight path of 1175 cm between POS01 and the target. As shown in the top-left spectrum in fig. 28, the shift of t_t for different beam species can be up to 10 ns. To obtain proper CB time spectra this shift was corrected for.

Since the common STOP signals from POS01 had a time relation different from the logical OR of the CB channels, an independent offset calibration had to be performed for the in-beam time spectra. The offsets were set in such a way that the time spectrum from each NaI module peaked at the 0 ns position after the correction of t_t .

The top-right spectrum in fig. 28 shows the correlation between the γ -time t_γ and the γ -energy E_γ with the RIB on the Pb target. For different energy regions, the time distributions are different. This can be seen more clearly in the bottom spectra in fig. 28 which are the projections of t_γ with different E_γ cuts. As the CFD thresholds were set as $E_\gamma^{lab} \sim 500$ keV, there was no time signal for $E_\gamma < 300$ keV, therefore the “walk” effect associating with low energy needs not to be considered. In the energy region of 300 to 600 keV, the time distribution is sharp and the background is small. As the energy increases, the time distribution develops a tail, which might originate from the time of flight of neutrons from the target to the detector, and the background increases. When the energy is above 7000 keV, we get a time spectrum which is distributed not around 0 ns but around -10 ns. These were not γ -rays any more but high energetic particles generated by interactions of the beam with upstream material and/or the target causing an energy overflow, i.e. the energy of the particles deposited in the NaIs was so high that it was out of the range of the QDCs.

By requiring E_γ below the energy overflow, we could get rid of the events associated with particle emission and get cleaner time spectra as shown in fig. 29. The shaded area corresponds to the time cut $[-4.5, 4.5]$ ns for prompt γ -rays. For the Pb target, there were 50% events in the cut; for the C target, 62.4%; for the measurement without target, there were 29.9% events in the cut which could be interpreted as the γ -rays from the interaction between the beam halo and the surrounding material (e.g. the target frame, the absorber).

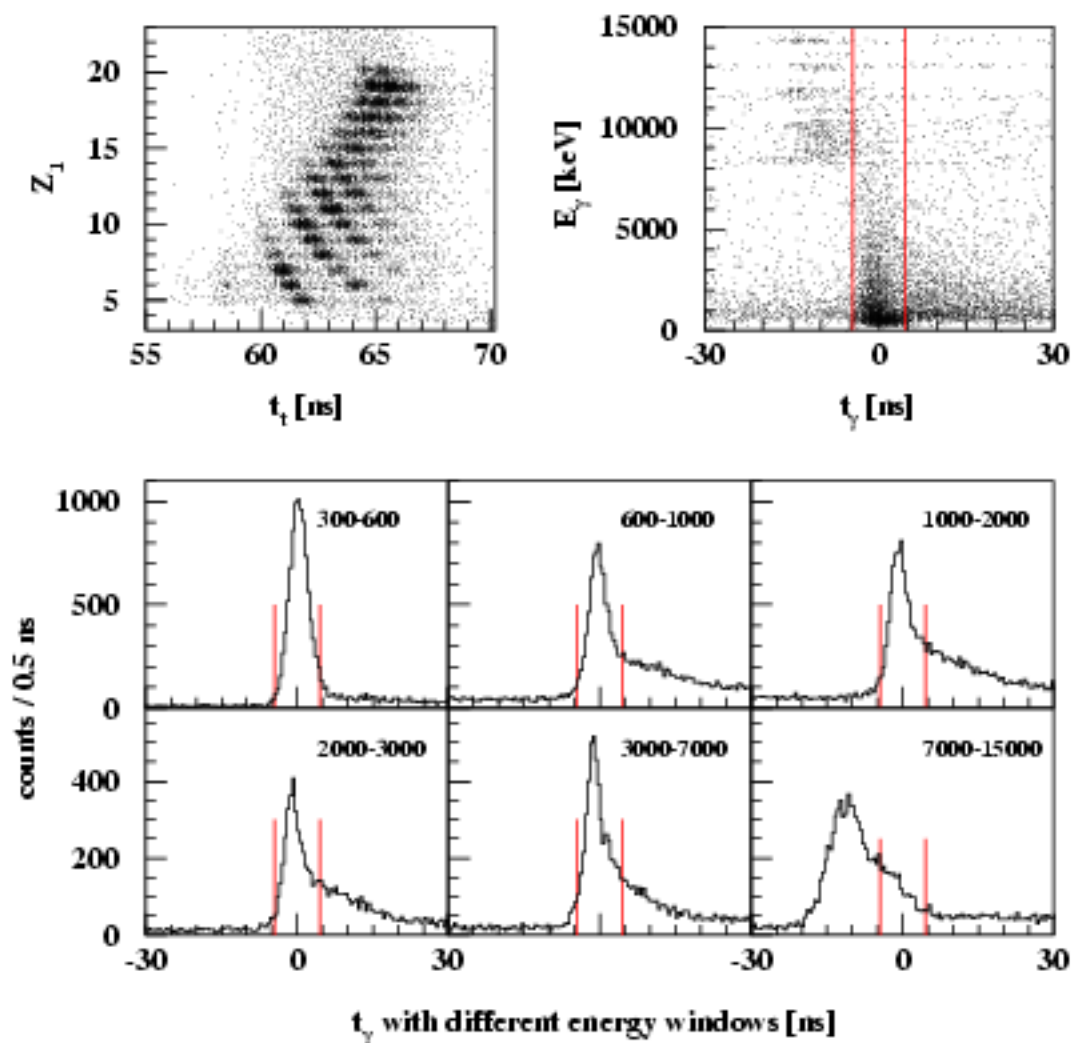


Figure 28: The time distribution of the particles in the RIB from POS01 to the target position (top-left); the relation between the γ -time t_γ and the γ -energy E_γ from the CB with the RIB on the Pb target (top-right); the projections of t_γ with different E_γ cuts (bottom) which show the relevant time distributions. The time cut $[-4.5, 4.5]$ ns for prompt γ -rays is marked.

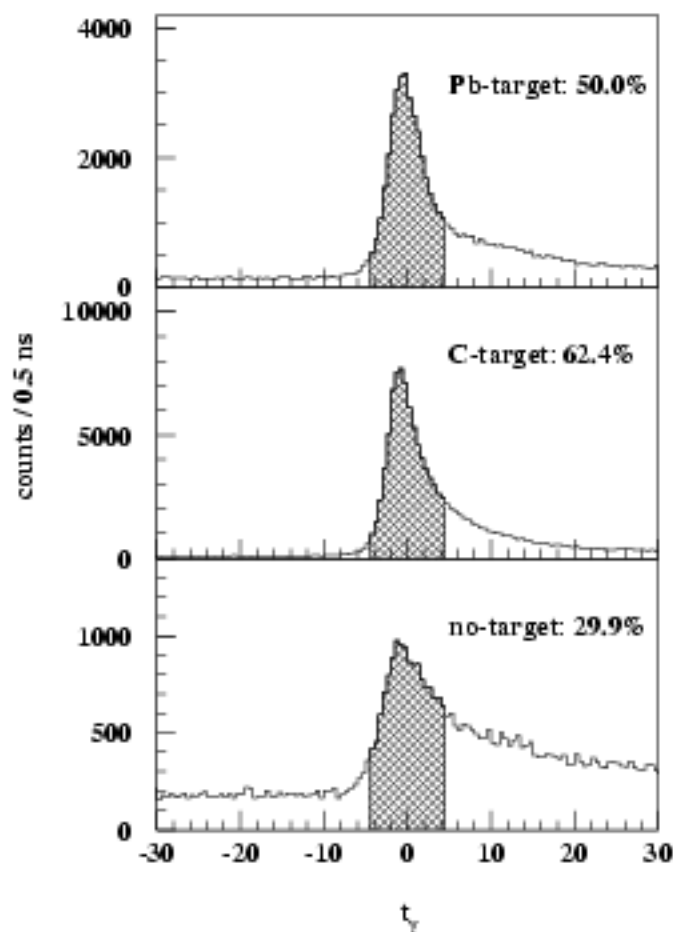


Figure 29: The time spectra from the CB for different targets which excludes the events associated with particle emission. The shaded area corresponds to the time cut $[-4.5, 4.5]$ ns for prompt γ -rays. The percentage of events in the shaded area as compared to the number of events with $-30 \leq t_\gamma \leq 30$ ns is given.

4.3.5 Multiplicity and neighbour add

The γ -multiplicity M_γ is represented as N_{NaI} , the number of NaIs which offer a “good time” signal in one event. Here “good time” means within the time window which was set for prompt γ -rays. As discussed in chapters 4.3.3 and 4.3.4, for the source measurement (see fig. 27), this window was $[-6.4, 6.4]$ ns with nearly all the time signals inside; while for the measurement with the RIB (see fig. 29), the equivalent one was $[-4.5, 4.5]$ ns, where about 50% time signals were inside, the rest “bad time” signals were interpreted as from background and disregarded in the analysis.

The NaIs considered for N_{NaI} must have had an energy signal higher than the ~ 500 keV CFD threshold.

The N_{NaI} distribution from the ^{88}Y source measurement is shown in fig. 30 (top). Most of the events were associated with $N_{NaI}=2$ and the mean value was $\langle N_{NaI} \rangle=1.8$. This fits well with the true γ -multiplicity $M_\gamma=2$ of ^{88}Y .

As shown in the middle and bottom panels in fig. 30, the multiplicity N_{NaI} for the measurement with the RIB was low. Requiring $Z_2 = Z_1$, $\langle N_{NaI} \rangle=1.8$ and 2.3 was obtained for ^{28}Mg on the Pb and C target measurement, respectively.

If the energy from one γ -ray is deposited in two or more neighbouring NaIs because of Compton scattering, the original γ -energy can be recovered by neighbour add, i.e. by adding up the energies of the neighbouring NaIs. On the other hand, one should be careful not to add up the energies of two or more γ -rays which fire accidentally neighbouring NaIs. In our case the probability of neighbouring NaIs fired by two or more γ -rays was very low because of the low multiplicity N_{NaI} .

Considering the big volume of each individual NaI, for one γ -ray with energy around 1 MeV, only the scatterings which result in two neighbouring NaIs fired, were taken into account. The probability for three or even more neighbouring NaIs fired by one γ -ray was checked to be very low. Assuming one γ -ray deposits its energy E_γ in two neighbouring NaIs as E_{γ_1} in NaI₁ and E_{γ_2} in NaI₂, scatterings can be summarized into three types according to the time signals of NaI₁ and NaI₂: (1) “good time+no time”: E_{γ_1} is above the threshold and give a “good time” signal while E_{γ_2} is below the threshold and there is no corresponding time signal; (2) “good time+good time”: both E_{γ_1} and E_{γ_2} are above the threshold; (3) “no time+no time”: both E_{γ_1} and E_{γ_2} are below the threshold. For $E_\gamma \sim 1$ MeV and the threshold ~ 500 keV, the dominant scattering was obviously the “good time+no time” type. Therefore the neighbour add was only done for this mode.

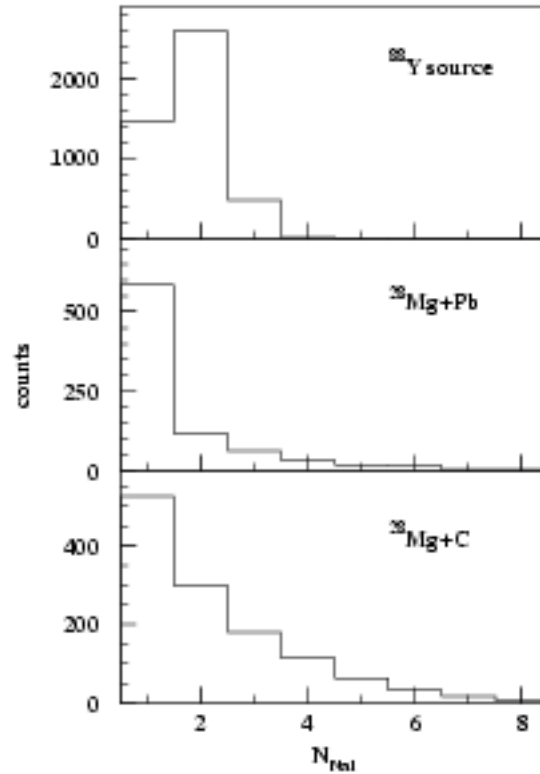


Figure 30: The multiplicity distribution of the CB for the ^{88}Y source measurement (top), the RIB ^{28}Mg on the Pb (middle) and C target (bottom) measurement. $Z_2 = Z_1$ is required.

The neighbour add for the “good time + no time” scattering was performed as follows: (1) all the NaIs which had only a small energy signal but no time signal were checked in order to find the neighbour of the NaI with “good time”; (2) E_{γ}^{lab} of the neighbouring “no time” NaI was summed up to that of the “good time” NaI; (3) because for γ -rays with energy larger than 511 keV, it is more likely to deposit more energy in the first step of Compton scattering [Kas94], the total energy was Doppler corrected according to the angle of the NaI with “good time” as well as with larger energy.

After neighbour add, the background in γ -spectra could be suppressed and the γ -peak be improved. The background subtracted peak intensity could be increased by $\sim 40\%$. Neighbour add has been applied in all the γ -spectra if not specified differently. Representing the γ -multiplicity M_{γ} by N_{NaI} is a good approximation.

4.3.6 Efficiency

For the energy calibration, the γ -sources were most of the time placed outside of the scattering chamber with the CB opened; for the efficiency calibration, there was one run after the test beam time with a ^{88}Y source at the target position and CB closed. The intensities for the two ^{88}Y transitions served as reference points for the efficiency determination of the CB by Monte Carlo simulations using GEANT developed at CERN [Cer94].

In the GEANT simulation the main physics processes, the geometry of the CB, the 500 keV threshold and the ancillary set-up (the absorber, the scattering chamber, etc.) were simulated. Altogether 10 γ -energies from 609.3 keV to 4000 keV were calculated with 100000 events for each one.

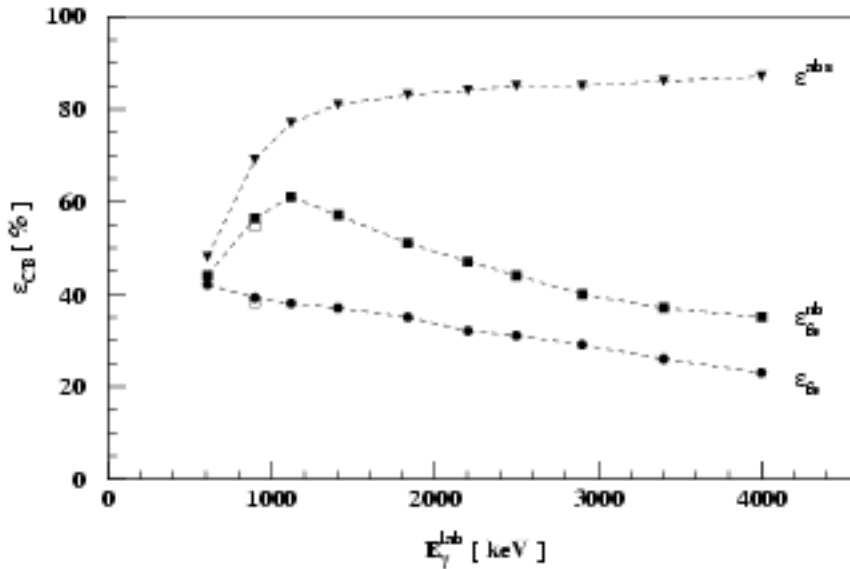


Figure 31: The energy dependent efficiency of the whole CB (10 out of 162 NaIs were missing) with absorber and 500 keV threshold for three different modes: standard ϵ_{fe} , neighbour add ϵ_{fe}^{nb} and absolute ϵ^{abs} . The values at $E_\gamma = 898$ keV from the ^{88}Y source measurement were marked by open squares. See text for details.

The energy dependent efficiency of the whole ball for three different modes is shown in fig. 31. ϵ_{fe} stands for the efficiency of full energy deposited in a single crystal (the standard

case) while ε_{fe}^{nb} is the improved one by adding up the energies which are scattered to the neighbouring crystals (“good time + no time”). Because of the threshold, neighbour add helps not too much to the 609.3 keV γ -line but for the higher γ -energies, ε_{fe}^{nb} increases by at least $\sim 30\%$ comparing to ε_{fe} . The absolute efficiency ε^{abs} means the efficiency that a γ -ray interacts in any way with the CB. Above ~ 1000 keV it reaches the maximum value of $\sim 90\%$ (the solid angle efficiency of the CB was $152/162 = 93\%$ because of the removed and “bad” NaI modules, see chapter 3.3.1.) and stays rather constant at higher energies.

At $E_\gamma = 898$ keV, ε_{fe} and ε_{fe}^{nb} derived from the ^{88}Y source measurement are 38.3% and 54.7% compared to 39.2% and 56.4% from the GEANT simulation. This shows the high accuracy of the GEANT simulation.

Because the absorber, composed of 2 mm aluminium and 2 mm lead, was a tube along the beam line (see fig. 12 in chapter 3.2.2), the absorption was different for γ -rays with different emission angle θ_γ . Therefore the efficiency of the CB ε_{CB} also depends on θ_γ . In the following, ε_{fe}^{nb} from the neighbour add mode will be used representing ε_{CB} .

In order to derive the θ_γ dependent efficiency, the CB was divided into 25 θ -rings along the beam line (The 1st and the 25th rings, corresponding to $\theta_\gamma = 0^\circ, 180^\circ$ with one NaI for each ring, were missing because of the beam tube.). NaIs at each θ -ring have the similar θ_γ . As examples, fig. 32 shows the solid angle normalized efficiency of 4 θ -rings at forward, medium and backward angles. Because of the tube absorber, the efficiency at forward and backward angle is lower than at medium angle. All the points for each θ -ring were fitted by a 4th or 5th order polynomial.

For all γ -rays detected by the CB the corresponding efficiency $\varepsilon_{fe}^{nb}(\theta_\gamma, E_\gamma^{lab})$ can be calculated by using the relevant polynomial out of the 23 ones mentioned above. We take the γ -rays with an original energy of $E_\gamma = 1200$ keV emitted from projectiles at velocity of $\beta = 0.589$ as an example (see fig. 33). For each θ -ring, the Doppler shifted γ -energy E_γ^{lab} (top) and then the corresponding $\varepsilon_{fe}^{nb}(\theta_\gamma, E_\gamma^{lab})$ (bottom) were calculated. ε_{fe}^{nb} is larger at medium angle than at forward and backward angles because of the tube absorber while the asymmetry about $\theta_\gamma = 90^\circ$ was caused by its energy dependence and different $E_\gamma^{lab}(\theta_\gamma)$.

To derive a cross section, the number of γ -rays detected by the CB needs to be transferred into the real number of emitted γ -rays. This was done individually for each θ -ring. For example, if 10 γ -rays were detected by the middle θ -ring ($\theta_\gamma = 89 - 91^\circ$) with $E_\gamma^{lab} = 1000$ keV, $\varepsilon_{fe}^{nb} = 63\%$ was obtained from the relevant polynomial. Considering the solid angle efficiency of $\varepsilon_\Omega = 14/16 = 87.5\%$ (14 crystals out of 16 worked properly), $10/0.62/0.875 = 18$ is derived, which means there were actually 18 γ -rays emitted in the direction of the middle θ -ring.

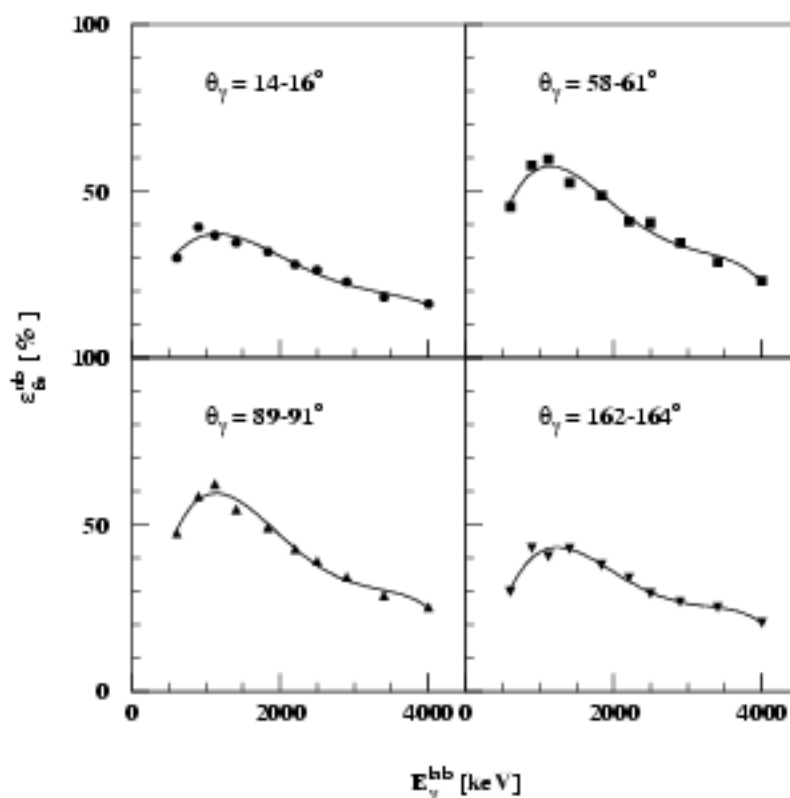


Figure 32: The solid angle normalized neighbour add efficiency of four θ -rings of the CB at forward, medium and backward θ_{γ} angles (absorber and threshold included). The curves correspond to the 4th or 5th order polynomials fitting the points.

The two θ -rings at $\theta_{\gamma} = 0^{\circ}$ and 180° which were removed for the beam tube were assumed to have the same efficiency (solid angle normalized) as the neighbouring θ -rings at $\theta_{\gamma} = 14^{\circ}$ and 164° respectively. Furthermore, referring to the angular distribution of γ -rays in the lab system (fig. 7 (d) in chapter 3.1.2), the intensity of γ -rays at $\theta_{\gamma} = 0^{\circ}$ and 180° were assumed to be the same as $\theta_{\gamma} = 14^{\circ}$ and 164° respectively. With these two assumptions, the 0° and 180° θ -rings could be merged into their neighbouring rings, i.e., the solid angle efficiency ε_{Ω} of the 14° θ -ring (fully mounted with 6 NaIs) decreased to $6/7$ and ε_{Ω} of the 164° θ -ring (4 out of 6 NaIs were mounted) decreased to $4/7$.

The Lorentz transformation for solid angle is unnecessary because we do not calculate the differential cross section $\frac{d\sigma}{d\Omega}(\theta_{\gamma})$ but the cross section integrated over the 4π solid angle.

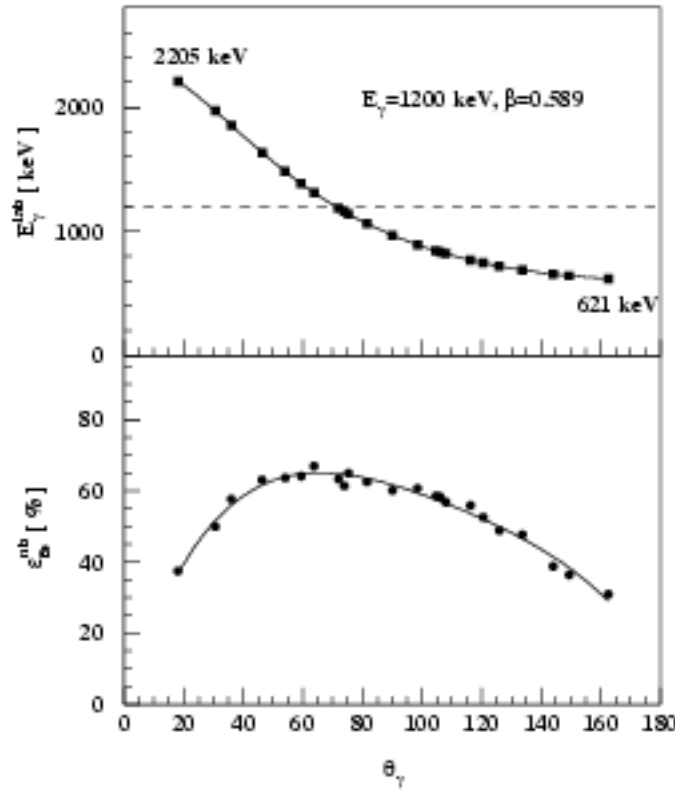


Figure 33: The Doppler shifted energy E_γ^{lab} of γ -rays with an original energy of $E_\gamma = 1200$ keV emitted from projectiles at velocity of $\beta = 0.589$ (top) and the corresponding efficiency $\epsilon_{fb}^{nb}(\theta_\gamma, E_\gamma^{lab})$ (bottom).

4.4 Experimental cross section determination

For a thin target the cross section can be deduced by

$$\sigma = \frac{N_\gamma}{N_{proj} \times \rho}, \quad (45)$$

with N_γ as the number of de-excitation γ -rays, N_{proj} the number of projectiles which is obtained from the number of the events associated with the beam trigger (refer to chapter 3.3.2), and ρ the number of target nuclei per unit area which is derived from the thickness d and the mass number A_T of target

$$\rho = 6.02 \times 10^{-4} \times \frac{d[g/cm^2]}{A_T} \quad (mb^{-1}).$$

In our experiment, the reaction rates of the beam particles with the Pb and C target were both below 1% thus the probability for a beam particle to have more than one reactions with the target nuclei was negligibly small. Therefore formula (45) can be used for the cross section determination.

For the Pb and C target with a thickness of 0.942 and 0.536 g/cm², ρ is 2.73×10^{-6} mb⁻¹ and 2.69×10^{-5} mb⁻¹, respectively.

N_{proj} can be obtained from the number of events with the beam trigger (see chapter 3.3.2) with cuts on Z_1 and A_1 , the charge and mass number in front of the target.

In order to obtain N_γ , the number of decay γ -rays emitted, we need to correct the γ -spectra detected by the CB channel by channel with a weighting factor $1/\varepsilon_{CB}(\theta_\gamma, E_\gamma^{lab})/\varepsilon_\Omega(\theta_\gamma)$ (see chapter 4.3.6). As an example, fig. 34 shows the detected and the “corrected” γ -spectrum of ²⁸Mg on the Pb target with the condition of γ -multiplicity $M_\gamma=1$. Fitting the “corrected” spectrum (bottom: solid line) and its background (dashed line), the number of counts of peak with background $N_{peak+back}$ and the number of counts of background N_{back} are obtained. The background subtracted peak intensity is

$$N_{peak} = N_{peak+back} - N_{back} .$$

N_{peak} is just N_γ , the number of γ -rays emitted in the decay of the 2_1^+ state in ²⁸Mg.

The uncertainty of N_{proj} and N_{target} are below 1%, therefore the cross section error comes mainly from the uncertainty of N_γ (or N_{peak}) which has two sources: the CB efficiency uncertainty and the peak intensity uncertainty.

As discussed above, in order to deduce the peak intensity N_{peak} , we need the CB efficiency $\varepsilon_{CB}(\theta_\gamma, E_\gamma^{lab})$ which was obtained by Monte Carlo simulation using GEANT (see chapter 4.3.6). The simulated set-up can never be exactly the same as the real experiment. From experience, the deviation should be $\leq 5\%$. There is also statistical error in the simulation. For each energy point, 100000 events were simulated for the total ball which was divided into 25 θ -rings, i.e. on the average 4000 events for each θ -ring. This causes an error of $< 2\%$. These two effects make up the uncertainty of the CB efficiency

$$\delta_{\varepsilon_{CB}} \approx \sqrt{(5\%)^2 + (2\%)^2} = 6\% .$$

The statistical error δ_{stat} of the peak intensity is

$$\delta_{stat} = \frac{\sqrt{(N_{peak+back} + N_{back}) \times \overline{\varepsilon_{CB}}}}{N_{peak} \times \overline{\varepsilon_{CB}}} , \quad (46)$$

with $\overline{\varepsilon_{CB}}$ standing for the mean value of the CB efficiency which is around 50%. Because of poor statistics, this uncertainty is relatively large, ranging from 10% to 20%.

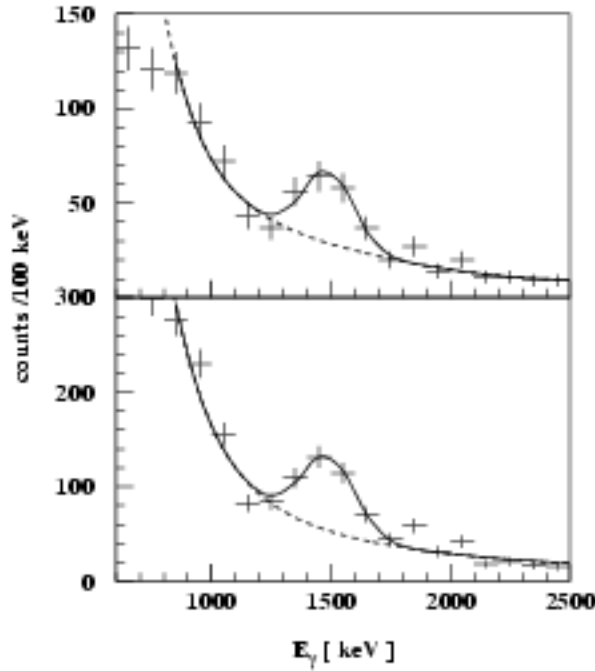


Figure 34: Gamma-spectrum of ^{28}Mg on the Pb target ($M_\gamma=1$) without (top) and with (bottom) the CB efficiency correction. The spectra and their background are fitted with solid and dashed lines. See text for details.

Using different functions to fit the background, the uncertainty of the peak intensity determination can be estimated as

$$\delta_{fit} \approx 15\% .$$

Totally, the uncertainty of N_{peak} , i.e. the uncertainty to determine experimental cross section, is

$$\frac{\delta\sigma}{\sigma} \approx \sqrt{(\delta_{stat})^2 + (\delta_{fit})^2 + (\delta_{\varepsilon_{CB}})^2} \quad (47)$$

which ranges from 20% to 30%, depending mainly on the count statistics in the γ -peak.

5 Experimental results and comparison with calculations

Using relativistic RIB, atomic processes, Coulomb excitation, nuclear excitation and nuclear reactions may occur. The former two processes with probability proportional to $\sim Z_t^2$ are much stronger in the Pb target ($Z_t = 82$, $A_t = 208$) than in the C target ($Z_t = 6$, $A_t = 12$); while nuclear processes take place in both targets with comparable probability proportional to $\sim A_t^{1/3}$ (Z_t and A_t stand for the charge and mass number of the target). In the experiment, the nuclear reactions with the C target yielded much higher statistics than that with the Pb target simply because the strong atomic and Coulomb processes in the Pb case saturated the data acquisition system which had a rather limited maximal trigger rate.

Coulomb excitation with Pb is the main goal of the investigation. By gating on $Z_1 = Z_2$ and $A_1 = A_2$, nuclear reactions characterized by mass and/or charge change can be ruled out, but atomic processes and nuclear excitation are still present. The atomic background can be suppressed by requiring a γ -multiplicity $M_\gamma > 0$, a minimum E_γ and/or, if statistics is sufficient, a minimum scattering angle θ . Nuclear excitation can not be separated by setting an upper limit on θ because the θ resolution was not sufficient. Nevertheless, nuclear excitation can be estimated from the measurement with C in which the probability for Coulomb excitation is so small that nuclear excitation can be taken as the dominant contribution to inelastic excitation.

To get a general idea of the probability for different reactions, the Z_2 vs. Z_1 distributions of the RIB with the Pb and C targets are compared in fig. 35, with the condition of $M_\gamma > 0$ and $E_\gamma > 1000$ keV to strongly suppress atomic background (cut on θ is not applied). In reactions with Pb, $\sim 40\%$ do not change charge number because Coulomb excitation is strong; while with C, only $\sim 25\%$ keep the original charge number and the rest ends with $Z_2 < Z_1$ via proton emission because nuclear interactions are dominant. As examples, the inlay pictures show the Z_2 distribution of the incoming Mg isotopes ($Z_1 = 12$).

Gating further on $Z_2 = Z_1 = 12$ and $A_1 = 28$ in order to investigate the probability of Coulomb excitation, the A_2 distributions after reactions of ^{28}Mg with the Pb and C target are plotted (fig. 36). Here A_2 is calculated with the method in which X_3 from ZST03 is required for a good resolution of 0.6 mass unit (refer to chapter 4.1.3). The strong contribution at $A_2 = A_1 = 28$ with Pb is due to both Coulomb and nuclear excitation (top); while with C the major contribution to $A_2 = A_1$ is only nuclear excitation, therefore the relative intensity of $A_2 = 28$ is much smaller (bottom). With the assumption that the nuclear processes in Pb result in a similar A_2 distribution as in C, the Coulomb excitation contribution to $A_2=28$ in the top spectrum can be estimated by subtracting a A_2 distribution which is obtained by down-scaling the bottom spectrum in such a way that the intensities at $A_2=27$, 26 and 25 are approximately the same as those in the

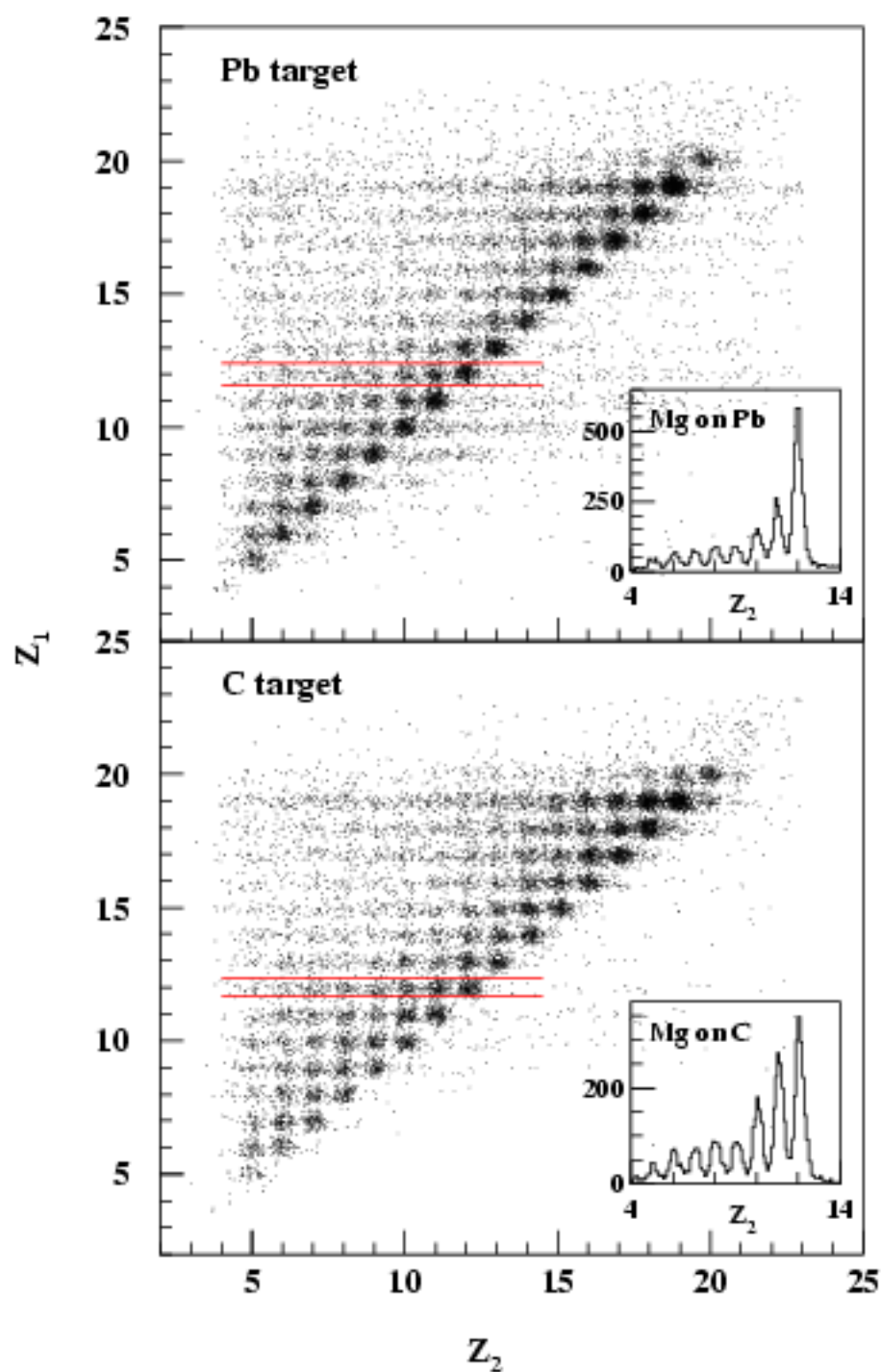


Figure 35: The Z_2 vs. Z_1 distribution of the RIB on the Pb (top) and C target (bottom) with a condition of $M_\gamma > 0$ and $E_\gamma > 1000$ keV. The inlay pictures show the Z_2 distribution for the incoming Mg isotopes ($Z_1 = 12$). See text for details.

top spectrum. The ratio of the Coulomb and nuclear excitation strength in Pb is roughly derived as 2 : 1, which is consistent with the theoretical calculation (see table 1 in chapter 2.2).

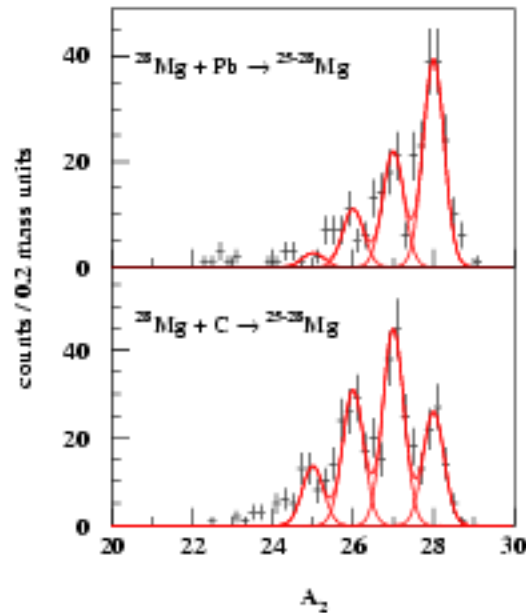


Figure 36: The A_2 distributions after reactions of ^{28}Mg with the Pb (top) and C target (bottom), with $Z_2 = Z_1 = 12$, $A_1 = 28$, $M_\gamma > 0$ and $E_\gamma > 1000$ keV required. The relative intensity at $A_2 = 28$ is much larger with a Pb- than with a C target because of strong Coulomb excitation by Pb.

From this experiment, all the neutron-rich nuclei ranging from beryllium ($Z=4$) to calcium ($Z=20$) with $A/Z=2.1-2.5$ can be studied systematically by setting cuts on A_1 and Z_1 (refer to fig. 19 in chapter 4.1.3). As examples, the incoming isotopes of the Mg- and Ar-chain, representing the light and heavy nuclei respectively, will be discussed.

In the first place, fragmentation reactions of ^{28}Mg and ^{43}Ar with the C target will be considered in order to present an overview of the reaction products (chapter 5.1). Fragmentation with the Pb target is not discussed because of low statistics.

After that, the γ -spectroscopy of the RIB with both the Pb and C targets will be investigated.

With Coulomb excitation low-lying low-spin states and giant resonances can be reached. In the former case, only γ -rays are emitted; whereas in the latter case, the “hot” nuclei de-excite first by neutron evaporation and then by γ -ray emission, which originate from excited states of the neighbouring isotopes. In addition, few nucleon removal reactions with C are employed to investigate higher lying states of the neighbouring nuclei.

The γ -spectra from reactions of $^{27,28}\text{Mg}$ (chapter 5.2) and $^{42,43,44}\text{Ar}$ (chapter 5.3) with Pb and C will be discussed. $Z_2 = Z_1$ is required to limit the reactions to inelastic excitation and neutron removal reaction channels. The cut on A_2 is not always applied for γ -spectra, depending on statistics and necessity. In chapter 5.4, the cross section of inelastic excitation will be given and compared with some calculations.

5.1 Fragmentation reactions of ^{28}Mg and ^{43}Ar with the C target

Gating on $Z_1 = 12$, $A_1 = 28$ and $Z_1 = 18$, $A_1 = 43$ respectively, cross sections of fragmentation reactions of ^{28}Mg and ^{43}Ar on the C target with an incident energy of 238.7 A MeV and 222.2 A MeV, are derived experimentally and compared to empirical calculations.

5.1.1 Charge-changing cross section $\sigma(\Delta Z)$

The charge distributions after the reactions of ^{28}Mg and ^{43}Ar with the C target are shown in fig. 37 (top). The fragment yield $N_{frag}(\Delta Z)$ ($\Delta Z = Z_2 - Z_1$ is the charge loss) can be obtained directly from the spectra. The experimental charge-changing cross sections are calculated as follows (refer to chapter 4.4)

$$\sigma_{exp}(\Delta Z) = \frac{N_{frag}(Z_2)/\varepsilon_{PIN2}(\Delta A)}{N_{proj} \times \rho}, \quad (48)$$

where ε_{PIN2} is the relative acceptance of PIN02 related to mass loss $\Delta A = A_2 - A_1$ (see table 5 in chapter 4.2.2). In order to obtain ε_{PIN2} for each ΔZ , the mean value of mass loss is approximately taken as $\langle \Delta A \rangle = 3\Delta Z$ (refer to fig. 38). The values of σ_{exp} are plotted in fig. 37 (bottom) and listed in table 7, with the uncertainty originating mainly from the statistical uncertainty of the fragment yield.

For heavy projectile nuclei interacting with a heavy target, the charge-changing cross sections are empirically described by power laws in $|\Delta Z|$ [Bin87,Cum90]:

$$\sigma(\Delta Z) = \sigma_e |\Delta Z|^{-\epsilon}, \quad (49)$$

with the scaling σ_e and the power ϵ depending on the mass of the target and the projectile A_t and A_1 as well as the beam energy E_{beam} . As shown by the dashed line in fig. 37, the power laws fit our experimental data quite well.

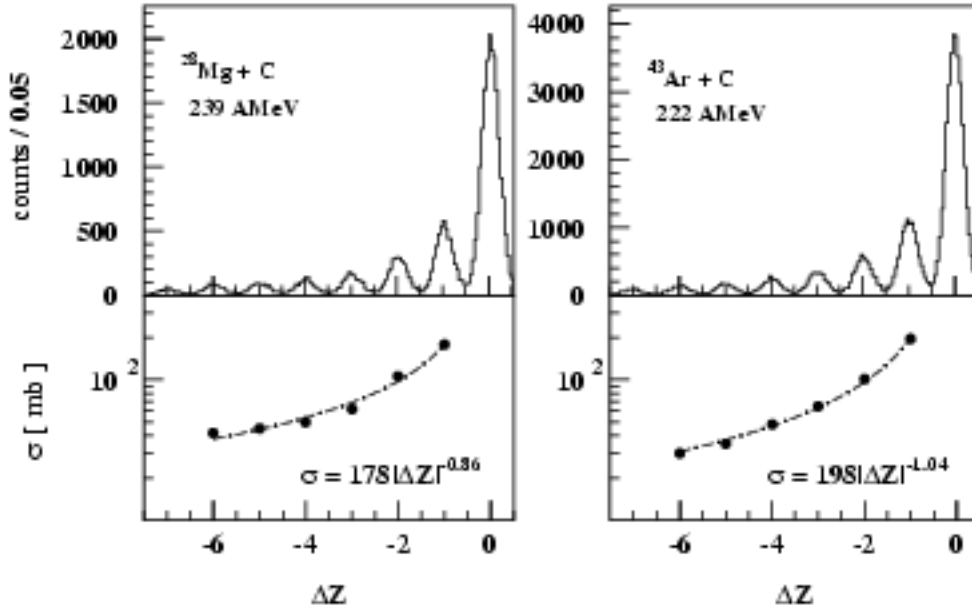


Figure 37: top: Charge distribution after the reactions of ^{28}Mg and ^{43}Ar on the C target. In the $\Delta Z = Z_2 - Z_1 = 0$ peak, there is contribution from atomic background because no condition on the CB is required. bottom: Experimental charge-changing cross sections $\sigma(\Delta Z)$ (points) are fitted by a function of $\sigma(\Delta Z) = \sigma_c |\Delta Z|^{-\epsilon}$ (dashed line).

Table 7: Experimental charge-changing cross sections derived from formula (48), with the number of ^{28}Mg and ^{43}Ar projectiles being obtained under the condition of $Z_1 = Z_2 = 12$, $A_1 = 28$ and $Z_1 = Z_2 = 18$, $A_1 = 43$ as $N_{proj} = 1.11 \times 10^6$ and 2.06×10^6 respectively.

$^{28}\text{Mg}+\text{C}@239\text{ AMeV}$			$^{43}\text{Ar}+\text{C}@222\text{ AMeV}$		
ΔZ	N_{frag}	σ_{exp} (mb)	ΔZ	N_{frag}	σ_{exp} (mb)
-1	5079	177.5 ± 2.4	-1	10640	194.7 ± 1.9
-2	2885	106.3 ± 1.8	-2	5402	100.6 ± 1.4
-3	1580	62.3 ± 1.3	-3	3397	64.9 ± 1.0
-4	1181	50.4 ± 1.1	-4	2458	48.1 ± 0.9
-5	964	45.4 ± 1.0	-5	1719	34.7 ± 0.7
-6	838	40.2 ± 1.0	-6	1437	30.0 ± 0.7

5.1.2 Isotopic cross section $\sigma(Z_2, A_2)$

With the condition $Z_2=12, 11$ and 10 , the mass distributions of Mg, Na and Ne after the reaction of ^{28}Mg with the C target are shown in fig. 38 (left). In the same way, A_2 distributions of S, P and Si after the reaction of ^{43}Ar with the C target are shown in the right panels in the same figure. As a reference, the two top spectra show the A_2 distribution of the beam obtained with the beam trigger which means no reaction but only atomic straggling takes place (refer to chapter 3.3.2). Here A_2 is calculated with the method in which X_3 from ZST03 is required to achieve a resolution as good as possible (refer to chapter 4.1.3). From these spectra, the yield of each isotope $N_{frag}(Z_2, A_2)$ is obtained (see table 8).

The experimental isotopic cross section is calculated as follows:

$$\sigma_{exp}(Z_2, A_2) = \frac{N_{frag}(Z_2, A_2)/\varepsilon_{PIN2}(\Delta A)/\varepsilon_{A_2}(Z_2)}{N_{proj}/\varepsilon_{A_2}(Z_1) \times \rho}, \quad (50)$$

where ε_{A_2} is the efficiency to determine A_2 which depends strongly on Z (refer to table 4 in chapter 4.1.3). The main contribution to the uncertainty of σ_{exp} is of statistical nature.

In the computer code EPAX [Süm90], the isotopic cross section is calculated empirically as

$$\begin{aligned} \sigma(Z_2, A_2) &= X(A_2)Y(Z_2), \\ X(A_2) &= \sigma_T P e^{-P(A_1 - A_2)}, \\ Y(Z_2) &= \sqrt{R/\pi} e^{-R|Z_0 - Z_2|^U}. \end{aligned} \quad (51)$$

The first term $X(A_2)$ represents the mass yield, i.e. the sum of the isobaric cross sections of mass A_2 , with the scale given by the total cross section σ_T which is proportional to the sum of two colliding nuclear radii and the shape governed by the slope parameter which depends on A_1 . The second term $Y(Z_2)$ describes the charge dispersion, namely the distribution of elemental cross sections with a given mass A_1 . The integral of $Y(Z_2)$ is normalized to 1 with the factor $\sqrt{R/\pi}$ where R is the width of the distribution related to A_1 . The peak position of the distribution, i.e. the most likely charge Z_0 , depends mainly on the β -stable charge $Z_\beta(A_2)$ and tends to be at the neutron-deficient side of $Z_\beta(A_2)$ because of evaporation processes. In addition, Z_0 is also affected by the A_1/Z_1 ratio of the projectile (refer to [Süm90] for details). The exponent parameter U is 2 for $Z_2 > Z_0$ and 1.5 for $Z_2 \leq Z_0$.

The experimental and calculated isotopic cross sections are illustrated in fig. 39 and listed in table 8. The calculated data fit the experimental ones better for fragments from the ^{43}Ar projectile (fig. 39: right) than from the ^{28}Mg projectile (left). The reason might be that the EPAX formula is a parametrization for fragments from nuclei heavier than $A_1 \approx 40$. The experimental data deduced here enable to modify the parametrization for a new systematics

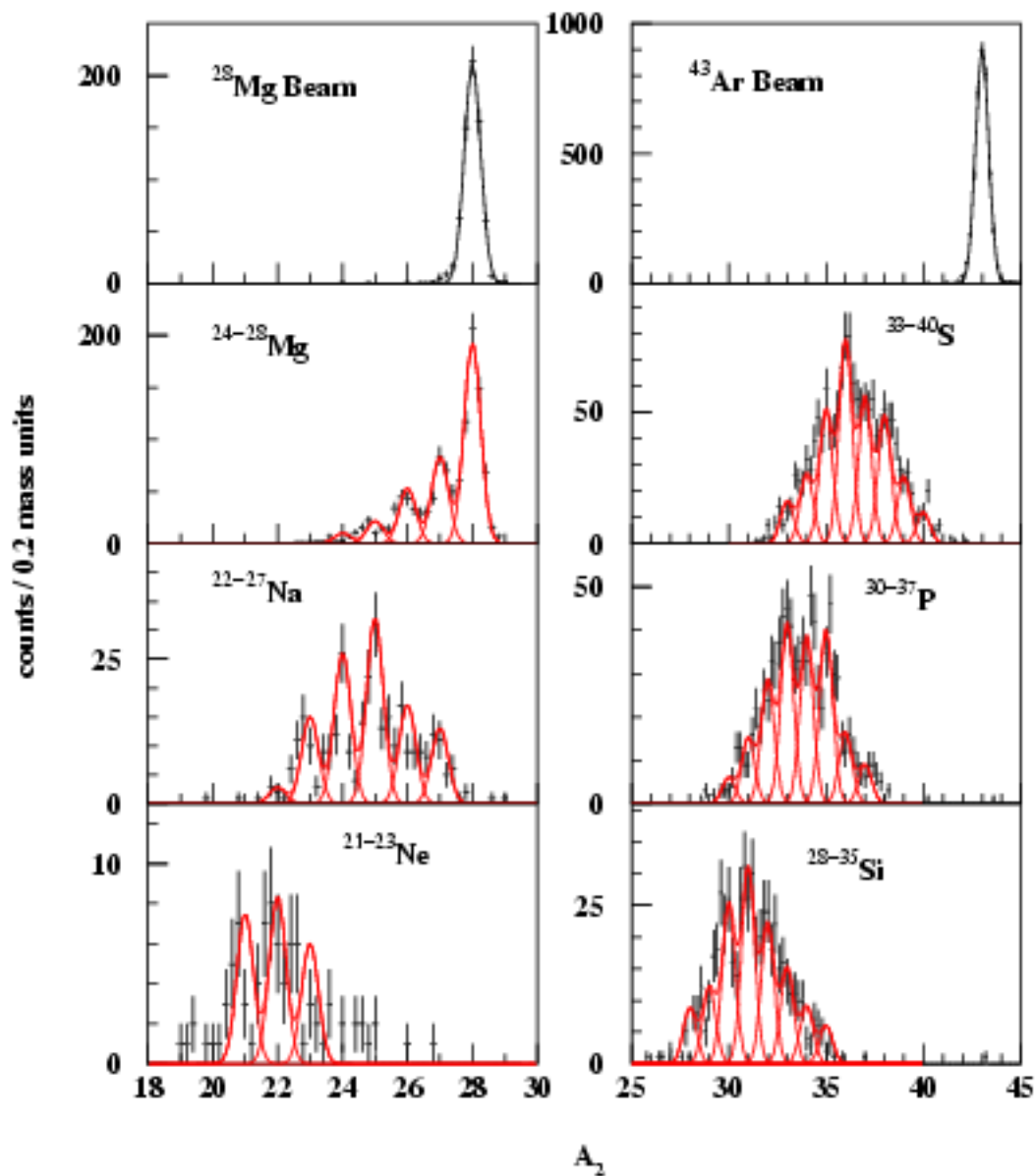


Figure 38: Fragment production after the reaction of ^{28}Mg (left) and ^{43}Ar (right) with the C target. The A_2 resolution of the ^{28}Mg and ^{43}Ar beam which is obtained from the top spectra respectively as 0.6 and 0.8 mass units, is used to fit the fragment distribution.

Table 8: Experimental and calculated isotopic cross sections $\sigma_{exp}(Z_2, A_2)$ and $\sigma_{EPAX}(Z_2, A_2)$ (in mb). To derive $\sigma_{exp}(Z_2, A_2)$ from formula (50), the number of ^{28}Mg and ^{43}Ar projectiles $N_{proj}=1.25\times 10^5$ and 5.89×10^5 is obtained under the condition of $Z_1=Z_2=12$, $A_1=A_2=28$ and $Z_1=Z_2=18$, $A_1=A_2=43$ respectively.

$^{28}\text{Mg}+\text{C}@239\text{ A MeV}$				$^{43}\text{Ar}+\text{C}@222\text{ A MeV}$			
fragment	N_{frag}	σ_{exp}	σ_{EPAX}	fragment	N_{frag}	σ_{exp}	σ_{EPAX}
^{27}Mg	278	83.5 ± 5.0	33.2	^{40}S	57	4.1 ± 0.6	2.1
^{26}Mg	184	56.1 ± 4.1	18.8	^{39}S	136	9.9 ± 0.9	5.1
^{25}Mg	66	20.5 ± 2.5	7.3	^{38}S	229	16.8 ± 1.1	10.7
^{24}Mg	16	5.1 ± 1.3	1.7	^{37}S	267	19.7 ± 1.2	19.1
				^{36}S	337	25.2 ± 1.4	25.2
				^{35}S	233	17.5 ± 1.4	18.3
				^{34}S	146	11.1 ± 0.9	8.1
^{27}Na	42	21.0 ± 3.2	11.2	^{37}P	36	2.8 ± 0.5	1.9
^{26}Na	54	27.5 ± 3.7	22.8	^{36}P	56	4.4 ± 0.6	4.9
^{25}Na	95	49.3 ± 5.1	30.4	^{35}P	155	12.2 ± 1.0	10.8
^{24}Na	65	34.1 ± 4.2	26.3	^{34}P	187	14.8 ± 1.1	19.0
^{23}Na	45	24.1 ± 3.6	13.7	^{33}P	197	15.8 ± 1.1	20.8
^{22}Na	7	3.8 ± 1.4	4.0				
^{23}Ne	18	19.3 ± 4.5	20.9	^{35}Si	23	2.1 ± 0.4	0.7
^{22}Ne	29	31.7 ± 5.9	26.0	^{34}Si	38	3.5 ± 0.6	2.2
^{21}Ne	19	21.1 ± 4.8	18.3	^{33}Si	77	7.2 ± 0.8	5.6
				^{32}Si	105	9.9 ± 1.0	12.1
				^{31}Si	127	12.0 ± 1.1	19.1
				^{30}Si	109	10.4 ± 1.0	15.1
				^{29}Si	34	3.3 ± 0.6	6.6

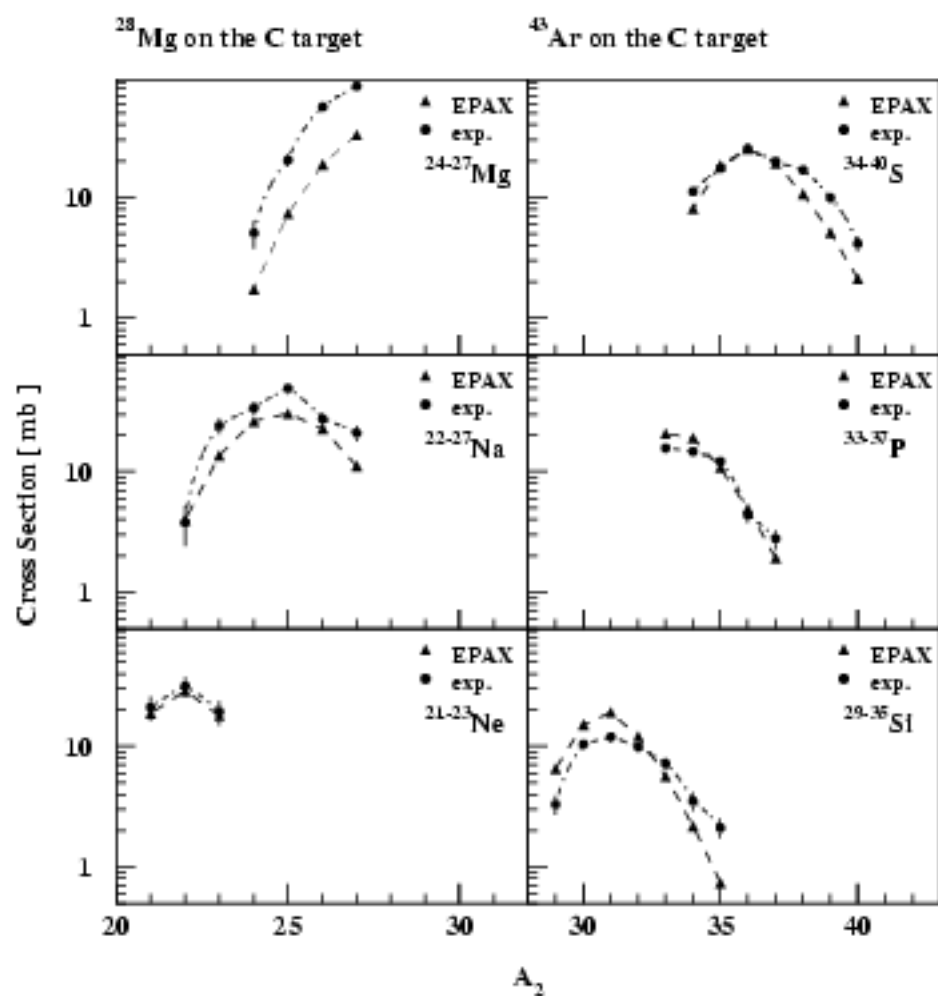


Figure 39: Isotopic cross section $\sigma(Z_2, A_2)$ evaluated from experimental data and calculated with EPAX.

for masses of $20 \sim 45$ and energies of $200 \sim 300$ A MeV.

5.2 Spectroscopic results for the Mg-isotopes

Gamma-spectroscopy of two isotopes $^{27,28}\text{Mg}$ with a cut $Z_1 = Z_2 = 12$, $A_1 = 27, 28$ is discussed. With the Pb target, γ -spectra are obtained without any condition on A_2 because the major part of reactions is inelastic excitation which does not change mass number (see fig. 36: top). However, A_2 information is used to check the origin of the γ -peaks. With the C target, on the other hand, conditions on A_2 are necessary for γ -spectroscopy because nuclear removal reactions are strong and a significant fraction of particles do change their mass number (see fig. 36: bottom). In order to get reasonable statistics, A_2 is calculated with the method in which the tracking detector ZST03 is not necessarily required, resulting in a resolution of ~ 0.8 mass units and an efficiency of $\sim 55\%$ (see chapters 4.1.2 and 4.1.3).

The atomic background is severe in the γ -spectra from the excitation with the Pb target (especially with γ -multiplicity $M_\gamma = 1$) while negligibly small with the C target as it depends strongly on the particle and target charges. As shown in fig. 8 in chapter 3.1.3, the cross section of atomic background in C is two magnitudes lower than that in Pb.

5.2.1 Excitation of $^{27,28}\text{Mg}$ with the Pb target

The γ -spectra and A_2 distributions of the even-even incoming isotope ^{28}Mg on the Pb target are shown in fig. 40. By requiring the trigger " γ " and $M_\gamma = 1$, besides the huge atomic background at low energies, the γ -line corresponding to the first excited state of ^{28}Mg shows up at 1473 keV (a) (refer to the known level scheme at the bottom). Gating on this γ -line, we get a distribution dominating at $A_2 = 28$ (d). It is consistent with that of the beam in (c) which is obtained with the beam trigger. Beam trigger means no reaction but only atomic straggling takes place (see chapter 3.3.2).

If one or several γ s and at least one neutron are required, we can investigate the "hot" channels, i.e. ^{28}Mg excited to giant resonances and then decaying by neutron evaporation resulting in excited states in its neighbouring isotopes such as ^{27}Mg and ^{26}Mg , which de-excite further by emitting γ -rays. By requiring the trigger " $\gamma+n$ " and $M_\gamma = 1-3$, two peaks around 1000 keV and 1700 keV appear (b). Gating on these two peaks respectively, A_2 distributions (e) and (f) composed of two peaks at $A_2 = 26$ and 27 are obtained. Referring to the known level schemes, these two peaks are suggested to originate from transitions in ^{26}Mg and ^{27}Mg . The 1000 keV peak is related to $5/2_2^+ \rightarrow 3/2^+ \rightarrow 1/2^+$ in ^{27}Mg and $2_2^+ \rightarrow 2_1^+$ in ^{26}Mg , whereas the 1700 keV peak is associated with $5/2_2^+, 5/2_1^+ \rightarrow 1/2^+$ in ^{27}Mg and $2_1^+ \rightarrow 0^+$ in ^{26}Mg . Because of the resolution of the CB, the γ -lines with energies

near to each other can not be distinguished. In (f) the peak at $A_2 = 26$ is stronger than $A_2 = 27$ because the excitation strength in the odd- A isotope is fragmented into several states.

The γ -spectra and A_2 distributions of the incoming isotope ^{27}Mg on the Pb target are shown in fig. 41, from which γ -transitions in ^{27}Mg as well as its neighbouring isotopes can be seen by gating on different trigger and M_γ .

5.2.2 Reactions of $^{27,28}\text{Mg}$ with the C target

The γ -spectra of ^{28}Mg impinging on the C target are displayed in fig 42. Gating on $A_2 = 28, 27$ and 26 , γ -spectroscopy for different reaction channels, namely inelastic excitation $^{28}\text{Mg} + \text{C} \rightarrow ^{28}\text{Mg}^*$, neutron removal reactions $^{28}\text{Mg} + \text{C} \rightarrow ^{27}\text{Mg}^* + 1n$ and $^{28}\text{Mg} + \text{C} \rightarrow ^{26}\text{Mg}^* + 2n$ can be investigated. Comparing the three E_γ vs. M_γ spectra with different A_2 cuts (top), we see that the γ -multiplicity M_γ distribution is shifted to higher values as the reaction becomes more violent. Projecting these spectra on E_γ with a proper cut on M_γ , γ -peaks originating from $^{28,27,26}\text{Mg}$ show up respectively (middle). The known level schemes are plotted at the bottom for reference.

Fig. 43 displays the γ -spectra from the reaction of ^{27}Mg with C, gating on $A_2 = 27$ and 26 . After inelastic excitation $^{27}\text{Mg} + \text{C} \rightarrow ^{27}\text{Mg}^*$ and one neutron removal reaction $^{27}\text{Mg} + \text{C} \rightarrow ^{26}\text{Mg}^* + 1n$, γ -peaks associated with transitions in ^{27}Mg and ^{26}Mg can be seen.

To confirm that the two γ -peaks observed in the $^{27}\text{Mg} + \text{C} \rightarrow ^{26}\text{Mg}^* + 1n$ reaction are from the $2_2^+(2930) \rightarrow 2_1^+(1808) \rightarrow 0^+(0)$ γ -cascade in ^{26}Mg (fig. 44: top-right), the sum energy E_{sum} vs. M_γ spectrum is investigated (top-left). With $M_\gamma=1$, distribution around 1800 keV corresponding to the first excited 2_1^+ state is dominant; with $M_\gamma=2$, a structure at $E_{\text{sum}} \approx 3000$ keV related to the second excited 2_2^+ state can be seen. Gating on $M_\gamma=2$ to plot a γ - γ coincidence matrix (bottom-left), we see a strong distribution at 1130 and 1800 keV. By setting an energy window around 1808 keV to one γ and projecting the other, a peak at 1130 keV shows up clearly (bottom-right). Another peak at 1780 keV in the same spectrum might be related to another γ -cascade $0_2^+(3588) \rightarrow 2_1^+(1808) \rightarrow 0^+(0)$ in ^{26}Mg . This demonstrates, despite the moderate energy resolution, detailed spectroscopy with the CB is possible.

The cross section of inelastic excitation with Pb should be much larger than that with C because of strong Coulomb excitation in Pb. As there were about 10 times more nuclei per unit area in the C target than in the Pb target (refer to chapter 4.4), the yields of γ -peaks corresponding to inelastic excitation with both targets are comparable.

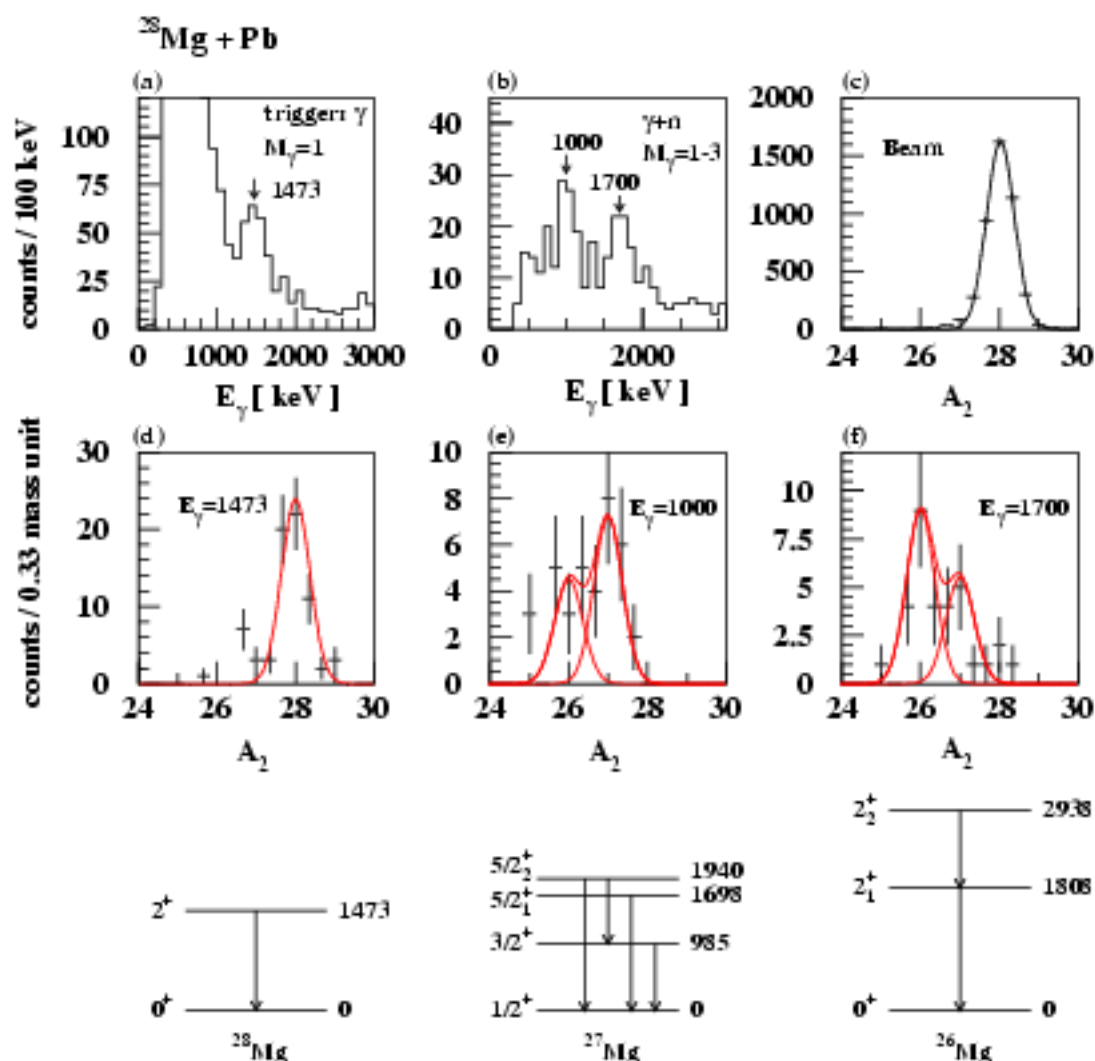


Figure 40: Gamma-spectra and A_2 distributions of ^{28}Mg impinging on Pb . The known level schemes are displayed at the bottom for reference with energies given in keV. (a): With the trigger “ γ ” and $M_\gamma = 1$, the γ -line corresponding to the $2^+ \rightarrow 0^+$ transition in ^{28}Mg shows up. (d): The A_2 distribution gating on this γ -line peaks at $A_2=28$. (b): With the trigger “ $\gamma+n$ ” and $M_\gamma = 1-3$, two γ -peaks appear. (e) and (f): The A_2 distributions gating on these two γ -lines peak at $A_2=27$ and 26 . This evidences that the γ -peaks originate from the γ -transitions in the neighbouring isotopes $^{26,27}\text{Mg}$. (c): The A_2 distribution of the ^{28}Mg beam.

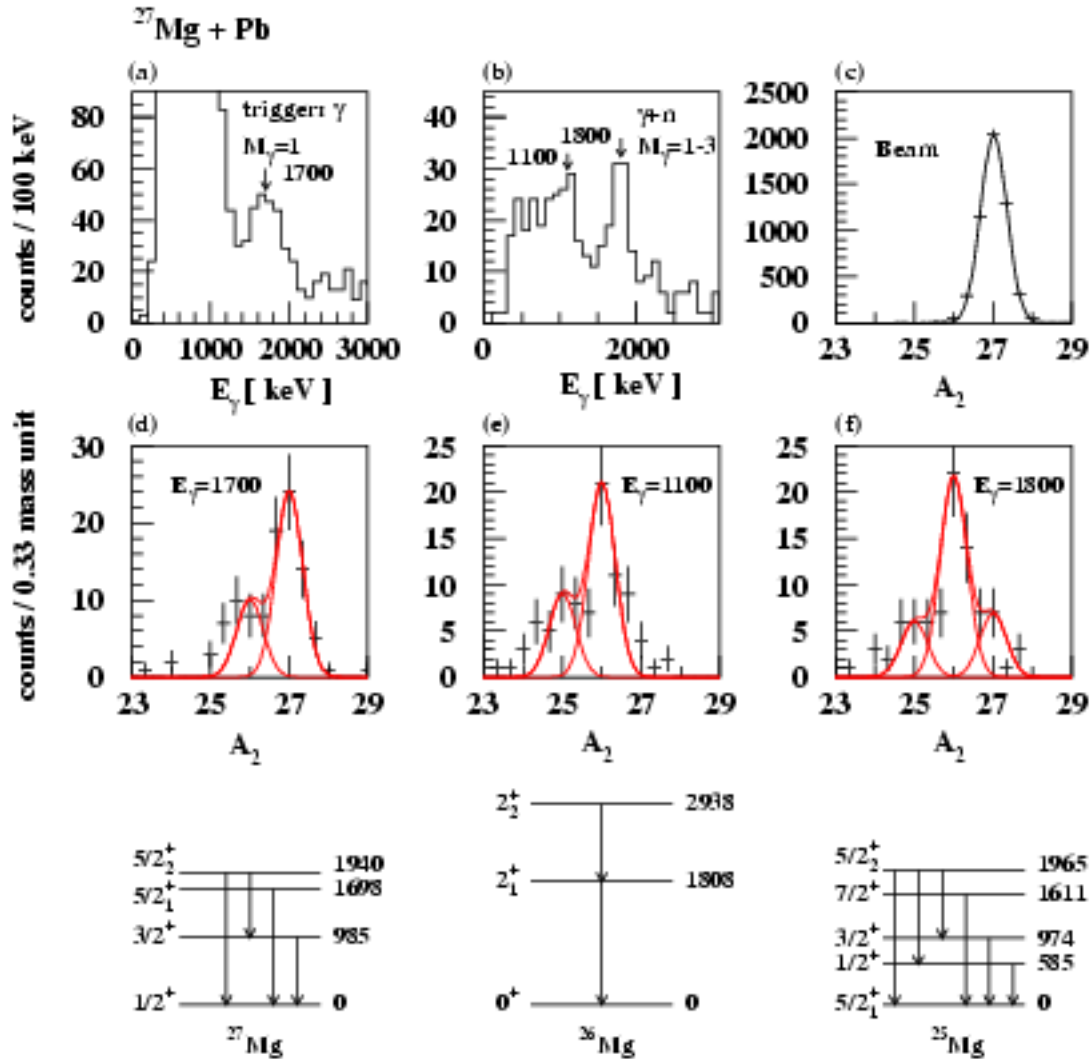


Figure 41: Gamma-spectra and A_2 distributions of ^{27}Mg impinging on Pb. The known level schemes are displayed at the bottom for reference with energies given in keV. (a): With the trigger “ γ ” and $M_\gamma = 1$, we see a γ -peak which might be a mixture of the transitions from $5/2_2^+$ and $5/2_1^+$ to $1/2^+$ in ^{27}Mg . (d): The strong distribution at $A_2=27$ in the A_2 spectrum gating on this γ -peak verifies its origin. The smaller distribution around $A_2 = 26$ can be explained by a contamination from the 1808 keV transition in ^{26}Mg . (b): With the trigger “ $\gamma+n$ ” and $M_\gamma = 1-3$, two peaks appear. (e) and (f): The A_2 distribution of the two peaks suggests that, the peaks originate mainly from the γ -cascade in ^{26}Mg and contaminate contribution from transitions in ^{25}Mg and/or ^{27}Mg . (c): The A_2 distribution of the ^{27}Mg beam.

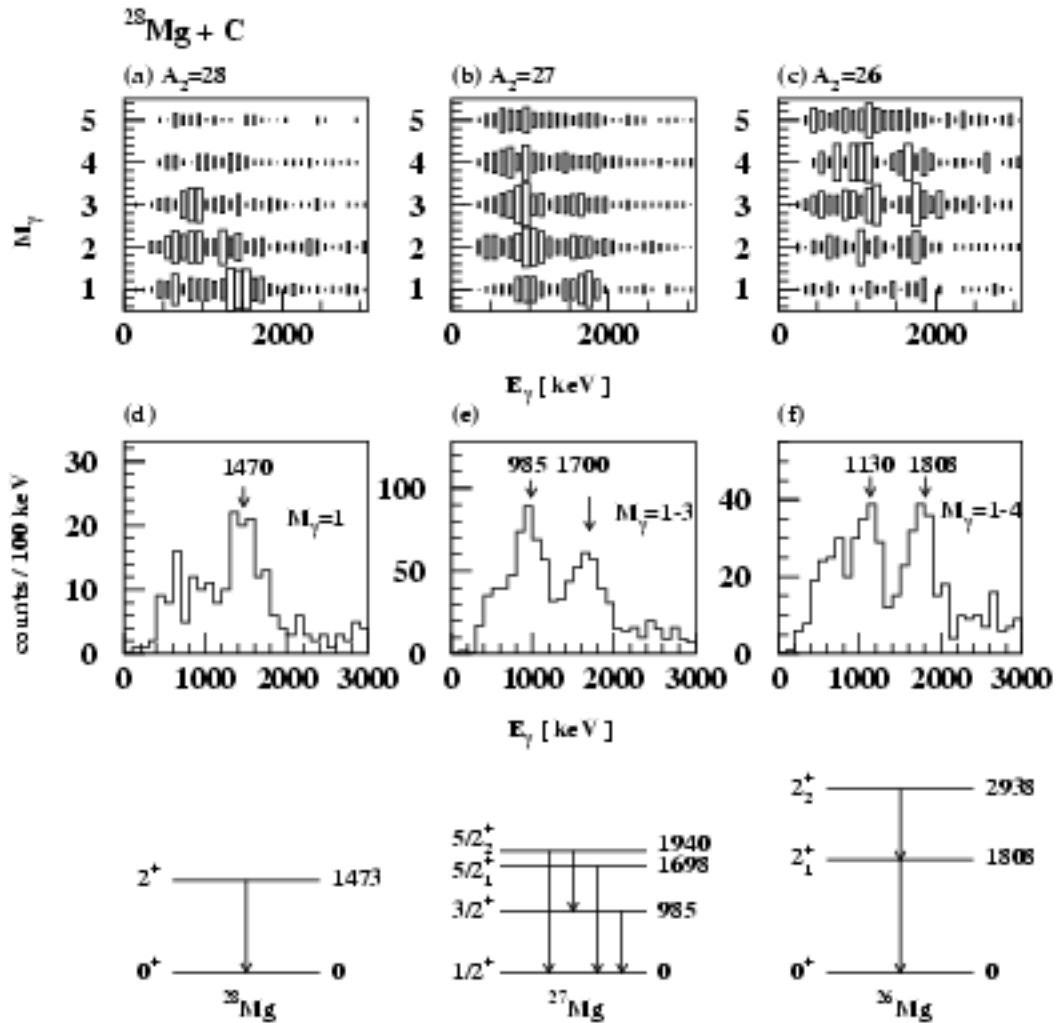


Figure 42: The γ -spectra of ^{28}Mg impinging on C. (top): E_γ vs. M_γ spectra gating on $A_2=28$, 27 and 26. The M_γ distribution is shifted to higher values as the reaction becomes more violent. (middle): Energy spectrum projected from the corresponding spectra in the top panels with a proper cut on M_γ . (d): With $A_2=28$ and $M_\gamma = 1$, a γ -line corresponding to the decay of the first excited state $2^+(1470)$ in ^{28}Mg can be seen; (e): with $A_2=27$ and $M_\gamma = 1-3$, two peaks are observed representing the $3/2^+ \rightarrow 1/2^+$ and $5/2_2^+, 5/2_1^+ \rightarrow 1/2^+$ transitions in ^{27}Mg ; (f): with $A_2=26$ and $M_\gamma = 1-4$, two γ -lines associated with the γ -cascade $2_2^+ \rightarrow 2_1^+ \rightarrow 0^+$ in ^{26}Mg appear. (bottom): The known level schemes for reference.

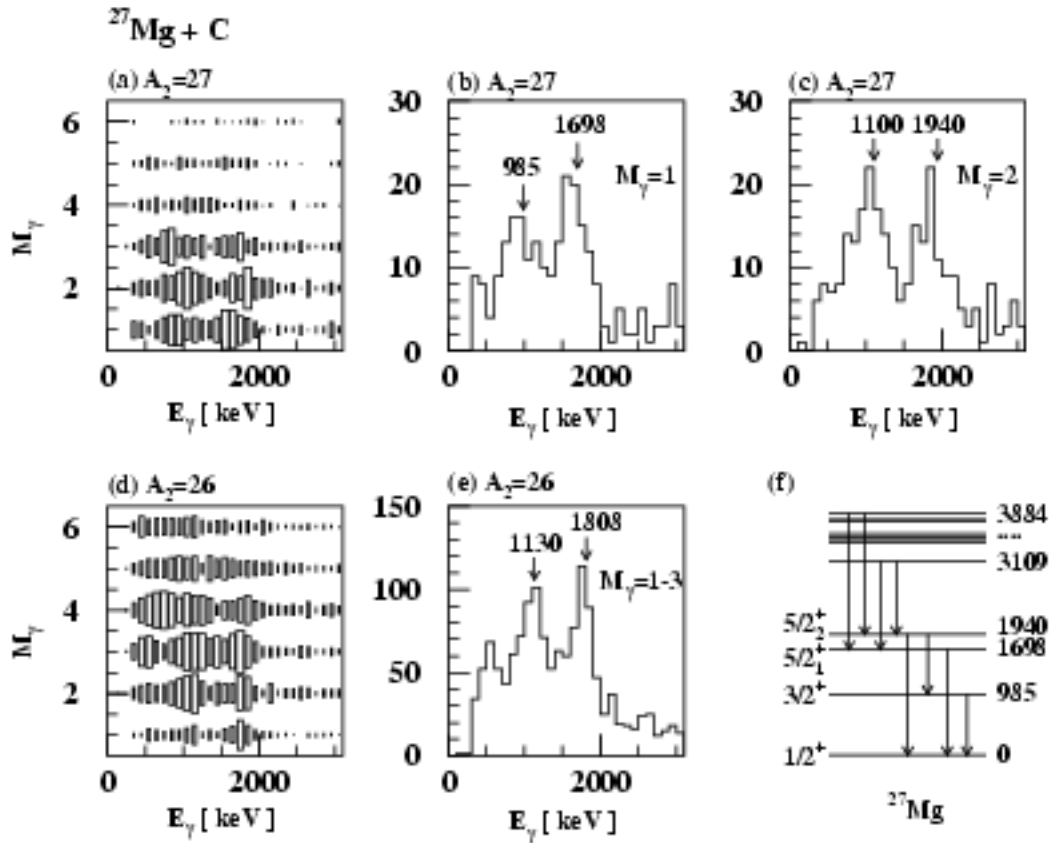


Figure 43: The γ -spectra of ^{27}Mg impinging on C. (a) and (d): E_γ vs. M_γ spectra with a cut on $A_2=27$ and 26. The M_γ distribution with $A_2=26$ exhibits higher values than $A_2=27$ because it reflects more violent reactions. (b): The projection of (a) with $M_\gamma=1$ has two γ -peaks corresponding to the decay of the first excited $3/2^+$ and $5/2_1^+$ states of ^{27}Mg . (c): The projection of (a) with $M_\gamma=2$ shows two other peaks at slightly higher energies which may originate from a γ -cascade of higher states of ^{27}Mg , i.e. $(3109) \rightarrow 5/2_2^+(1940) \rightarrow 1/2^+(0)$ (refer to the known level scheme of ^{27}Mg (f)), another cascade $5/2_2^+ \rightarrow 3/2_1^+ \rightarrow 1/2^+$ with $E_{\gamma 1} \approx E_{\gamma 2} \approx 1000$ keV might be covered by the γ -peak at 1100 keV). (e): The projection of (d) with $M_\gamma=1-3$ displays two peaks from the γ -cascade in ^{26}Mg .

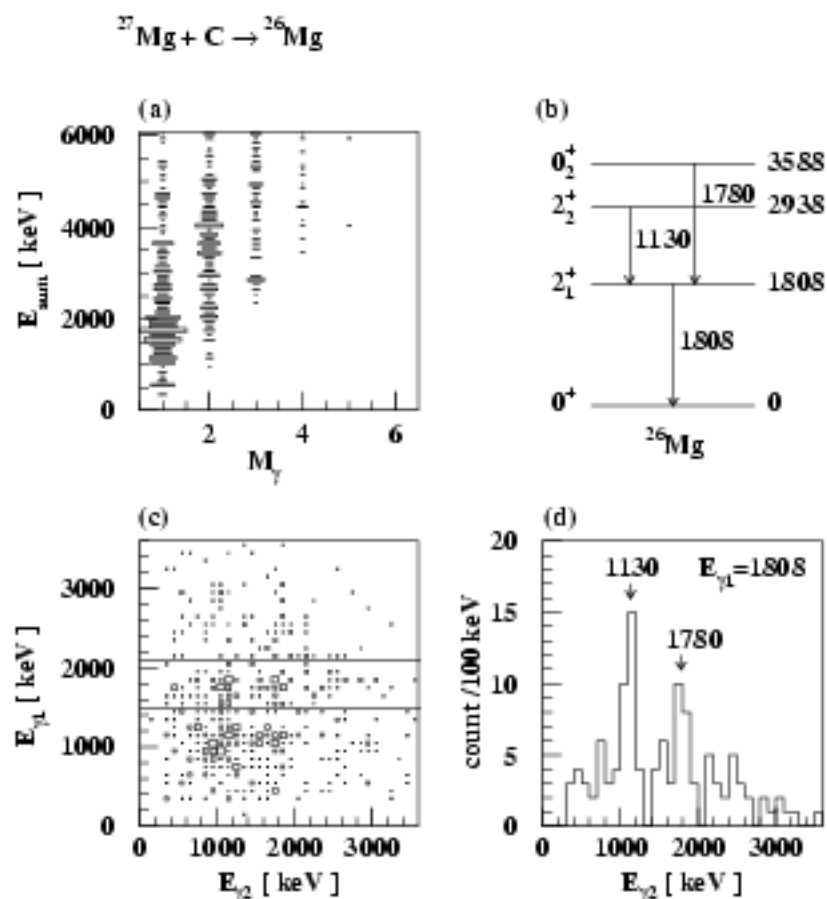


Figure 44: The decay sequences of ^{26}Mg (b) suggested from the $^{27}\text{Mg} + \text{C} \rightarrow ^{26}\text{Mg}$ spectrum in fig. 43(e) can be confirmed by: (a) the sum energy E_{sum} vs. M_γ spectrum, which shows a dominant distribution at $M_\gamma = 1$, $E_{sum} \approx 1800$ keV and $M_\gamma = 2$, $E_{sum} \approx 3000$ and 3500 keV, (c) the γ - γ matrix with $M_\gamma = 2$. (d) By setting an energy window around 1808 keV to one γ in (c) and projecting the other, peaks at 1130 keV and 1780 keV show up clearly.

5.3 Spectroscopic results for the Ar-isotopes

Spectra from reactions of the incoming isotopes ^{42}Ar , ^{43}Ar and ^{44}Ar with the Pb and C target will be discussed in the following three sub-chapters 5.3.1 - 5.3.3. A cut on A_2 , which is derived with a resolution of $0.8\sim 0.9$ mass units and an efficiency of $30\sim 40\%$, is helpful in the analysis, e.g. to investigate the γ -cascade of ^{42}Ar produced by the reactions $^{43}\text{Ar}+\text{Pb}$ and $^{43}\text{Ar}+\text{C}$.

5.3.1 ^{42}Ar with the Pb and C target

The γ -spectra from the reactions of ^{42}Ar with the Pb and C target are shown in fig. 45 with conditions on the γ -trigger, M_γ and/or A_2 . In both spectra we see a peak at 1200 keV which could be related to the first excited state $2_1^+(1208)$ or the γ -cascade $2_2^+(2487)\rightarrow 2_1^+(1208)\rightarrow 0^+(0)$ of ^{42}Ar .

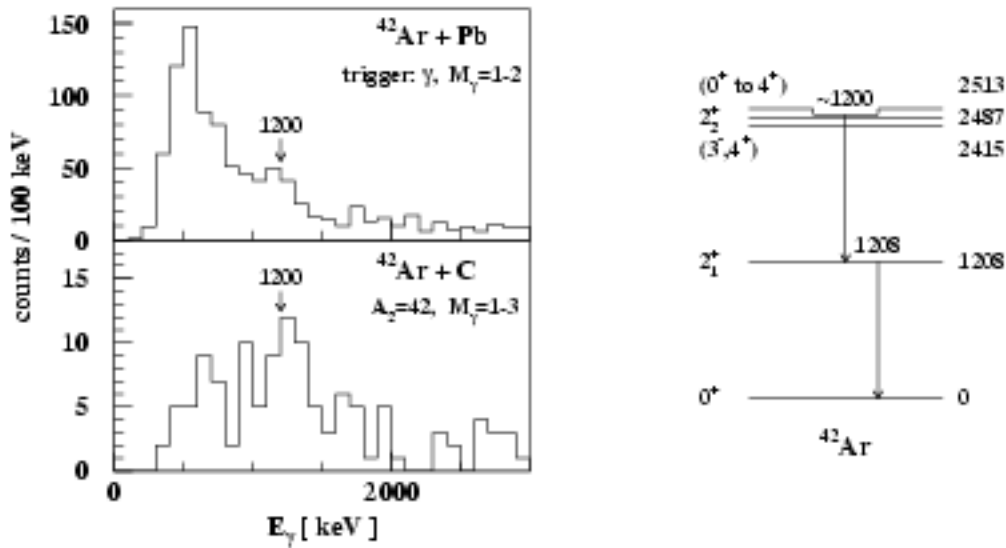


Figure 45: The γ -spectra of ^{42}Ar . From excitation of ^{42}Ar with the Pb target, requiring the γ -trigger and $M_\gamma=1-2$, a peak shows up at around 1200 keV above the large atomic background (top); from the reaction of ^{42}Ar with the C target, gating on $A_2 = 42$ and $M_\gamma=1-3$, we also get a peak at 1200 keV (bottom). Comparing with the known level scheme (right), this γ -peak is supposed to be related to the first excited state $2_1^+(1208)$ or the γ -cascade $2_2^+(2487)\rightarrow 2_1^+(1208)\rightarrow 0^+(0)$ of ^{42}Ar .

5.3.2 ^{43}Ar with the Pb and C target

The γ -spectra from the reaction of ^{43}Ar with the Pb target are shown in fig. 46 (left). Requiring a γ -multiplicity $M_\gamma=2-4$ ($M_\gamma=1$ is excluded because of the large atomic background), a peak around 1200 keV shows up (top), which could be related to γ -transitions in ^{42}Ar . If $A_2=42$ is required, i.e. gating on the $^{43}\text{Ar}+\text{Pb}\rightarrow^{42}\text{Ar}^*+1n$ reaction channel, with $M_\gamma=1-4$, the background is suppressed and the peak is improved (middle). Because of the limited A_2 resolution, the cut on $A_2=42$ is contaminated by $A_2=41$ and especially $A_2=43$ components. If a neutron detected by LAND is also required in addition to $A_2=42$, we get a further improvement (bottom). Therefore this peak can be confirmed to originate from γ -transitions in ^{42}Ar accompanied by neutron emission.

The γ -spectra from the reaction of ^{43}Ar with the C target are also seen in fig. 46 (right). With $M_\gamma=1-4$, a peak shows up at around 1200 keV (top). Similar to the reaction $^{43}\text{Ar}+\text{Pb}$, this peak can be improved by gating on $A_2=42$ (middle). However, requiring neutrons detected by LAND does not further improve the peak significantly (bottom). Moreover, the peak intensity decreases roughly by a factor of 7 (for the reaction with the Pb target, the peak intensity decreases only by a factor of 3 if LAND is required).

Neutron emissions with the Pb and C target are interpreted to be caused by different mechanisms. If a projectile is first excited to giant resonances by Coulomb excitation and then decays by neutron evaporation, the neutrons are emitted with a kinetic energy of a few MeV in the rest system of the projectile. Therefore in the lab system, because of the high beam energy, the evaporated neutrons go to forward direction with a very small opening angle comparable to the acceptance of LAND. On the other hand, if neutrons are knocked out directly during the reaction, the process can be approximately described as a free nucleon-nucleon collision associated with an almost isotropic angular distribution in the C.M. system of the two colliding nucleons. In the lab system, the opening angle of the knocked out neutrons exceeds the acceptance of LAND. With ^{43}Ar on Pb it is more likely to have the first kind of neutron emission, while with ^{43}Ar on C the second mechanism seems to dominate. That is why requiring LAND does not help too much to improve the 1200 keV peak from the $^{43}\text{Ar}+\text{C}\rightarrow^{42}\text{Ar}^*+1n$ reaction.

The sum energy and the γ - γ -coincidence matrix gating on the $^{43}\text{Ar}+\text{Pb}\rightarrow^{42}\text{Ar}^*+1n$ and $^{43}\text{Ar}+\text{C}\rightarrow^{42}\text{Ar}^*+1n$ reaction channel (fig. 47) give evidence that the peak around 1200 keV is composed of two γ -lines from the γ -cascade $2^+(2487)\rightarrow 2^+(1208)\rightarrow 0^+(0)$ of ^{42}Ar . Because of the energy resolution of the CB, these γ -lines which have similar energies can not be distinguished.

By gating on $A_2=41$ and $A_2=40$, the two and three neutron removal reaction channels $^{43}\text{Ar}+\text{C}\rightarrow^{41}\text{Ar}^*+2n$ and $^{43}\text{Ar}+\text{C}\rightarrow^{40}\text{Ar}^*+3n$ can be investigated (fig. 48). The γ -lines

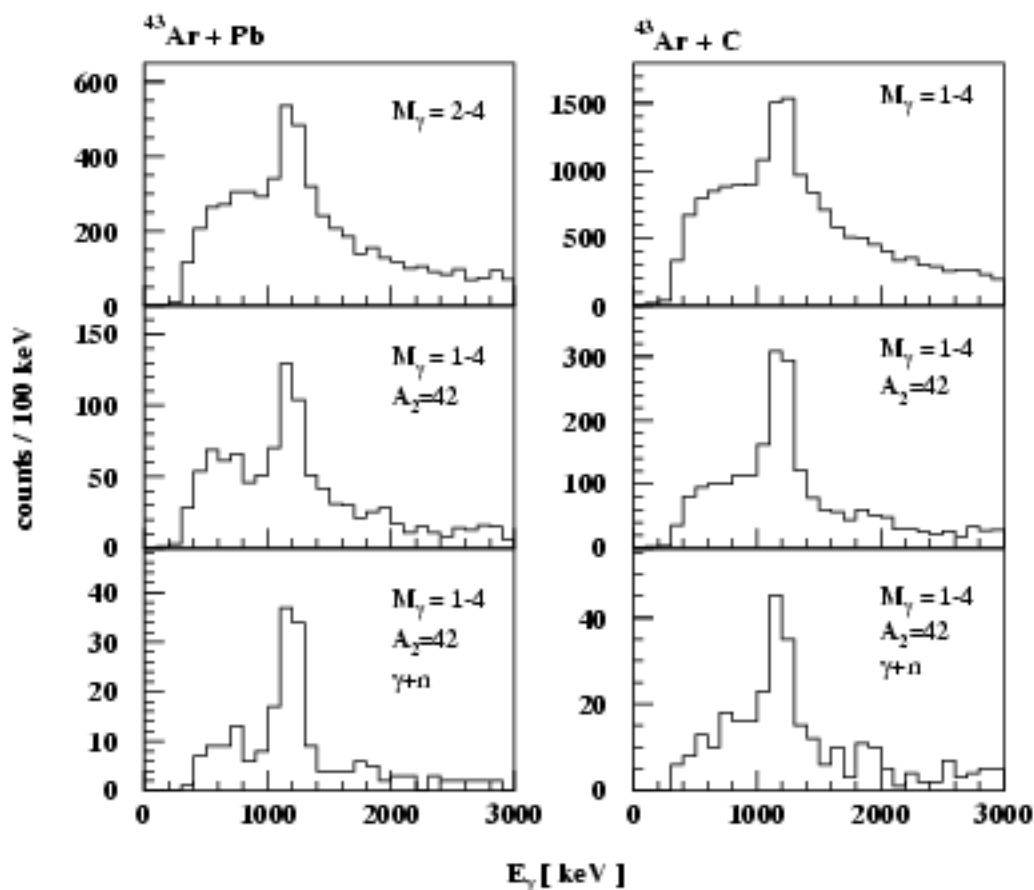


Figure 46: left: The peak around 1200 keV from the reaction of ^{43}Ar with the Pb target (top) is improved step by step by requiring $A_2=42$ (middle) and in addition the trigger “ γ +neutron” (bottom). This confirms that the peak comes from the γ -transitions in ^{42}Ar accompanied by neutron evaporation. right: The 1200 keV γ -peak from the reaction of ^{43}Ar with the C target (top) is improved by requiring $A_2=42$ (middle) but not significantly further improved with the trigger “ γ +neutron” (bottom). By requiring the trigger “ γ +neutron”, the peak intensity decreases by about a factor of 3 and 7 respectively for the $^{43}\text{Ar}+\text{Pb}\rightarrow^{42}\text{Ar}^*+1n$ and $^{43}\text{Ar}+\text{C}\rightarrow^{42}\text{Ar}^*+1n$ reaction. This indicates that neutron emissions with the Pb and C target are caused by different mechanisms. See text for details.

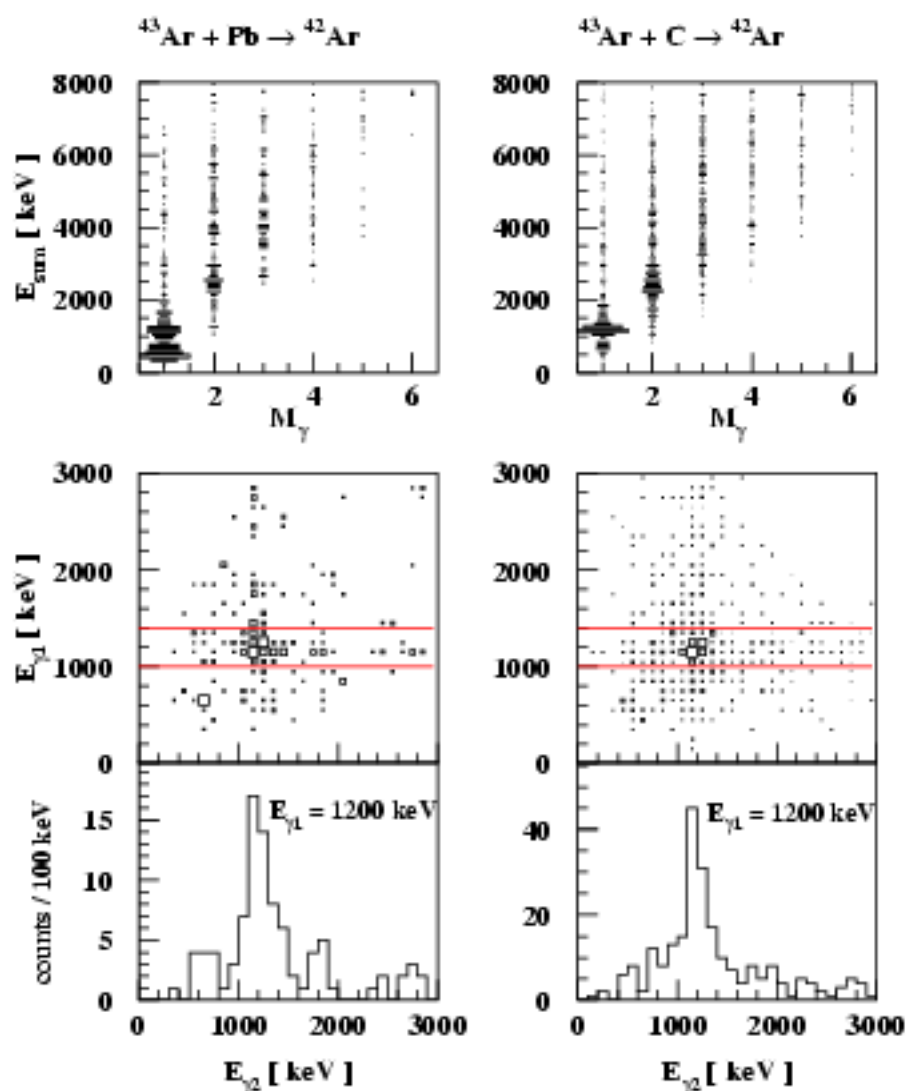


Figure 47: Gating on $A_2=42$, the peak around 1200 keV observed in both $^{43}\text{Ar} + \text{Pb} \rightarrow ^{42}\text{Ar}^* + 1n$ and $^{43}\text{Ar} + \text{Pb} \rightarrow ^{42}\text{Ar}^* + 1n$ reactions can be proven to be composed of two γ -lines from the γ -cascade $2^+(2487) \rightarrow 2^+(1208) \rightarrow 0^+(0)$ of ^{42}Ar . (top): The sum energy concentrates at 1200 keV with $M_\gamma=1$ and ~ 2400 keV with $M_\gamma=2$. (middle): The γ - γ -coincidence matrix peaks at $E_{\gamma 1}=E_{\gamma 2}=1200$ keV. (bottom): The projection on the $E_{\gamma 2}$ axis with a gate around $E_{\gamma 1}=1200$ keV shows a clean peak at $E_{\gamma 2}=1200$ keV.

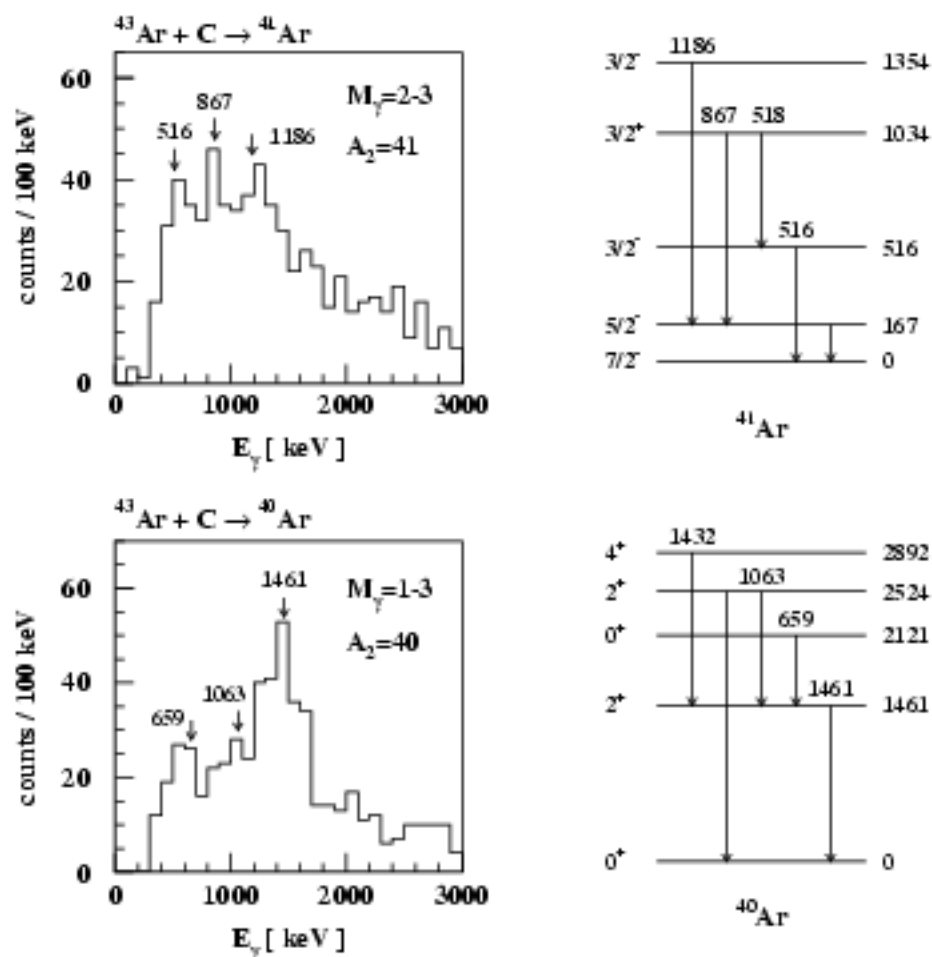


Figure 48: Gamma-spectra from two reaction channels obtained by gating on A_2 . top: From the $^{43}\text{Ar} + \text{C} \rightarrow ^{41}\text{Ar}$ reaction channel, with $M_\gamma=2-3$, three peaks show up (left), which are interpreted as γ -transitions from ^{41}Ar (right). bottom: From the $^{43}\text{Ar} + \text{C} \rightarrow ^{40}\text{Ar}$ reaction channel, gating on $M_\gamma=1-3$, three peaks related to transitions in ^{40}Ar can be seen.

from higher lying states of ^{40}Ar and ^{41}Ar show up clearly despite small statistics, thus demonstrate the sensitivity of this method.

5.3.3 ^{44}Ar with the Pb and C target

As displayed in fig. 49, by requiring $M_\gamma=1$ in the reaction of ^{44}Ar with the Pb target, a peak at $E_\gamma \approx 1144$ keV is obtained, which is suggested to originate from the first 2^+ state of ^{44}Ar observed recently [Sch96]. Originating from inelastic excitation, this peak can be improved by setting a proper cut on the scattering angle θ around $\theta_{max} = 21$ mrad (refer to chapter 4.2.3). No cut on A_2 is used in the spectra because of statistics. Therefore in the 1144 keV peak, there could be a small admixture of the 1200 keV line from γ -transitions in ^{42}Ar .

Gating on $A_2=44$, transitions of ^{44}Ar can be investigated via nuclear reactions $^{44}\text{Ar}+\text{C}\rightarrow^{44}\text{Ar}$ (fig. 50: left). Projecting the M_γ vs. E_γ spectrum (top) with $M_\gamma=1-3$, a peak shows up at ~ 1144 keV in the single γ spectrum (middle), representing the known 2^+ state of ^{44}Ar . In the same spectrum, we can also see a line at ~ 2000 keV. This is unlikely from the transition $4^+(3096)\rightarrow 2^+(1208)$ in ^{42}Ar although there could be a contamination of $A_2=42$ in the $A_2=44$ cut because (1) the energy is too high; (2) the E_{sum} vs. M_γ spectrum concentrating at $M_\gamma=1$, $E_{sum} \approx 1144$ and 2000 keV (bottom) is not consistent with the transition mentioned above which corresponds to $M_\gamma=1$, $E_{sum}=1208$ keV and $M_\gamma=2$, $E_{sum}=3096$ keV as shown in fig. 47(left). Therefore an unknown state at ~ 2000 keV which de-excites directly to the ground state is suggested to be added to the level scheme of ^{44}Ar .

The above suggestion is supported by the calculated level scheme of ^{44}Ar in the shell model framework [Ret97,Now98] (see fig. 51), in which the transition of $2_2^+(1899) \rightarrow 0^+(0)$ may corresponds to the γ -line at ~ 2000 keV observed in our measurement.

Requiring $A_2=42$ (fig. 50: right), projecting the M_γ vs. E_γ spectrum (top) with $M_\gamma=1-5$, we get a γ peak at 1200 keV (middle) and a sum energy spectrum concentrating at $M_\gamma=1$, $E_{sum}=1200$ and $M_\gamma=2$, $E_{sum} \approx 2400$ (bottom), showing again the γ -cascade $2^+(2487)\rightarrow 2^+(1208)\rightarrow 0^+(0)$ of ^{42}Ar as discussed in the former chapter.

Transitions from the excited states of ^{43}Ar (the first excited state of ^{43}Ar is 1740 keV [NNDC]) have not been clearly identified in the experiment. There might be two reasons: (1) ^{43}Ar is an odd-A nuclei with too many transition branches; (2) the cut on $A_2=43$ is not clean and there is admixture of $A_2=42$ and/or $A_2=44$.

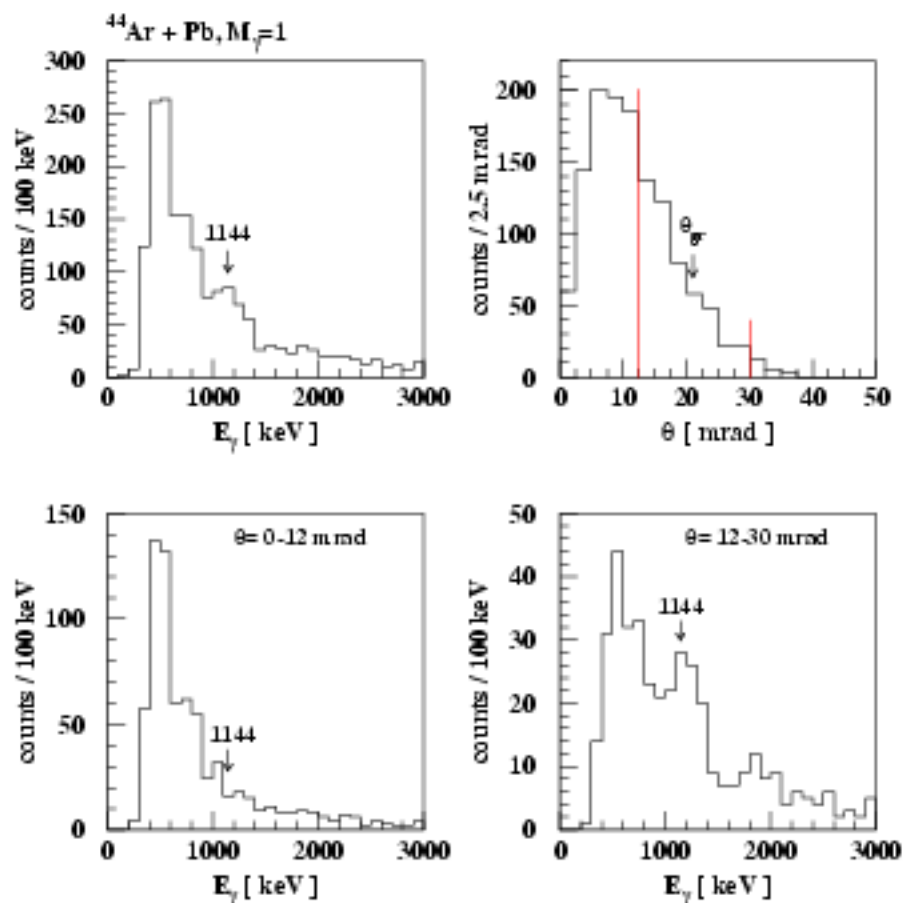


Figure 49: Requiring $M_\gamma=1$ in the reaction of ^{44}Ar with the Pb target, a peak related to the 2^+ (1144) state in ^{44}Ar is obtained (top-left). This peak can be improved by gating on proper scattering angles (top-right): with $\theta=0-12$ mrad only atomic background can be seen (bottom-left); with $\theta=12-30$ mrad a peak shows up clearly at ~ 1144 keV (bottom-right).

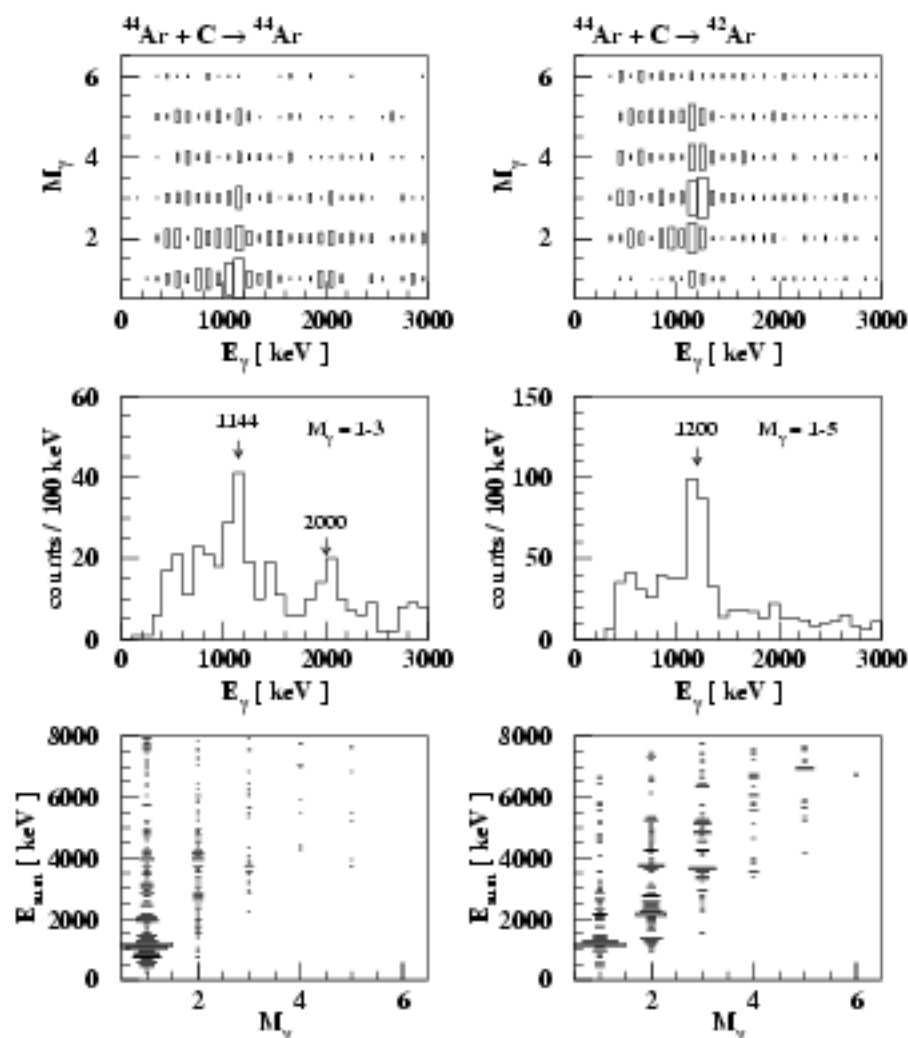


Figure 50: Spectra from the $^{44}\text{Ar} + \text{C} \rightarrow ^{44}\text{Ar}$ reaction channel indicate the transitions from the known $2^+(1144)$ state and an unknown state at ~ 2000 keV of ^{44}Ar (left). Spectra from the $^{44}\text{Ar} + \text{C} \rightarrow ^{42}\text{Ar}$ channel show the γ -cascade of ^{42}Ar as discussed in the former chapters (right). See text for details.

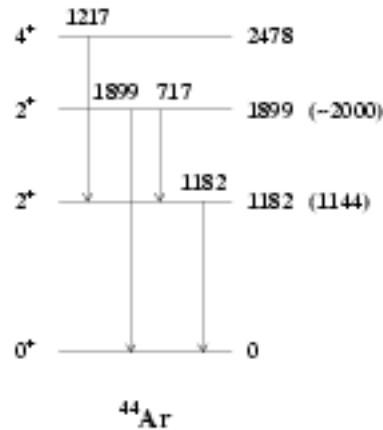


Figure 51: The calculated level scheme of ^{44}Ar in the shell model framework [Ret97,Now98]. The measured energies of states 2_1^+ [Sch96] and 2_2^+ are marked in brackets.

5.4 Experimental cross sections of γ -transitions and comparison with coupled-channels calculations

As examples, cross sections of the 1698 keV γ -line associated with the transition $5/2_1^+(1698) \rightarrow 1/2^+(0)$ in ^{27}Mg , and the 1473 keV γ -line corresponding to the transition $2^+(1473) \rightarrow 0^+(0)$ in ^{28}Mg , from inelastic excitation with both the Pb and C target, will be discussed.

5.4.1 Experimental cross sections

As discussed in chapter 4.3.6, in order to obtain the number of de-excitation photons to determine cross section experimentally, the detected γ -spectrum needs to be corrected by the CB efficiency. Fig. 52 shows four “corrected” spectra from four reactions $^{27}\text{Mg}+\text{Pb}$, $^{27}\text{Mg}+\text{C}$, $^{28}\text{Mg}+\text{Pb}$ and $^{28}\text{Mg}+\text{C}$ with conditions of (1) γ -multiplicity $M_\gamma=1$, (2) no signal from the neutron detector LAND (3) $Z_2 = Z_1$, (4) $A_2 = A_1$, and (5) no energy overflow in the CB (conditions 4 and 5 are only used with the C target). The efficiency for the Z_2 and A_2 determination does not affect cross sections because the number of projectiles N_{proj} is obtained with the same condition on Z_2 and A_2 .

Fitting these spectra to get the peak intensity N_{peak} , together with the number of projectiles N_{proj} (see table 9), the experimental cross section $\sigma_{i \rightarrow f}^{exp}$ for the decay from state $|i\rangle$ to $|f\rangle$,

can be derived by using formula (45) in chapter 4.4. The uncertainty of the cross sections is mainly due to the uncertainty of N_γ .

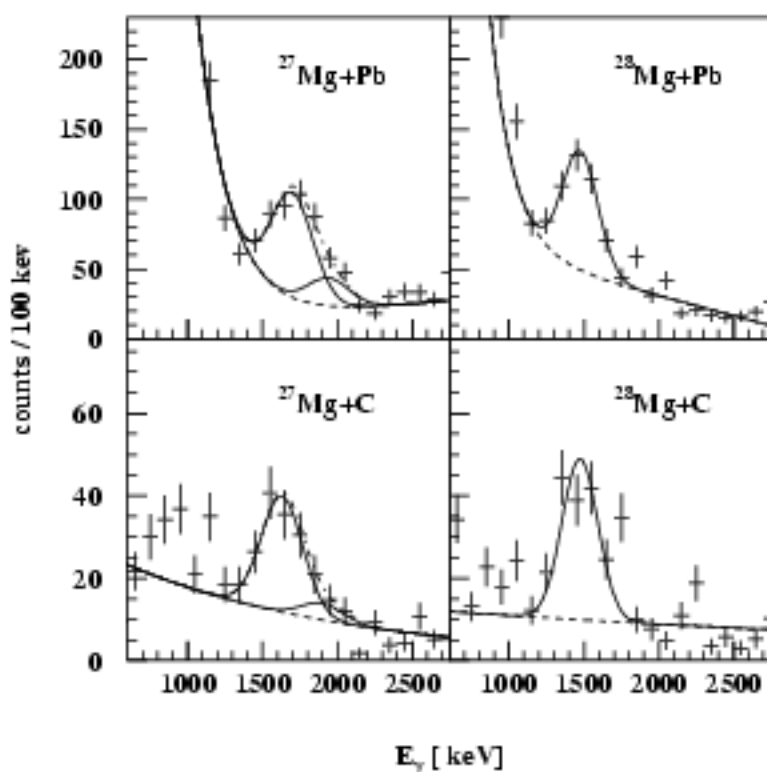


Figure 52: Gamma-spectra for four reactions, corrected with the CB efficiency. Peaks and backgrounds are fitted with solid and dashed lines. The γ -peak at $E_\gamma \approx 1700$ keV is fitted with two Gauss peaks because it is interpreted as a mixture of two transitions $5/2_2^+(1940), 5/2_1^+(1698) \rightarrow 1/2^+(0)$ in ^{27}Mg . The background of the top spectra is fitted with the sum of an exponential function and a first order polynomial while that of the bottom ones is fitted with an exponential function.

Table 9: The experimental cross section $\sigma_{i \rightarrow f}^{exp}$ for the decay from state $|i\rangle$ to $|f\rangle$ (energies in keV), derived from the peak intensity N_{peak} obtained from the four γ -spectra in fig. 52 and the number of projectiles N_{proj} .

reaction	transition	N_{peak}	N_{proj}	$\sigma_{i \rightarrow f}^{exp}$ (mb)
$^{27}\text{Mg}+\text{Pb}$	$5/2_1^+(1698) \rightarrow 1/2^+(0)$	$263 \pm 21\%$	2.22×10^6	43.3 ± 9.1
$^{27}\text{Mg}+\text{C}$	$5/2_1^+(1698) \rightarrow 1/2^+(0)$	$98 \pm 28\%$	0.67×10^6	5.4 ± 1.5
$^{28}\text{Mg}+\text{Pb}$	$2^+(1473) \rightarrow 0^+(0)$	$256 \pm 22\%$	1.82×10^6	51.5 ± 11.3
$^{28}\text{Mg}+\text{C}$	$2^+(1473) \rightarrow 0^+(0)$	$117 \pm 24\%$	0.54×10^6	8.1 ± 1.9

5.4.2 Cross sections from coupled-channels calculations

In the computer code CCNUC employing the coupled-channels method (see chapter 2.2), the first four states $1/2^+(0)$, $3/2^+(985)$, $5/2_1^+(1698)$ and $5/2_2^+(1940)$ of ^{27}Mg and the first four states $0^+(0)$, $2^+(1473)$, $0_2^+(3863)$ and $4^+(4020)$ of ^{28}Mg are included, respectively. See the known level schemes in fig. 53 for reference.

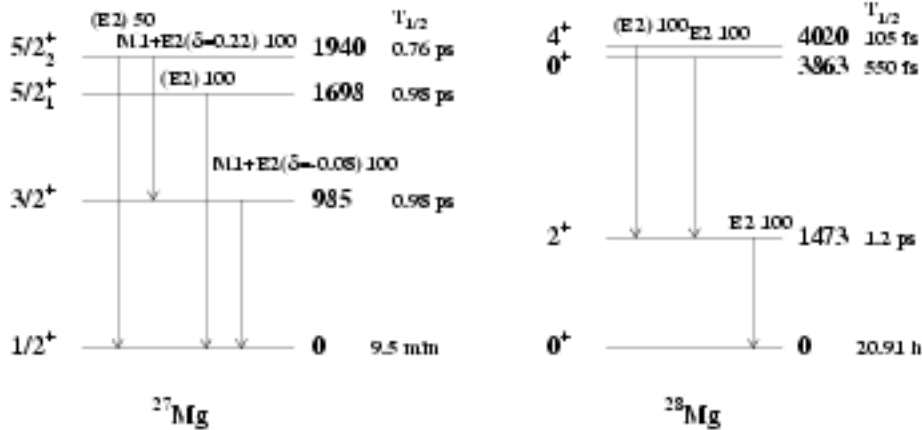


Figure 53: The known level scheme of ^{27}Mg and ^{28}Mg with energies in keV.

From the half lives $T_{1/2}$ of these states, the decay modes ($E\lambda$ or $M\lambda$), the branching ratios

and other quantities available in [NNDC], the reduced excitation probabilities $B(E\lambda) \uparrow$ and/or $B(M\lambda) \uparrow$ are calculated, which are the main part of the input for CCNUC. The output of CCNUC are cross sections σ_m^{cc} for excitation of each state $|m\rangle$ ($m=0,1,2,3$) mentioned above. The error of σ_m^{cc} originates mainly from the uncertainty of $T_{1/2}$.

In order to compare the experimental data with them, $\sigma_{i \rightarrow f}^{exp}$, the measured cross section for the decay from state $|i\rangle$ to $|f\rangle$, needs to be transformed to σ_m^{exp} . In ^{27}Mg , as the $5/2_1^+$ (1698) state decays only to the ground state $1/2^+$, $\sigma_{5/2_1^+} = \sigma_{5/2_1^+ \rightarrow 1/2^+}$ is obtained. In ^{28}Mg , the higher states 0_2^+ (3863) and 4^+ (4020) decay via 2^+ (1473), i.e. they feed to 2^+ (1473), however, because σ_{2^+} is at least two magnitudes larger than $\sigma_{0_2^+}$ and σ_{4^+} and $M_\gamma=1$ is required, we also have the simple relation of $\sigma_{2^+} = \sigma_{2^+ \leftarrow 0_2^+}$.

Table 10: Cross sections σ_m^{cc} and σ_m^{exp} for excitation of state $|m\rangle$ obtained by coupled-channels calculations using CCNUC and derived from experimental data.

reaction	state $ m\rangle$	σ_m^{cc} (mb)	σ_m^{exp} (mb)
$^{27}\text{Mg}+\text{Pb}$	$5/2_1^+$ (1698) of ^{27}Mg	25.0 ± 1.9	43.4 ± 9.1
$^{27}\text{Mg}+\text{C}$	$5/2_1^+$ (1698) of ^{27}Mg	3.5 ± 0.3	5.4 ± 1.5
$^{28}\text{Mg}+\text{Pb}$	2^+ (1473) of ^{28}Mg	67.7 ± 5.6	51.5 ± 11.3
$^{28}\text{Mg}+\text{C}$	2^+ (1473) of ^{28}Mg	13.3 ± 1.1	8.1 ± 1.9

Comparing experimental cross sections σ_m^{exp} with the coupled-channels calculations σ_m^{cc} in table 10 we see that for the odd nucleus ^{27}Mg experimental cross sections are roughly 50% larger than calculated ones while for the even-even nucleus ^{28}Mg the values for σ_m^{exp} are about consistent with σ_m^{cc} within the error. Whether the discrepancy in the odd case is due to the calculation or the matrix elements employed is not clear and should be clarified in a forthcoming investigation.

From table 10 we also see that the cross sections from the reactions with the Pb target are much bigger than with the C target. This is because the main contribution to the cross sections is Coulomb excitation which depends strongly on the charge numbers of colliding nuclei.

6 Summary and outlook

The aim of this work was to investigate the feasibility of a pioneering experimental method, namely in-beam γ -spectroscopy employing relativistic radioactive ion beams (RIB) for the study of the nuclear structure of the neutron-rich nuclei below ^{48}Ca with neutron number between the two magic numbers $N=20$ and $N=28$. Secondary reactions of the RIB with a Pb and a C target, e.g. Coulomb excitation, nuclear excitation and few nucleon removal reactions, were used to populate the excited states of the neutron-rich light nuclei.

A primary ^{50}Ti beam was produced by the synchrotron facility SIS at GSI, Darmstadt, with an energy of 330 AMeV and an intensity of 10^9 particles per spill (1 spill \approx 4 seconds). After fragmentation reactions with a 4 g/cm² ^9Be primary target, a variety of nuclei below ^{50}Ti were produced. From these fragments, about 50 nuclear species (in which more than 30 were β -unstable neutron-rich isotopes) with $Z = 4 - 20$, $A/Z \approx 2.1 - 2.5$ and energies ranging from 210 to 280 AMeV ($\beta \approx 0.58 \sim 0.64$) were selected simultaneously by the FRagment Separator FRS with $B\rho = 5.588$ Tm and $\Delta B\rho/B\rho \sim 0.5\%$. This secondary RIB which was transferred to the target area CAVE B had an intensity of around 10^4 particles per second for the full composition of nuclear species i.e. on the average about 200 particles per second for each nuclear species. In CAVE B, the mass number A_1 of each nuclear species in the RIB was identified by time of flight; A_2 after the secondary reactions was obtained by the ΔE - $B\rho$ -TOF method employing the dipole magnet ALADIN; the charge numbers Z_1 and Z_2 were determined by two ΔE counters.

Two experimental particularities are related to the high beam energy. An average Doppler broadening of $\sim 15\%$ is expected for in-beam γ -spectra detected by a common γ -detector with an opening angle of 18° ; the cross section of atomic background is at least three orders of magnitude larger than typical Coulomb excitation cross sections. The Darmstadt-Heidelberg Crystal Ball (CB) consisting of 162 individual NaI crystals with an intrinsic energy resolution of 8% is well suited for γ -spectroscopy employing relativistic RIBs; moreover, its 4π solid angle and large full energy efficiency $\varepsilon_{fe} \approx 70\%$ at 1.3 MeV compensate for the low beam intensity. To suppress atomic background, a 2 mm thick Pb tube was installed between CB and the secondary target which was placed at the center of the CB, and a threshold of ~ 500 keV was set to the CB trigger. In addition, the scattering angle θ was measured by three multiwire proportional chambers (MWPC) in order to suppress pure atomic background distributing at $\theta \approx 0^\circ$. Another goal to measure θ is to try to distinguish Coulomb and nuclear excitation which dominate at different impact parameter regions.

In order to measure the neutrons evaporated from giant resonances which is expected to be populated in relativistic Coulomb excitation, the neutron detector LAND was employed.

Z_1 and Z_2 were measured with a resolution of 0.5 mass units and an efficiency of nearly 100%, while A_1 was measured with a resolution 0.3~0.6 mass units (better for lighter isotopes) and an efficiency of 80%. The resolution of A_2 for heavy nuclei like Ar was 0.8 mass units with an efficiency of 30%; for light nuclei like Mg, A_2 could be derived by the standard mode with 0.8 mass units resolution and 55% efficiency and another mode with a better resolution of 0.6 mass units but only 10% efficiency.

The scattering angle θ was determined with an efficiency of 30%. With an intrinsic resolution of 5 mrad and the atomic angular straggling of 6 and 2 mrad for the Pb and C target, the combined resolution was not sufficient to distinguish Coulomb and nuclear excitation but helpful to suppress atomic background in the γ -spectra.

By setting cuts on Z_1 and A_1 , in-beam γ -spectroscopy of 30 ~ 40 nuclear species in the RIB could be performed. The weakest channels like ^{42}Ar where discrete γ -lines were identified had an intensity of only ~80 particles per second in the RIB. The incoming Mg- and Ar-isotopes representing light and heavy nuclei respectively, were discussed in detail as examples. $Z_2 = Z_1$ was required to limit the reactions to inelastic excitation and neutron removal reaction channels.

Requiring the γ -trigger, γ -multiplicity $M_\gamma=1$, and/or $A_2=A_1$, a γ -peak around 1473 MeV corresponding to the first excited state in ^{28}Mg was observed from the inelastic excitation of ^{28}Mg impinging on the Pb and C target. Similarly, another γ -peak around 1700 keV composed of two transitions of the low-lying states in ^{27}Mg was observed. Cross sections for these peaks were comparable with coupled-channels calculations where both the Coulomb and nuclear interactions are included. The cross sections from excitations with Pb were 5~10 times larger than with C where nuclear excitation is dominant. This shows that the major contribution to the inelastic excitation in Pb is Coulomb excitation.

As to nucleon removal reactions, from the $^{43}\text{Ar}+\text{Pb}\rightarrow^{42}\text{Ar}^*+1n$ and $^{43}\text{Ar}+\text{C}\rightarrow^{42}\text{Ar}^*+1n$ channels, a γ -peak around 1200 keV was observed with $M_\gamma=2-4$ (Pb) and $M_\gamma=1-4$ (C). By investigating the sum energy and γ - γ -coincidence matrix, this peak was confirmed to be associated with a γ -cascade in ^{42}Ar , demonstrating the high selectivity and sensitivity of the method. Moreover, from the two and three neutron removal reactions of ^{43}Ar with the C target, γ -peaks associated with higher-lying states of ^{41}Ar and ^{40}Ar were observed.

Cross sections of secondary fragmentation reactions of ^{28}Mg and ^{43}Ar with the C target were derived experimentally. They were comparable but not completely consistent with empirical calculations. The experimental data deduced from this experiment enable to modify the parametrization for a new systematics for masses of 20~45 and energies of 200~300 MeV.

The experiment can obviously be improved by replacing the three MWPCs by detectors with a higher efficiency and better resolution, e.g. silicon micro-strip detectors with a resolution of better than 1 mm. Only if a resolution of 1mm could be achieved, the resolution to determine A_2 would be as good as A_1 , and the intrinsic resolution of θ would reach 2 mrad. The final resolution of θ also depends on the thickness of target because of atomic straggling. Compromising between reaction yield and atomic straggling, an optimal target thickness might be around 0.5 g/cm² for Pb resulting in a θ resolution of 4 mrad.

The γ -energy resolution could be improved if some NaI crystals in the CB (e.g. at forward angle $\theta_\gamma < 30^\circ$) would be replaced by high resolution segmented Ge detectors. Calculations have shown that a resolution of 4% originating mainly from Doppler broadening could be achieved.

Since the last three years, the intensity of the primary beam from SIS has been increased by one to two orders of magnitude to around 10^{11} particles per spill. This high intensity offers the opportunity to study exotic nuclei far from β -stability.

Employing secondary RIB to study exotic nuclei near the neutron or proton drip-line is attracting more and more attention. The work at RIKEN [Mot95] and MSU [Sch96, Gla97, Ibb98] showed that, Coulomb excitation using intermediate-energy beams is a successful way to study the first excited state of exotic neutron-rich nuclei.

Our pilot experiment using 210~280 AMeV RIB – despite the low beam intensity and short beam time – demonstrates, on the other hand, that in-beam γ -spectroscopy with RIB at relativistic energies is feasible too and can be further improved. With heavy targets like Pb, single step inelastic excitation originating mainly from Coulomb interaction takes place so that first excited state can be investigated and B(E2) values can be extracted; with light targets like C, moreover, secondary nuclear reactions are strong and excited states with higher energy and/or spin can be populated thus offering richer spectroscopic information in this region.

A The two methods to produce radioactive ion beams (RIB)

The two methods to produce radioactive ion beams discussed in chapter 1 are compared in the following table.

Table 11: The comparison between the ISOL technique and projectile fragmentation

	ISOL	projectile fragmentation
primary beam	high intensity light particle like proton	low intensity heavy ion
production target	1-300 g/cm ² , complicated target+catcher+ion source	a few 100 mg/cm ² to few g/cm ² relatively simple
reaction	target fragmentation	projectile fragmentation
separation	slow, diffusion time: ms - s, sometimes even minutes	fast, flight time: ns - μ s
RIBs		
energy	low, need post-acceleration	high, sometimes need to be slowed down
intensity	high, 10 ⁶ -10 ¹² pps	low, < 1% of the primary beam
emittance	good	poor
purity	isobar contamination	good
charge state	low charge state with broad distribution	high charge state with sharp distribution, fully stripped for light elements
element limit	short-lived isotopes from refractory elements are suppressed	no chemical selectivity

B Estimate of $\Delta(B\rho)/(B\rho)_0$ resolution

The calculations of X_t , α_1 , X_4 and α_2 , which are used to calculate $\Delta(B\rho)/(B\rho)_0$ in chapter 4.1.2, as well as the estimate of their resolutions, are as follows:

$$\begin{aligned} X_t &= \frac{1250X_2 - 143X_1}{1107}, & \delta X_t &= \sqrt{\left(\frac{1250}{1107}\delta X_2\right)^2 + \left(\frac{143}{1107}\delta X_1\right)^2} = 0.17; \\ \alpha_1 &= \tan^{-1}\left(\frac{X_3 - X_t}{132}\right), & \delta\alpha_1 &= \frac{\sqrt{\delta X_3^2 + \delta X_t^2}}{132} = 2.6 \times 10^{-3}; \\ X_4 &= G1X + 31, & \delta X_4 &= \delta G1X = 0.10; \\ \alpha_2 &= \tan^{-1}\left(\frac{G2X - G1X}{206}\right) + 84 \times 10^{-3}, & \delta\alpha_2 &= \frac{\sqrt{\delta G2X^2 + \delta G1X^2}}{206} = 0.69 \times 10^{-3}. \end{aligned}$$

Here the resolutions of ZST01, ZST02 and ZST03 are: $\delta X_1 = \delta X_2 = 0.15$ cm and $\delta X_3 = 0.30$ cm; while those of GFI01 and GFI02 are: $\delta G1X = \delta G2X = 0.10$ cm.

The parameters in formula (39) determined by the ALADIN geometry [Cub96] are:

$$\begin{aligned} a_1 &= 1.000077, \\ b_1 &= 724.9481, \\ c_1 &= -103.9487, \\ a_2 &= 1.8718451E-07, \\ b_2 &= 1.000059, \\ c_2 &= -0.2526325. \end{aligned}$$

If $\Delta(B\rho)/(B\rho)_0$ is calculated from formula (40), it has a resolution of:

$$\begin{aligned} \delta\left(\frac{\Delta(B\rho)}{(B\rho)_0}\right) &= \delta\left\{\frac{1}{c_2}\left[-a_2X_t - \frac{b_2}{132}(X_3 - X_t) + \alpha_2\right]\right\} \\ &= \frac{1}{|c_2|} \sqrt{\left[\left(\frac{b_2}{132} - a_2\right)\delta X_t\right]^2 + \left(\frac{b_2}{132}\delta X_3\right)^2 + \delta\alpha_2^2} = 1.07\%. \end{aligned}$$

If $\Delta(B\rho)/(B\rho)_0$ is calculated from formula (41), the resolution is estimated as:

$$\begin{aligned} a_3 &= b_2c_1 - b_1c_2 = 79.1906, \\ b_3 &= b_2a_1 - b_1a_2 = 1.00000, \\ \delta\left(\frac{\Delta(B\rho)}{(B\rho)_0}\right) &= \delta\left\{\frac{1}{a_3}\left[-b_3X_t + b_2G1X - b_1\left(\frac{G2X}{206} - \frac{G1X}{206}\right)\right]\right\} \\ &= \frac{1}{|a_3|} \sqrt{(b_3\delta X_t)^2 + \left[\left(\frac{b_1}{206} + b_2\right)\delta G1X\right]^2 + \left(\frac{b_1}{206}G2X\right)^2} = 0.72\%. \end{aligned}$$

C Scattering angle determination and resolution

The calculations of θ_X^{in} , θ_Y^{in} , θ_X^{out} , θ_Y^{out} and their resolutions, which are used to determine scattering angle θ and its resolution in chapter 4.2.1, will be discussed in details.

From ZST01 and ZST02 with resolution of $\delta X_1 = \delta Y_1 = \delta X_2 = \delta Y_2 = 0.15$ cm, the incoming angle and the position at the target were determined:

$$\begin{aligned}\theta_X^{in} &= \tan^{-1}\left(\frac{X_2 - X_1}{1107}\right), & \theta_Y^{in} &= \tan^{-1}\left(\frac{Y_2 - Y_1}{1107}\right); \\ X_t &= \frac{1250X_2 - 143X_1}{1107}, & Y_t &= \frac{1250Y_2 - 143Y_1}{1107};\end{aligned}$$

with a resolution of

$$\begin{aligned}\delta\theta_X^{in} &= \delta\theta_Y^{in} = \frac{\sqrt{\delta X_2^2 + \delta X_1^2}}{1107} = 0.19 \times 10^{-3}; \\ \delta X_t &= \delta Y_t = \sqrt{\left(\frac{1250}{1107}\delta X_2\right)^2 + \left(\frac{143}{1107}\delta X_1\right)^2} = 0.17.\end{aligned}$$

If (X_3, Y_3) from ZST03 with a resolution of 0.3 cm was available, the outgoing angle were obtained as:

$$\theta_X^{out} = \tan^{-1}\left(\frac{X_3 - X_t}{132}\right), \quad \theta_Y^{out} = \tan^{-1}\left(\frac{Y_3 - Y_t}{132}\right),$$

with a resolution of

$$\delta\theta_X^{out} = \delta\theta_Y^{out} = \frac{\sqrt{\delta X_3^2 + \delta X_t^2}}{132} = 2.6 \times 10^{-3}.$$

If (X_3, Y_3) was not there, Y_{TOF} from the TOF-wall with a resolution of 2 ~ 3 cm was used to get θ_Y^{out} :

$$\theta_Y^{out} = \tan^{-1}\left(\frac{Y_{TOF} - Y_t}{1295}\right), \quad \delta\theta_Y^{out} = \frac{\sqrt{\delta Y_{TOF}^2 + \delta Y_t^2}}{1295} = 2.3 \times 10^{-3};$$

as for θ_X^{out} , which is actually α_1 in chapter 4.1.2, could be derived from GFI01 and GFI02 with the relation in formula (39):

$$\begin{aligned}\theta_X^{out} &= \frac{1}{a_3}(-c_3X_t - c_2X_4 + c_1\alpha_2), \\ a_3 &= b_2c_1 - b_1c_2 = 79.1906, \\ c_3 &= a_2c_1 - a_1c_2 = 0.25263,\end{aligned}$$

with a resolution of

$$\delta\theta_X^{out} = \frac{1}{|a_3|} \sqrt{(c_3\delta X_t)^2 + \left[\left(\frac{c_1}{206} + c_2\right)\delta G1X\right]^2 + \left(\frac{c_1}{206}\delta G2X\right)^2} = 1.3 \times 10^{-3}.$$

D Properties of electromagnetic transitions

A nuclear state $|i\rangle$ decays to a lower excited state $|f\rangle$ by emitting a photon (γ -ray) with energy

$$E_\gamma = h\omega = E_i - E_f \quad (MeV), \quad (52)$$

and wavelength

$$\lambda = \frac{hc}{E_\gamma} = \frac{197.3}{E_\gamma} \quad (fm). \quad (53)$$

The angular momentum of the photon, λ , is called the multipolarity of radiation. For a given λ , there are two kinds of radiation, namely

$$\begin{aligned} \text{Electric } 2^\lambda - \text{pole } (E\lambda) \text{ radiation: } \pi_i \pi_f &= (-)^\lambda, \\ \text{Magnetic } 2^\lambda - \text{pole } (M\lambda) \text{ radiation: } \pi_i \pi_f &= (-)^{\lambda+1}. \end{aligned} \quad (54)$$

The transition probability for γ -ray emission of multipolarity λ is

$$P(\lambda, I_i \rightarrow I_f) = \frac{8\pi(\lambda+1)}{\lambda[(2\lambda+1)!!]^2} \frac{1}{h} \left(\frac{E_\gamma}{197.3}\right)^{2\lambda+1} B(\lambda, I_i \rightarrow I_f), \quad (55)$$

with the reduced transition probability

$$B(\lambda, I_i \rightarrow I_f) = \frac{1}{2I_i+1} |\langle f|M(\lambda)|i\rangle|^2, \quad (56)$$

where $\langle f|M(\lambda)|i\rangle$ is the transition matrix element (or transition amplitude).

With $B(E\lambda)$ in units of $e^2 fm^{2\lambda}$ and $B(M\lambda)$ in units of $\mu_N^2 fm^{2\lambda-2}$, the relations between $P(\lambda)$ and $B(\lambda)$ are

$$\begin{aligned} P(E\lambda, I_i \rightarrow I_f) &= 5.499 \times 10^{22} \frac{(\lambda+1)}{\lambda[(2\lambda+1)!!]^2} \left(\frac{E_\gamma}{197.3}\right)^{2\lambda+1} B(E\lambda, I_i \rightarrow I_f) \quad (s^{-1}), \\ P(M\lambda, I_i \rightarrow I_f) &= 6.071 \times 10^{20} \frac{(\lambda+1)}{\lambda[(2\lambda+1)!!]^2} \left(\frac{E_\gamma}{197.3}\right)^{2\lambda+1} B(M\lambda, I_i \rightarrow I_f) \quad (s^{-1}). \end{aligned} \quad (57)$$

For the transitions with $\lambda=1$ to 4, there are the following relations [Mor 76]

$$\begin{aligned} P(E1) &= 1.59 \times 10^{15} E_\gamma^3 B(E1), \\ P(E2) &= 1.22 \times 10^9 E_\gamma^5 B(E2), \\ P(E3) &= 5.67 \times 10^2 E_\gamma^7 B(E3), \\ P(E4) &= 1.69 \times 10^{-4} E_\gamma^9 B(E4), \end{aligned}$$

$$\begin{aligned}
P(M1) &= 1.76 \times 10^{13} E_\gamma^3 B(M1) , \\
P(M2) &= 1.35 \times 10^7 E_\gamma^5 B(M2) , \\
P(M3) &= 6.28 \times 10^0 E_\gamma^7 B(M3) , \\
P(M4) &= 1.87 \times 10^{-6} E_\gamma^9 B(M4) .
\end{aligned} \tag{58}$$

With the single-particle aspect, namely the assumption that radiation originates from excitation of only one nucleon, a rough estimate of $B(\lambda)$, known as the Weisskopf estimate, can be derived [Mor76]:

$$\begin{aligned}
B^w(E\lambda) &= \frac{1}{4\pi} \left(\frac{3}{\lambda+3}\right)^2 e^2 R_0^{2\lambda} = \frac{1}{4\pi} \left(\frac{3}{\lambda+3}\right)^2 (1.2A^{1/3})^{2\lambda} \quad (e^2 fm^{2\lambda}) , \\
B^w(M\lambda) &= \frac{10}{\pi} \left(\frac{3}{\lambda+3}\right)^2 \mu_N^2 R_0^{2\lambda-2} = \frac{10}{\pi} \left(\frac{3}{\lambda+3}\right)^2 (1.2A^{1/3})^{2\lambda-2} \quad (\mu_N^2 fm^{2\lambda-2}) .
\end{aligned} \tag{59}$$

For E2 and M1 transitions the Weisskopf estimate are

$$\begin{aligned}
B^w(E2) &= \frac{1}{4\pi} \left(\frac{3}{5}\right)^2 (1.2A^{1/3})^4 = 5.94 \times 10^{-2} A^{4/3} \quad (e^2 fm^4) , \\
B^w(M1) &= \frac{10}{\pi} \left(\frac{3}{4}\right)^2 (1.2A^{1/3})^0 = 1.79 \quad (\mu_N^2 fm^0) .
\end{aligned} \tag{60}$$

References

- [Ajz87] F. Ajzenberg-Selove, Nucl. Phys. A 475 (1987) 1.
- [Ajz91] F. Ajzenberg-Selove, Nucl. Phys. A 523 (1991) 1.
- [ALA88] ALADIN Collaboration, GSI Annual Report 1988, p. 292.
- [Ald75] K. Adler, A. Winther, Electromagnetic Excitation, Theory of Coulomb Excitation with Heavy Ions (North-Holland, Amsterdam, 1975).
- [Anh84] R. Anholt, S. A. Andriamonje, E. Morenzoni, Ch. Stoller, J. D. Molitoris, W. E. Meyerhof, H. Bowman, J. -S. Xu, Z. -Z. Xu, J. O. Rasmussen and D. H. H. Hoffmann, Phys. Rev. Lett. 53 (1984) 234.
- [Anh86] R. Anholt, Ch. Stoller, J. D. Molitoris, D. W. Spooner, E. Morenzoni, S. A. Andriamonje, W. E. Meyerhof, H. Bowman, J. -S. Xu, Z. -Z. Xu, J. O. Rasmussen and D. H. H. Hoffmann, Phys. Rev. A 33 (1986) 2270.
- [Aud95] G. Audi and A. H. Wapstra, Nucl. Phys. A 595 (1995) 409.
- [Bau91] G. Bauer, Nucl. Phys. A 531 (1991) 685.
- [Ben89] C. J. Benesh, B. C. Cook and J. P. Vary, Phys. Rev. C 40 (1989) 1198.
- [Ber96] C. A. Bertulani, L. F. Canto, M. S. Hussein and A. F. R. de Toledo Piza, Phys. Rev. C 53 (1996) 334.
- [Bin87] W. R. Binns, T. L. Garrard, M. H. Israel, M. P. Kertzmann, J. Klarmann, E. C. Stone and C. J. Waddington, Phys. Rev. C 36 (1987) 1870.
- [Bla89] Th. Blaich, R. Freifelder, N. Herrmann, J. K. Keller, P. Koczon, M. Krämer, Y. Leifels, V. Lindenstruth, W. F. J. Müller, R. Schmidt and K. Teh, GSI Annual Report 1989, p. 311.
- [Boe86] F. W. N. de Boer, H. J. Wollersheim, H. Emling, E. Grein, E. Grosse, W. Spreng, G. Eckert, Th. W. Elze, K. Stelzer and Ch. Lauterbach, Z. Phys. A 325 (1986) 457.
- [Boh53] A. Bohr, B. R. Mottelson, Mat. Fys. Medd. Dan. Vid. Selsk., Vol. 27, No. 16 (1953).
- [Bor95] K. Boretzky, Ph.D. thesis, University of Frankfurt, 1995.
- [Bro87] I. N. Bronstein and K. A. Semendjajew, Taschenbuch der Mathematik (Verlag Harri Deutsch, Thun und Frankfurt/Main, 1987).
- [Cer93] CERN Program Library entry Q121, PAW-Physics Analysis Workstation, CERN, Geneva, Switzerland, 1993.

- [Cer94] CERN Program Library entry W5013, GEANT-Detector Description and Simulation Tool, CERN, Geneva, Switzerland, 1994.
- [Cer95] CERN Program Library entry Y250, HBOOK-Statistic Analysis and Histogramming, CERN, Geneva, Switzerland, 1995.
- [Cli86] D. Cline, *Ann. Rev. Nucl. Part. Sci.* **36** (1986) 683.
- [Cub96] J. Cub, private communication.
- [Cub97] J. Cub, J. Holeczek, S. Wan et al., *Acta Physicz Polonica B* **28** (1997) 367.
- [Cub98] J. Cub, G. Stengel, A. Grünschloß, K. Boretzky, T. Aumann, W. Dostal, B. Eberlein, Th.W. Elze, H. Emling, G. Ickert, J. Holeczek, R. Holzmann, J.V. Kratz, R. Kulesa, Y. Leifels, H. Simon, K. Stelzer, J. Stroth, A. Surowiec, and E. Wajda, *Nucl. Instr. and Meth. A* **402** (1998) 67.
- [Cum90] J. R. Cummings, W. R. Binns, T. L. Garrard, M. H. Israel, J. Klarmann, E. C. Stone and C. J. Waddington, *Phys. Rev. C* **42** (1990) 2508.
- [Dét79] C. Détraz, D. Guillemaud, G. Huber, R. Klapisch, M. Langevin, F. Naulin, C. Thibault, L. C. Carraz and F. Touchard, *Phys. Rev. C* **19** (1979) 164.
- [Eis76] J. M. Eisenberg and W. Greiner, *Excitation Mechanisms of the Nucleus* (North-Holland, Amsterdam, 1976).
- [End90] P. M. Endt, *Nucl. Phys. A* **521** (1990) 1; *A* **529** (1991) 763 (errata I); *A* **564** (1993) 609 (errata II).
- [Fau96] M. Fauerbach, D. J. Morrissey, W. Benenson, B. A. Brown, M. Hellström, J. H. Kelly, R. A. Kryger, R. Pfaff, C. F. Powell and B. M. Sherrill, *Phys. Rev. C* **53** (1996) 647.
- [Fuk92] N. Fukunishi, T. Otsuka and T. Sebe, *Phys. Lett. B* **296** (1992) 279.
- [Gla97] T. Glasmacher, B. A. Brown, M. J. Chromik, P. D. Cottle, M. Fauerbach, R. W. Ibbotson, K. W. Kemper, D. J. Morrissey, H. Scheit, D. W. Skenicka and M. Steiner, *Phys. Lett. B* **395** (1997) 163.
- [Gui84] D. Guillemaud, C. Détraz, M. Langevin, F. Naulin, M. de Saint-Simon, C. Thibault, F. Touchard and M. Epherre, *Nucl. Phys. A* **426** (1984) 37.
- [Gui89] D. Guillemaud-Mueller, Yu. E. Penionzhkevich, R. Anne, A. G. Artukh, D. Bazin, V. Borrel, C. Détraz, D. Guerreau, B. A. Gvozdev, J. C. Jacmart, D. X. Jiang, A. M. Kalinin, V. V. Kamanin, V. B. Kutner, M. Lewitowicz, S. M. Lukyanov, A. C. Mueller, N. Hoai Chau, F. Pougheon, A. Richard, M. G. Saint-Laurent and W. G. Schmidt-Ott, *Z. Phys. A* **332** (1989) 189.

- [Hol92] R. Holzmann, K. Grimm, R. Kulesa, E. Wajda, H. Xie, M. Zinser and the LAND Collaboration, GSI Annual Report 1992, p.48.
- [Hol96] J. Holeczek, private communication.
- [Hol97] R. Holzmann, private communication.
- [Hub78] G. Huber, F. Touchard, S. Büttenbach, C. Thibault, R. Klapisch, H. T. Duong, S. Liberman, J. Pinard, J. L. Vialle, P. Juncar and P. Jacquinet, Phys. Rev. C 18 (1978) 2342.
- [Ibb98] R. W. Ibbotson, T. Glasmacher, B. A. Brown, L. Chen, M. J. Chromik, P. D. Cottle, M. Fauerbach, K. W. Kemper, D. J. Morrissey, H. Scheit and M. Thoenessen, Phys. Rev. Lett. 80 (1998) 2081.
- [Jac75] J. D. Jackson, Classical Electrodynamics (Wiley & sons, New York, 1975).
- [Kas94] M. Kaspar, Diplom thesis, University of Frankfurt, 1994.
- [LAN92] LAND Collaboration, Th. Blaich, Th. W. Elze, H. Emling, H. Freiesleben, K. Grimm, W. Henning, R. Holzmann, G. Ickert, J. K. Keller, H. Klingler, W. Kneissl, R. König, R. Kulesa, J. V. Kratz, D. Lambrecht, J. S. Lange, Y. Leifels, E. Lubkiewicz, M. Proft, W. Prokopowicz, C. Schütter, R. Schmidt, H. Spies, K. Stelzer, J. Stroth, W. Walus, E. Wajda, H. J. Wollersheim, M. Zinser and E. Zude, Nucl. Instr. and Meth. A 314 (1992) 136.
- [Lei93] Y. Leifels, Ph.D. thesis, University of Bochum, 1993.
- [Leo94] W. R. Leo, Techniques for Nuclear and Particle Physics Experiments (Springer-Verlag, Berlin and Heidelberg, 1994).
- [Liv69] J. J. Livingood, The Optics of Dipole Magnets (Academic Press, New York and London, 1969).
- [Met86] V. Metag, D. Habs and D. Schwalm, Comments on Nucl. Part. Phys. 16 (1986) 213.
- [Mor76] H. Morinaga and T. Yamazaki, In-Beam Gamma-Ray Spectroscopy (North-Holland, Amsterdam, 1976).
- [Mor89] D. J. Morrissey, Phys. Rev. C 39 (1989) 460.
- [Mot95] T. Motobayashi, Y. Ikeda, Y. Ando, K. Ieki, M. Inoue, N. Iwasa, T. Kikuchi, M. Kurokawa, S. Moriya, S. Ogawa, H. Murakami, S. Shimoura, Y. Yanagisawa, T. Nakamura, Y. Watanabe, M. Ishihara, T. Teranishi, H. Okuno and R. F. Casten, Phys. Lett. B 346 (1995) 9.

- [Nil95] B. S. Nilsen, C. J. Waddington, J. R. Cummings, T. L. Garrard and J. Klarmann, *Phys. Rev. C* 52 (1995) 3277.
- [NNDC] Nuclear Data Sheets, Edited by National Nuclear Data Center, Brookhaven National Laboratory, program ENSDAT.
- [Now98] F. Nowacki, private communication
- [Pel82] D. Pelte and D. Schwalm, *In-beam Gamma-ray Spectroscopy with Heavy Ions* (North-Holland, Amsterdam, 1982).
- [Pov94] A. Poves and J. Retamosa, *Nucl. Phys. A* 571 (1994) 221.
- [Ram88] S. Raman, C. W. Nestor and K. H. Bhatt, *Phys. Rev. C* 37 (1988) 805.
- [Ram91] S. Raman, C. W. Nestor, S. Kahane and K. H. Bhatt, *Phys. Rev. C* 43 (1991) 556.
- [Rav91] H. L. Ravn, Paper Presented at Second International Conference on Radioactive Nuclear Beams, Louvain-la-Neuve, 1991, Section 2, p. 85.
- [Ret97] J. Retamosa, E. Caurier, F. Nowacki and A. Poves, *Phys. Rev. C* 55 (1997) 1266.
- [Sak96] H. Sakurai, N. Aoi, A. Goto, M. Hirai, N. Inabe, M. Ishihara, H. Kobinata, T. Kubo, H. Kumagai, T. Nakagawa, T. Nakamura, M. Notani, Y. Watanabe, Y. Watanabe and A. Yoshida, *Phys. Rev. C* 54 (1996) R2802.
- [Sat87] Satchler, *Nucl. Phys. A* 472 (1987) 215.
- [Sch91] T. Schwab, Ph.D. thesis, University of Gießen, 1991.
- [Sch94] D. Schwalm, Coulomb Excitation at "Safe" and "Unsafe" Energies, MPIH-V 15-1994.
- [Sch96] H. Scheit, T. Glasmacher, B. A. Brown, J. A. Brown, P. D. Cottle, P. G. Hansen, R. Harkewicz, M. Hellström, R. W. Ibbotson, J. K. Jewell, K. W. Kemper, D. J. Morrissey, M. Steiner, P. Thirolf and M. Thoenessen, *Phys. Rev. Lett.* 77 (1996) 3967.
- [She91] B. M. Sherrill, Paper Presented at Second International Conference on Radioactive Nuclear Beams, Louvain-la-Neuve, 1991, Section 1, p. 3.
- [Sor95] O. Sorlin, D. Guillemaud-Mueller, R. Anne, L. Axelsson, D. Bazin, W. Böhmer, V. Borrel, Y. Jading, H. Keller, K.-L. Kratz, M. Lewitowicz, S. M. Lukyanov, T. Mehren, A. C. Mueller, Yu. E. Penionzhkevich, F. Pougheon, M. G. Saint-Laurent, V. S. Salamatina, S. Shoedder and A. Wöhr, *Nucl. Phys. A* 583 (1995) 763.

- [Spi79] E. Spindler, H. D. Betz and F. Bell, *Phys. Rev. Lett.* **42** (1979) 832.
- [Ste91] H. Stelzer, *Nucl. Instr. and Meth. A* **310** (1991) 103.
- [Ste96] G. Stengel, Diplom thesis, University of Frankfurt, 1996.
- [Süm90] K. Sümmerer, W. Brüche, D. J. Morrissey, M. Schädel, B. Szweryn, Yang Weifan, *Phys. Rev. C* **42** (1990) 2546.
- [Til93] D. R. Tilley, H. R. Weller and C. M. Cheves, *Nucl. Phys. A* **564** (1993) 1.
- [Til95] D. R. Tilley, H. R. Weller, C. M. Cheves, R. M. Chasteler, *Nucl. Phys. A* **595** (1995) 1.
- [Wan97] S. Wan, P. Reiter, J. Cub, H. Emling, J. Gerl, R. Schubert and D. Schwalm for the CB-LAND-FRS collaboration, *Z. Phys. A* **358** (1997) 213.
- [Web90] W. R. Webber, J. C. Kish, D. A. Schrier, *Phys. Rev. C* **41** (1990) 533.
- [Wer94] T. R. Werner, J. A. Sheikh, W. Nazarewicz, M. R. Strayer, A. S. Umar and M. Misu, *Phys. Lett. B* **333** (1994) 303.
- [Wil80A] B. H. Wildentahal and W. Chung, *Phys. Rev. C* **22** (1980) 2260.
- [Wil80B] W. W. Wilcke et al., *At. Data Nucl. Data Tables* **25** (1980) 389.
- [Wil83] B. H. Wildentahal, M. S. Curtin and B. A. Brown, *Phys. Rev. C* **28** (1983) 1343.
- [Win79] A. Winther and K. Adler, *Nucl. Phys. A* **319** (1979) 518.
- [Wol93] H. J. Wollersheim, GSI Report, GSI-93-22. ISSN 0171-4546 (1993).

Acknowledgement

First of all I want to thank all the CB-LAND-FRS collaborators who participated in the experiment.

My special gratitude is to Prof. Dr. Dirk Schwalm, Dr. Jürgen Gerl, Dr. Peter Reiter and Dr. Jürgen Cub who have been strongly involved in this project and have helped me a lot in analyzing and interpreting the data.

I am indebted to Dr. Hans Emling for introducing the computer code CCNUC and explaining the related theory; to Dr. Hans-Jürgen Wollersheim for the discussions about angular distributions of γ -rays in the rest and lab systems; to Dr. Klaus Sümmerer for explaining the methods to produce RIBs; to Dr. Romain Holzmann for explaining the atomic processes; to Dr. Hubert Grawe and Dr. F. Nowacki for the newly calculated levels of ^{44}Ar and discussions about nuclear structure models; to Mr. Jacek Holeczek for analyzing data of the particle detectors; to Dipl. Phys. Alexander Grünschloß for drawing the picture of the set-up in CAVE B and to Dr. Konstanze Boretzky for the picture of LAND and "schwätzen" about babys before my son was born.

The joy to share an office with Dipl. Phys. Matthias Kaspar and Dipl. Phys. Ingo Peter as well as their help are unforgettable. It was a great pleasure to work with Dr. Jürgen Gerl, Dr. Tom Happ, Mr. Armin Kleinböhl, Dipl. Ing. Ivan Kozhoukharov, Dr. Thorsten Kröll, Miss Pascale Mayet, Dr. Maurycy Rejmund, Dipl. Ing. Henning Schaffner, Dr. Christian Schlegel, Dr. Rüdiger Schubart, Dr. Ralf Schubert, Dipl. Phys. Stefan Schremmer, Dipl. Phys. Gerhard Stengel, Dr. Kai Vetter, Dipl. Phys. Boris Wagner and Dr. Hans-Jürgen Wollersheim.

Thanks are also due to the GSI staff especially Mrs. Aloisia Busch and Mrs. Silvia Engel for the help with daily problems.

This work would not have been possible to be completed without Mrs. Ria Frey who takes care of my baby like her own child. I am also very thankful to my friend Ms. Jinghong LIU for her warm-hearted help everywhere outside of physics.

Finally, I would like to thank my husband Weiguang YAO for his hundreds of letters and thousands of e-mails, either from Beijing or from London (Ontario) during my stay in Darmstadt.

CV

Name: WAN
First name: Shuying
Nationality: Chinese
Date of birth: October 3rd, 1968
Place of birth: Sichuan, P. R. China
Marital status: Married, one child
Scientific field: Nuclear Physics

1975-1980 primary school, Sichuan, China
1980-1986 secondary school, Sichuan, China
1986-1990 undergraduate study at Peking University, Beijing, China
1990 Bachelor's degree of science
1990-1993 graduate study at China Institute of Atomic Energy,
Beijing, China, degree thesis: The Negative Parity States
in the Actinide Region
1993 Master's degree of science
1993-1994 research assistant in the department of physics at
China Institute of Atomic Energy, Beijing, China
1994-1998 research assistant in the department of nuclear physics II
at GSI and Ph. D. student at Heidelberg University, Germany.